UNIVERSITÀ
DI PAVIA

UNIVERSITÀ DEGLI STUDI DI PAVIA

UNIVERSITÁ DELLA SVIZZERA ITALIANA

JOINT PhD PROGRAM IN COMPUTATIONAL MATHEMATICS AND DECISION SCIENCES XXXV CYCLE

An electro-fluid-structure model for cardiac numerical simulations based on an embedded strategy

Advisor:
Prof. Rolf KRAUSE

PhD dissertation of:
Silvia CALIGARI
matr. 479177

Academic year 2021-2022

I certify that except where due acknowledgement has been given, the work presented in this thesis is that of the author alone; the work has not been submitted previously, in whole or in part, to qualify for any other academic award; and the content of the thesis is the result of work which has been carried out since the official commencement date of the approved research program.

Silvia Caligari
Pavia, 25th October 2023

To my family

Abstract

In this Thesis, we propose a loosely coupled model for numerical cardiac simulations representing the main physical processes involved in heart physiology by means of an electro-fluid-structure interaction (EFSI) problem.

Firstly, we develop computational methods for simulating cardiac electrophysiology, specifically focusing on the propagation of electrical signals through the cardiac tissue. We employ the anisotropic Monodomain model, which combines a reaction-diffusion equation with various membrane models representing ionic currents. To accurately capture the behavior of these models, we propose a second-order scheme based on Strang splitting, where the nonlinear subproblem is solved by an explicit second-order predictor-corrector scheme. This scheme effectively handles the stiff gating variables and the rapid gradient increase of the action potential, resulting in improved computational efficiency.
Furthermore, we extend our computational framework by incorporating the Eikonal model. This model allows us to compute the time activation, considering the reduced computational costs associated with its implementation.

Secondly, a generalized formulation for the fluid-structure interaction (FSI) problem, which incorporates an active term expressed as active stress, is developed. This formulation draws inspiration from the Immersed Boundary Method and combines various mathematical tools. Specifically, we utilize elastodynamics equations to model the solid behavior, a high-order Navier-Stokes solver for the fluid flow, and an L^2-projection method for the transfer of velocities and forces between the fluid grid and the solid mesh.
By incorporating the active term, our formulation accurately accounts for the active mechanical contribution of the cardiac muscle. We validate the effectiveness and reliability of our approach through extensive testing, including the use of the Turek-Horn benchmark. Additionally, we simulate the filling phase of a two-dimensional idealized ventricle, where the deformed mesh obtained serves as the initial condition for simulating the active contraction stage. Throughout

these simulations, our proposed formulation consistently demonstrates its ability to extend the capabilities of FSI modeling in the context of cardiac simulations.

Lastly, we achieve the coupling between the generalized fluid-structure interaction (FSI) framework, incorporating active stress, and the electrophysiological environment by evaluating a time activation map using two different models: the reduced Eikonal model and the Monodomain model coupled with the LuoRudy ionic model.
We conduct these evaluations on a three-dimensional idealized ventricle, enabling us to observe the effects of the coupling on the cardiac system. Specifically, we compare the results obtained from a uniform contraction scenario with those obtained considering the deformations generated by the activation maps. This comparative analysis provides valuable insights into the impact of electromechanical couplings on cardiac modeling. These advancements open up possibilities for advanced electromechanical couplings in cardiac modeling, providing a more comprehensive understanding of heart physiology.

Acknowledgements

I would like to express my gratitude to Prof. Krause for his valuable guidance, expertise, and the time he dedicated to my research.
I am grateful to Dr. Maria Nestola and Dr. Marco Favino for their continuous supervision, attention, and support throughout this journey. Their suggestions and guidance have been crucial in shaping the outcome of this work.
I would like to extend my thanks to Dr. Mai Huynh for her valuable advice, expertise, and encouragement that have been immensely helpful in navigating through the challenges faced during this research. Special thanks go also to Eleonora Vercesi for her unwavering support and friendship. They have not only been exceptional colleagues but also dear friends who have made these years more enjoyable and lighthearted.
I am deeply grateful to my family for their constant presence and encouragement throughout my academic journey. Their love and belief in me have been a constant source of inspiration.
Lastly, I want to express my gratitude to Andrea for always standing by my side, his optimism, and his perpetual motivation.

Contents

Figures

Tables

Chapter 1

Introduction

Numerical cardiac models of the whole human heart have been widely studied as a support for the investigation of cardiac diseases such as arrhythmia, ischemia, and in particular rare pathologies characterized by limited experimental research involving human cardiac tissue.
Normal human heart activity involves three main physical processes: electrophysiology, active and passive mechanics, and blood dynamics. In particular, electrophysiology describes the propagation of the cardiac electrical signal, which starts in the sinoatrial node and goes through the cardiac tissue thanks to the excitable conformation of the cells. This electrical stimulus generates active forces which induce the cardiac wall to contract and pump blood throughout the circulatory system.
For this reason, the computation of an entire heart requires the combination of models that represent the distinct physiological aspects regarding the cellular electrical activity, the anisotropic and nonlinear mechanical properties of the myocardium during muscular contraction and relaxation, and the large deformations resulting in a proper space-time scale. In addition, the heart can be represented as a fluid-structure system, and taking into account the inertia of blood and the cardiac wall is needed.
Several mathematical and numerical models have been attempted to reproduce an accurate replication of the heart functions but the multiphysics interaction and the multiscale properties of the problem require high computational power, that is available in only specialized supercomputing centers, and models need to be highly optimized to solve an entire heart beat within reasonable hours.
For this reason, the majority of models focus on some specific features and many times replace the missing heart function with reduced problems or prescribe useful variables.

The most common models used for electrophysiology are the bidomain model and the reduced monodomain model, nonlinear parabolic differential partial equations describing the evolution in time of the transmembrane potential coupled with a system of ordinary differential equations representing the behavior of the gating variables of a specific ionic model. For an accurate representation of the gradient of the action potential, and in particular its depolarization phase, a fine spatial grid is required furthermore a fine temporal grid is necessary for the computation of gating variables.
In particular, BARNAFI et al. [2022] compares parallel nonlinear solvers for the solution of the Bidomain model, while Del Corso et al. [2022] proposes an electrophysiological representation of the whole heart with a GPU-accelerated solver considering the different properties of cardiac tissue including the topology and electrical conductivities.
The spatio-temporal evolution of the cardiac electrical signal results in the generation of a contraction-relaxation process and their interaction, with the passive mechanical properties of cardiac tissue, is quantitatively described by the cardiac electro-mechanical coupling model. This model combines the deformation of cardiac tissue described by a finite elasticity model, the generation of an active tension term through non-linear ordinary differential equations, the evolution of the electrical signal with Bidomain or Monodomain models coupled with several ionic membrane models including the cardiac fibers architecture (Piersanti et al. [2021]).
Several computational strategies for electromechanical coupling have been proposed (DeSimone et al. [2020]), (Usyk et al. [2002]) and have made significant developments, but the computational costs are still significant.
However, electromechanical models and their numerical formulation have been widely investigated and employed for clinical experiments, but only few works have considered the relationship between cardiac mechanics and hemodynamics.
Boundary-fitted methods are the most widely used approach, where the fluid is solved on a moving spatial domain in an Arbitrary Lagrangian-Eulerian formulation, while the solid is usually described with a Lagrangian formulation (Feng et al. [2019]),(Nordsletten et al. [2011]). However, these methods may involve large displacements and distorted fluid grids yielding complicated implementation and high computational costs.
A multi-scale heart simulation proposed by the UT-Heart simulator (Hosoi et al. [2010]) is one of the first cardiac fully coupled models published and employed for the analysis of clinical studies. Another fully coupled model focused on right and left ventricular systole offers essential information on the computational

techniques which enable the use of high-performance computing resources for cardiac simulations even though they ignore the valves and consider a simplified description of the atria (Ahmad Bakir et al. [2018]).
An immersed-boundary approach was proposed in (Viola et al. [2020]) for a coupled fluid-structure-electrophysiology left heart model involving a reduced description of force generator and setting aside the consequences due to fibers shortening.
A novel multiphysics fully coupled model has recently been proposed (Bucelli et al. [2022]) for a three-dimensional detailed description of the heart, including a closed-loop lumped-parameter model to simulate systemic and pulmonary circulation.
However, this kind of model requires extremely high computational power, complex solvers, and specific preconditioners, losing flexibility in the choice of the discretization schemes.

1.1 Research overview

This dissertation can be divided into two main parts. The first part consists of an analysis of the electrophysiological environments introducing a time integrator based on Strang splitting coupled with an explicit predictor-corrector scheme, obtaining an overall second-order numerical scheme. In particular, we apply the proposed method on a modified FitzHugh Nagumo model and compare it with a Strang splitting operator integrated with a second-order θ-method applying the Newton method for the resolution.
We also consider a three-dimensional simplified geometry of the left ventricle and evaluate the activation map related to the mechanical contraction of cardiac muscle through the implementation of the eikonal model and the Monodomain model coupled with the Luo Rudy ionic membrane model.
The second part generalizes the fluid-structure interaction problem based on the immersed-boundary method with the introduction of a time dependent active term in the elastodynamic equation referring to the solid to represent the active contribution of cardiac muscle.
The problem is then coupled with the electrophysiology creating a one-way relation that connects the time dependent active force generator term with the activation maps produced by the resolution of the eikonal model and the Monodomain model.

1.2 Contributions and limitations

The contributions of the present dissertation are multiple. In this work, we present a first attempt to represent all the physical processes involved in cardiac simulation, leading to an extremely challenging problem, especially if we consider that only interdisciplinary research groups have recently published satisfactory results.

In particular, we will first focus on the electrophysiological models where we propose a second-order numerical scheme for the time integration of the equation that describes the evolution of action potential. Starting from the operator splitting theory, where the problem is decoupled into a linear e nonlinear subproblem representing the diffusive and the reactive terms respectively, we adopt the second-order Strang splitting and combine a θ-rule of second-order accuracy for solving the linear PDE and a second-order explicit predictor correct scheme for the nonlinear system, representing an alternative opportunity compared to the classical implicit scheme as Newton or Runge-Kutta methods.
All electrophysiological models proposed have been implemented by the author inside the application $Pony$, based on the open source general purpose C++ finite element framework $MOOSE$, Multiphysics Object Oriented Simulation Environment, specifically designed for the development of multiphysics tools. $Pony$ can be extended without effort by incorporating additional ionic and mechanical models to generate active forces.

An additional contribution is represented by the introduction of a generalization of the immersed-boundary approach for FSI problems adding an active term in the elastodynamic equation for the solid which depends on the activation maps evaluated by different electrophysiological models, creating a one-way fluid-structure-electrophysiology coupling.
The immersed boundary method offers an alternative to avoid dynamic mesh generation, where the elastic structure is immersed in a viscous incompressible fluid and the fluid subproblem is described in the Eulerian form while the solid subproblem is in the Lagrangian form, involving large displacements and distorted fluid grids. In this thesis, an FSI formulation based on immersed boundary method is employed where the incompressible flow is discretized with a finite difference method and coupled with a finite element method for the resolution of the structural problem by using an L^2-projection approach.
We consider different benchmarks of an incompressible fluid past an elastic solid structure for the resolution of parallel numerical simulations which include the

time dependent active term. The Turek Hron benchmark is used for convergence studies, while a novel two-dimensional geometry is proposed for the representation of a transversal section of the left ventricle. Three-dimensional simulations offer a more realistic description of cardiac functions even though the electrophysiology and the fluid-structure interaction were performed separately.
The fluid-structure interaction algorithm is implemented in the FE framework *MOOSE*, where a Newton method is used to linearize the solid subproblem and GMRES is employed to solve the associated linear system, and it is integrated with an Object Oriented Numerics Library *MOONoLith* for the transfer of discrete fields and the flow solver IMPACT, validated and widely used for different complex flow configurations.
Future research should concentrate on advanced electromechanical couplings, including calcium concentration effects on active force generation. Additionally, a more accurate simulation of the velocity profile should be made by taking into account a more realistic ventricular geometry and integrating it with the mitral and aortic valves.
To capture important aspects of the heart's electrical activity, models for the Purkinje network should be also investigated and the implementation of an adaptive mesh refinement strategy may permit to avoid oscillations in the simulations results.
These improvements will enhance the accuracy and applicability of the simulation model, and provide a more comprehensive understanding of the heart's function.

1.3 Outline of the dissertation

In Chapter 2 we quickly introduce the bioelectric property of the cell membrane, including the description of action potential and channel gating. Then, we present a modified FiztHugh Nagumo model for the electrical activity of the heart, that effectively explains the qualitative elements of cardiac excitation, as well as some quantitative characteristics of cardiac tissue, like the action potential's form and duration, and it will be involved in the convergence studies of the proposed time integrator. Lastly, we briefly describe two membrane models for cardiac tissue that, due to their lower computing costs, are better suited to coupling with the fluid-structure problem through the evaluation of attention maps: the Monodomain model for the cardiac tissue, a reduction of the Bidomain model, consisting of only one parabolic reaction-diffusion equation that describes the evolution of the transmembrane potential and coupled with the

Luo Rudy ionic model, and the Eikonal model.
Chapter 3 is dedicated to space-time discretization techniques for the Monodomain model. In particular, we consider the finite element method for space discretization and two different approaches for time discretization: the first is a classic semi-implicit finite difference method for the reaction-diffusion equation coupled with Rush-Larsen scheme for the ODE's system (where it is permitted by the equations' form). The second is based on an operator splitting strategy coupled with a predictor-corrector scheme (Heun's method). We propose a global second order of accuracy integrator that includes an explicit scheme for the resolution of the nonlinear subproblem, complemented by a convergence analysis and compared with a common implicit scheme (second order θ method solved with a Newton method).
In Chapter 4 we give a general review of continuum mechanics in order to introduce the equations for the solid and fluid subproblems. The fluid-structure interaction issue will then be addressed by concentrating on the geometrical and physical coupling requirements. Lastly, we will introduce a generalization of the fluid-structure interaction problem based on an immersed boundary approach adding an active term into the elastodynamic equation referred to the structure's behavior.
Chapter 5 describes the space-time discretization of the FSI problem, where we adopt the finite element method for the spatial discretization of the elastodynamics equations, a finite difference method for the spatial discretization of Navier-Stokes equations, and the coupling on the interface is led by an L^2-projection variational approach. Moving on to the discretization in time, we use the Newmark approach for the solid subproblem and a third-order Runge-Kutta method for the fluid. The fluid-structure algorithm utilized to enhance the solution of the fluid-structure interaction system is presented last.
In the last Chapter, we present the numerical results of parallel numerical simulations of an incompressible fluid past an elastic solid structure using several benchmarks: a Turek-Hron benchmark for testing the generalization of the FSI problem with the active stress term, also used for convergence analysis, a two-dimensional section of left-ventricle and a three-dimensional simplified left ventricle, where a one-way electrical-fluid-structure coupling is proposed.
The main arguments of the thesis were proposed in the following conferences:

- 1^{st} Young Applied Mathematicians Conference, Santa Maria di Leuca (Le), September 13 – 17, 2021

- Young Researchers Workshop on Mathematical and Numerical Cardiac Mod-

eling, Pavia, December 14, 2021.

- COMPMAT 2022, Spring Workshop, Pavia, March 13 – 14, 2022.

-International MultiGrid Conference 2022, Multilevel Methods for Cardiac Simulations, Lugano, August 22 – 27, 2022.

- MCF2022, Modelling the Cardiac Function iHEART Conference, Cetraro, September 30 – October 2, 2022.

Chapter 2

Models of Ventricular Cardiac Cells for Electrophysiology

We start this chapter by rapidly recalling a membrane model for the ionic current, before passing to the bioelectric property of the cell membrane. After that, we give an explicit description of the most complete model of cardiac electrical activity, the Bidomain model, a system of two degenerate parabolic reaction-diffusion equations which represent the intra and the extracellular potential in the cardiac muscle, coupled with a system of ordinary differential equations describing the ionic currents. Because of its computational cost, lastly, we will see a simplified Monodomain model for the cardiac tissue, consisting of only one parabolic reaction-diffusion equation that describes the evolution of the transmembrane potential with an ionic model.

2.1 Membrane Models and Ionic Currents

The cell membrane is a protective covering of the cell that preserves the integrity of the inner environment. It is at the same time selectively permeable, permitting the free passage of some materials and restricting the passage of others. It is made up of a double layer of phospholipid molecules, in which their hydrophilic heads face the external environment as well as the internal cytosolic environment, while the hydrophobic tails face each other. Irregularly dispersed throughout the phospholipid bilayer are aggregates of globular proteins, such as structural proteins (that help to give the cell support and shape), receptor proteins (which help cells communicate with their external environment), and transport proteins (that transport molecule across the cell membrane through facilitated diffusion). The membrane also acts as a barrier to the free flow of ions

(Na^+, K^+, Cl^-) and maintains concentration differences by active mechanisms that use energy to pump ions against their concentration gradients. Differences in ionic concentrations create a potential difference across the cell membrane, on which we will focus. In fact, many cells, such as neurons and muscle cells, use the membrane potential as a signal: for example, the operation of the nervous system and muscle contraction are both dependent on the generation and propagation of electrical signals Klabunde [2011].
There are cells for which, if we apply a current for a short period of time and it is sufficiently strong, the membrane potential goes through a large excursion, called *action potential* (AP), before eventually returning to rest. Such cells are called excitable and they include precisely cardiac cells.

2.1.1 The Action Potential

When the cell is at rest, ions are distributed across the membrane in a very predictable way. For example, the concentration of Na^+ outside the cell is 10 times greater than the concentration inside. The difference in charge is described as the *resting membrane potential* and its exact value varies between cells (we will use a resting membrane potential of -84mV). Once the cell is electrically stimulated, it begins a sequence of actions involving the influx and efflux of ions that produce the action potential of the cell. There are three recognizable phases of an action potential. The first phase is the rapid *depolarization*. This phase is due to the opening of the fast Na^+ channels causing a rapid increase of the sodium membrane conductance and a rapid influx of Na^+ ions inside the cell. Thus the membrane potential is reversed from negative to positive (about +25mV). After the inactivation of the sodium channels, the transient outward current causes the small downward deflection of the action potential, and it is due to the movement of K^+ and Cl^- ions outside the cell. The second phase is called *plateau*. The influx of calcium into the cell is balanced by the efflux of potassium out of the cell through the slow delayed K^+ channels. During the third phase, the rapid *repolarization* the calcium channels close while the potassium channel remains open. As the K^+ ions start to leave the cell, the membrane potential begins to move back toward its resting value Ikonnikov et al. [2014].
From the beginning of the depolarization phase until the part way of the repolarization phase, each cell is in an absolute refractory period during which it is impossible to evoke another action potential. This is because of the inactivation gate of the sodium channel. Once that channel is back to its resting conformation, a new action potential could be started, but only by a stronger stimulus.

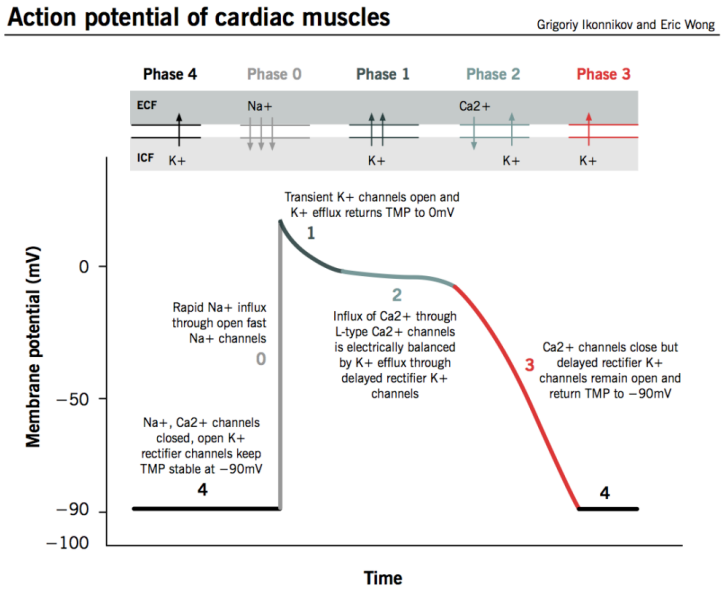

Figure 2.1. Phases of the action potential in cardiac muscles and ionic currents (Physiology of cardiac conduction and contractility, G. Ikonnikov and E. Wong, 2013)

2.1.2 Channel Gating

Each individual ion channel can be thought as a container of one or more physical subunits, called gates, that regulate the flow of ions through the channel. An individual gate can be in one of two states: open or closed. When all of the gates for a particular channel are in the open state, ions can pass through the channel and the channel is open Keener and Sneyd [2009]. If any of the gates are in the closed state, ions cannot flow and the channel is closed. A common model describes an ionic current through an open channel as a linear function of the membrane potential:

$$I_S = g_S(V - V_S) \tag{2.1}$$

where g_S is the membrane conductance and V_S is the Nernst Potential given by $V_S = \frac{RT}{zF} ln(\frac{c_e}{c_i})$, with c_e external concentration and c_i internal concentration. It is now important to determine how ionic channels open and close in response to changes in the membrane potential.
The probability for an individual gate to be open or closed depends on the value of the membrane voltage. Indeed the gate model can be described as a first-order

chemical reaction with two states:

$$\mathrm{C} \underset{\beta(V)}{\overset{\alpha(V)}{\rightleftharpoons}} \mathrm{O} \tag{2.2}$$

where C and O correspond to the closed and open states and $\alpha(V)$, $\beta(V)$ are the voltage-dependent rate constants at which a gate goes from the closed to the open and from the open to the closed states. Be w the fraction of open gates, then $1-w$ is the fraction of closed gates. From the law of mass action

$$\frac{\mathrm{d}w}{\mathrm{d}t} = \alpha(V)(1-w) + \beta(V)w = \frac{w_\infty(V)-w}{\tau(V)} \tag{2.3}$$

where $w_\infty = \frac{\alpha(V)}{\alpha(V)+\beta(V)}$ is the steady-state value of w, and $\tau(V) = \frac{1}{\alpha(V)+\beta(V)}$ is the time constant of approach to the steady-state. In the Hodgkin-Huxley model (which we will see in the next subsection) these functions were derived by fitting data.

The macroscopic conductance for a large population of channels is thus proportional to the number of channels in the open state, which is in turn proportional to the probability that the associated gates are in their open state. Thus the macroscopic conductance g_s due to channels of type s, with constituent gates of type i, is proportional to the product of the individual gating variable w_i:

$$g_s = \bar{g}_s \prod_i w_i \tag{2.4}$$

where $\bar{g}_s$ is a normalization constant that determines the maximum possible conductance when all the channels are open.

2.1.3 A Simplified Two-Variable Model

To avoid computational difficulties, R. R. Aliev and A. V. Panfilov [Aliev and Panfilov, 1996] published a simplified model for intensive 3-dimensional computations of the whole heart. They modified the FitzHugh Nagumo (FHN) model, which describes successfully qualitative aspects of excitation, including some quantitative properties of cardiac tissue such as the shape and the duration of the action potential.

FitzHugh has given a qualitative description of the Hodgkin-Huxley model [Hodgkin and Huxley, 1952], taking into account the different kinetics of the model variables: m and v are fast variables (i.e. the sodium channel activates quickly, and the membrane potential changes rapidly), while n and h are slow variables.

If we fix the slow variables at their steady-state values n_0 and h_0 it is possible

considering the behavior of the model as a function of only the two fast variables and study the process of excitation. On the other hand, to see what happens on a larger time scale, we have to consider the slow variations of the variables n and h.

A useful description of the Hodgkin-Huxley model is given by the involvement of one fast variable (assuming that m is an instantaneous function of the potential and the activation of sodium conductance performs on a faster time scale) and one slow variable (estimating $h+n \approx 0.8$ [FitzHugh, 1961]) and can be written as

$$\begin{cases} C_m \dfrac{\mathrm{d}v}{\mathrm{d}t} = -\bar{g}_{Na} m_\infty(v)^3 (0.8-n)(v-v_{Na}) - \bar{g}_K n^4 (v-v_K) - \bar{g}_L (v-v_L), \\ \dfrac{\mathrm{d}n}{\mathrm{d}t} = \alpha_n (1-n) + \beta_n n. \end{cases} \tag{2.5}$$

The Fitzhugh-Nagumo (FHN) model is a phenomenological model which captures the behavior of the fast-slow Hodgkin-Huxley model and consists of an $excitation$ variable v and a slow variable called $recovery$ variable w:

$$\begin{cases} \dfrac{\mathrm{d}v}{\mathrm{d}t} &= f(v) - w, \\ \dfrac{\mathrm{d}w}{\mathrm{d}t} &= \alpha(\beta v - \gamma w) \end{cases} \tag{2.6}$$

where $f(v)$ is a third degree polynomial and α, β and γ are real constant. The model proposed by R. R. Aliev and A. V. Panfilov consists of two equations describing the fast and slow processes:

$$\begin{cases} \dfrac{\partial v}{\partial t} &= \dfrac{\partial}{\partial x_i} d_{ij} \dfrac{\partial v}{\partial x_j} - kv(v-a)(v-1) - vw \\ \dfrac{\partial w}{\partial t} &= \epsilon(v,w)(-w - kv(v-a-1)) \end{cases} \tag{2.7}$$

where $\epsilon(v,w) = \epsilon_0 + \frac{\mu_1 w}{(v+\mu_2)}$, d_{ij} is the conductivity tensor and k, a, ϵ_0, μ_1 and μ_2 are real costant parameters.

The nonlinear term for the voltage-like variable v is a cubic function and, contrary to the FHN model, they add $-vw$ instead of $-w$, improving the description of the shape of the action potential and preventing it from becoming super-repolarized. Furthermore, the linear term used in the FHN model is replaced by a quadratic function, which is more appropriate for the heart tissue.

The model involves dimensionless variables v, w, and t. For obtaining the usual values for transmembrane potential and time the following formulae are useful:

$$E[mV] = 100v - 80 \quad t[ms] = 12.9t[t.u.] \tag{2.8}$$

The right-hand side of the equation (3.19) is similar to the FHN model. We still have a cubic function for the fast variable v and, to improve the representation of the shape of the action potential, the term uv is added. Furthermore, in the differential equation referring to the slow variable w it is used a quadratic term instead of the linear function of the FHN model. Such geometry is more appropriate for describing the heart tissue.

2.1.4 The Monodomain Model

The most complete model of cardiac electrical activity is the Bidomain model. It was first proposed in the late 1970s by Tung and Geselowitz (Tung, 1978) and it is now the generally accepted model for the electrical behavior of cardiac tissue. This model consists of two degenerate parabolic reaction-diffusion equations describing the intra u_i and the extracellular u_e potential in the cardiac muscle, coupled with a system of ordinary differential equations describing the ionic currents flowing through the cellular membrane. At the microscopic level, a model for the cellular structure of the cardiac tissue is complicated by the fact that the membrane potential, the intra and the extracellular spaces are continuously connected and intertwined. It is difficult to write equations that take into account the fine structure of the geometry of these spaces. However, it is possible to derive, by a homogenization process, a macroscopic model describing the averaged intra and extracellular electric potential and currents; see Keener and Sneyd [2009] andFranzone and Savaré [2002] for a formal derivation and modeling details.
A mathematical analysis of the Bidomain model can be found in Veneroni [2009] and in Bourgault et al. [2009b], including the study of the existence and uniqueness of the model.
Referring to Colli Franzone and Pavarino [2004], let $\Omega \subset \mathbb{R}^3$ be the bounded physical region occupied by the cardiac tissue. The intra and the extracellular medium are characterized by the conductivity tensor D_i and D_e. Because of the anisotropic structure, the conductivity is related to the arrangement of the cardiac fibers, whose direction rotates counterclockwise from the epicardium to the endocardium. It is now possible to identify three distinct principal axes at any point $\mathbf{x}$. Let $\mathbf{a}_l(\mathbf{x})$, $\mathbf{a}_t(\mathbf{x})$ and $\mathbf{a}_n(x)$ be a triplet of orthonormal vectors related to the structure of the myocardium at a point $\mathbf{x}$, with $\mathbf{a}_l(\mathbf{x})$ parallel to the local fiber direction and $\mathbf{a}_t(\mathbf{x})$ normal to the muscle sheet. Let $\sigma_l^{i,e}$, $\sigma_t^{i,e}$, $\sigma_n^{i,e}$ be the conductivity coefficients measured along the corresponding directions. In general, these coefficients may depend on $\mathbf{x}$, but we assume they are constant, i.e. we are considering homogeneous anisotropy. Then the conductivity tensors, dependent

on $\mathbf{x}$, are given by:

$$D_{i,e}(\mathbf{x}) = \sigma_l^{i,e}\mathbf{a}_l(\mathbf{x})\mathbf{a}_l^T(\mathbf{x}) + \sigma_t^{i,e}\mathbf{a}_t(\mathbf{x})\mathbf{a}_t^T(\mathbf{x}) + \sigma_n^{i,e}\mathbf{a}_n(\mathbf{x})\mathbf{a}_n^T(\mathbf{x}) \tag{2.9}$$

The total membrane current per unit volume is given by

$$I_m = \chi\left(C_m\frac{\partial v}{\partial t} + I_{ion}\right) \tag{2.10}$$

where $v = u_i - u_e$ is the transmembrane potential, the coefficient χ is the ratio of membrane area per tissue volume, C_m is the surface capacitance of the membrane and I_{ion} is the ionic current.
Imposing the conservation of currents, i.e. the interchange between the two media must balance the membrane current flow per unit volume, we have:

$$\mathrm{div}\mathbf{J}_i = -\mathrm{div}\mathbf{J}_e = I_m \tag{2.11}$$

where $\mathbf{J}_{i,e} = -D_{i,e}\boldsymbol{\nabla}u_{i,e}$ are the intra and the extracellular current densities.
Before writing the model reaction-diffusion system of PDEs, we have to describe the ionic current. We have seen how it is possible representing the ionic current through a fixed number of gating and ionic concentration variables $w := (w_1, ..., w_M)$

$$I_{ion}(v, w) = \sum_{k=1}^{N} G_k(v)\prod_{j=1}^{M} w_j^{p_{j_k}}(v - v_k(w)) \tag{2.12}$$

where N is the number of current we are considering, $G_k(v)$ is the normalize membrane conductance, v_k is the reversal potential for the kth current and p_{j_k} are integers. Recalling (2.3), the dynamics of the gating and concentration variables are described by the system of ODEs

$$\frac{\partial w_j}{\partial t} = \alpha_j(v)(1 - w_j) - \beta_j(v)(w_j) = R(v, w_j), \mathrm{with} w(\mathbf{x}, 0) = w_0(\mathbf{x}) \tag{2.13}$$

where $\alpha_j, \beta_j > 0$ and $0 \leq w_j \leq 1$.
We can now model the intra and the extracellular potential by coupling the reaction-diffusion equation (2.10) with the system of ordinary differential equations given by (2.13). Given an applied current per unit volume $I_{app}^{i,e} : \Omega \times (0, T) \longrightarrow \mathbb{R}$, where $(0, T)$ is the time interval (usually it coincides with a heartbeat) and initial conditions $v_0 : \Omega \longrightarrow \mathbb{R}, w_0 : \Omega \longrightarrow \mathbb{R}^M$ we can find the intra and the extracellular potential $u_{i,e} : \Omega \times (0, T) \longrightarrow \mathbb{R}$, the transmembrane potential $v = u_i - u_e$, the gating and ionic concentrations variables $w : \Omega \times (0, T) \longrightarrow \mathbb{R}^M$,

$c : \Omega \times (0,T) \longrightarrow \mathbb{R}^Q$ such that

$$\begin{cases} \chi C_m \dfrac{\partial v}{\partial t} - \mathrm{div}(D_i \nabla u_i) + \chi I_{ion}(v,w,c) = i^i_{app} & \text{in } \Omega \times (0,T) \\ -\chi C_m \dfrac{\partial v}{\partial t} - \mathrm{div}(D_e \nabla u_e) - \chi I_{ion}(v,w,c) = -i^e_{app} & \text{in } \Omega \times (0,T) \\ \dfrac{\partial w}{\partial t} = R(v,w) & \text{in } \Omega \times (0,T) \\ \dfrac{\partial c}{\partial t} = S(v,w,c) & \text{in } \Omega \times (0,T) \end{cases} \tag{2.14}$$

We can also assume that the cardiac tissue is insulated, therefore homogeneous Neumann boundary conditions are assigned on $\partial\Omega \times (0,T)$

$$\mathbf{n}^T D_i \boldsymbol{\nabla} u_i = 0, \mathbf{n}^T D_e \boldsymbol{\nabla} u_e = 0.$$

Initial conditions are assigned in Ω for $t = 0$

$$v(\mathbf{x},0) = u_i(\mathbf{x},0) - u_e(\mathbf{x},0) = v_0(\mathbf{x}), w(\mathbf{x},0) = w_0(\mathbf{x}). \tag{2.15}$$

Adding the first two equations of the system, we have $-\mathrm{div} D_i \boldsymbol{\nabla} u_i - \mathrm{div} D_e \boldsymbol{\nabla} u_e = I^i_{app} - I^e_{app}$. Integrating on Ω and applying the divergence theorem we have the following condition for the system to be solvable:

$$\int_\Omega I^i_{app}\,\mathrm{d}x = \int_\Omega I^e_{app}\,\mathrm{d}x \tag{2.16}$$

Concluding, the electric potentials, u_i and u_e, in bounded domains are determined up to the same additive time-dependent constant, while v is uniquely determined. The usual choice consists of selecting this constant so that u_e has zero average on Ω

$$\int_\Omega u_e\,\mathrm{d}x = 0.$$

The anisotropic *Monodomain* system is a simplified cardiac tissue model that consists of a parabolic reaction-diffusion equation describing the evolution of the transmembrane potential coupled with an ionic model. This model has been widely used for three-dimensional simulations because of its lower computational cost. For our simulations we will refer to this simplified model, considering the ionic model ranging from the Luo-Rudy model (see the previous section).
Assuming equal anisotropy ratio of the two media (λ), the Bidomain system reduces to

$$\begin{cases} \chi C_m \dfrac{\partial v}{\partial t} - \operatorname{div}(D\nabla v) + \chi I_{ion}(v,w,c) = i_{app} & \text{in } \Omega \times (0,T) \\ \dfrac{\partial w}{\partial t} = R(v,w) & \text{in } \Omega \times (0,T) \\ \dfrac{\partial c}{\partial t} = S(v,w,c) & \text{in } \Omega \times (0,T) \end{cases} \tag{2.17}$$

where $D = \frac{\lambda D}{1+\lambda}$ and $I_{app} = \frac{\lambda I^i_{app}}{1+\lambda} + \frac{\lambda I^e_{app}}{1+\lambda}$, with Neumann boundary conditions for v and initial conditions for v and w.

2.1.5 The Luo-Rudy Model

After the work of Hodgkin and Huxley, there were works done to apply their model to different cell types, including cardiac cells. The quantitative models of cardiac cells serve the purpose of reproducing the details of the action potential shape (which is different from the nerve cells action potential) while attempting to give reasonable mechanistic explanations of their behavior. The difficulty with cardiac cells is that there are many different cell types and different types of ionic channels. For example, in the ventricles, epicardial, myocardial, and endocardial cells have noticeable differences in the action potential. We recall here the phase I Luo-Rudy (LR1) model: a mathematical model of the membrane action potential of the mammalian ventricular cell. With the development of single-cell and single-channel recording techniques in the 1980s, the limitations of voltage-clamp measurements were overcome and the intracellular and extracellular ionic environments could be controlled. The data from single-channel recordings provide the basis for a quantitative description of channel kinetics and membrane ionic currents. The Luo-Rudy model focuses on the depolarization and repolarization phases of the action potential and on phenomena that involve interactions between these processes, including a periodic response of the cell to periodic stimulation. The general approach is based on a numerical reconstruction of the ventricular action potential by using Hodgkin-Huxley-type formalism and Beeler-Reuter equations [Beeler and Reuter, 1977a]. We will see that the primary difference between a ventricular cell and a Purkinje or sinoatrial nodal cell is the presence of calcium, which is needed to activate and contract the cardiac muscle.
The rate of change of membrane potential is given by (2.17) where ionic current

I_{ion} is the sum of six ionic currents: I_{Na}, a fast sodium current; I_{si}, a slow inward current; I_K, a time-dependent potassium current;I_{K1}, a time-independent potassium current; I_{Kp}, a plateau potassium current; and I_b, a time-independent background current. The ionic currents are determined by ionic gates, whose gating variables are obtained as a solution to a system of ordinary differential equations of the form(2.3).

I_{Na}: *Fast sodium current*. The model of the fast sodium channel incorporates both a slow process of recovery from inactivation and adequate maximum conductance that results in a realistic rate of membrane depolarization. They used the activation m and inactivation h parameters and it is incorporated a slow inactivation gate j to represent the slow recovery of sodium current. Thus

$$I_{Na} = \bar{g}_N a m^3 h j (V - V_{Na}) \tag{2.18}$$

I_{si}: *Slow inward current*. The slow inward current differs from the fast inward sodium current in that it is carried primarily by calcium rather than sodium, requires a more positive level of membrane potential to be activated, and has slower activation and inactivation kinetics. They have used the activation d and inactivation f gates and it can be described by

$$I_{si} = \bar{g}_{si} d f (V - V_{si}) \tag{2.19}$$

I_K: *Time-dependent potassium current*. Patch-clamp experiments showed that the I_K channel is controlled by a time-dependent activation gate x and a time-independent inactivation gate x_i. Thus

$$I_K = \bar{g}_K x x_i (V - V_K) \tag{2.20}$$

I_{K1}: *Time-independent potassium current*. It can be identified an inactivation gate $k1$ but, because its time constant is small, it can be approximated by $k1_x$, its steady-state value. Thus the I_{K1} can be formulated as follow

$$I_{K1} = \bar{g}_{K1} k1_x (V - V_{K1}) \tag{2.21}$$

The current at the plateau potentials results from a time-independent channel

I_{Kp}, which is also independent of external potassium concentration, and a background current I_b. They can be formulated as

$$I_{Kp} = \bar{g}_{Kp} Kp(V - V_{Kp}) \tag{2.22}$$

and

$$I_b = \bar{g}_b (V - V_b) \tag{2.23}$$

It can be defined the total time-independent potassium current, $I_{k1(T)}$, as

$$I_{K1(T)} = I_{K1} + I_{Kp} + I_b \tag{2.24}$$

2.1.6 Eikonal Model

An alternative way to reduce the computational costs and the complexity of the Bidomain model is to consider the Eikonal model for the propagation of action potential wavefront in the myocardium, which can be derived from the Bidomain Model by means of a perturbation technique [Keener, 1991], [Franzone and Guerri, 1993]. This model captures the main features of cardiac electrical activity regardless of one's specific ionic model.
Since the action potential has a rapid increase, the excitation wavefront involves a thin depolarized region of cardiac cells and the eikonal model can be used for evaluating the activation time at which the wavefront occupies a given position. Then, the propagation of the excited layer is characterized by the activation time function $\psi(\mathbf{x}) : \Omega \to \mathbb{R}$ that satisfies the following eikonal equation

$$c_0 \sqrt{\nabla\psi \cdot D\nabla\psi} - \nabla \cdot (D\nabla\psi) = \tau_m \qquad \text{in } \Omega \tag{2.25}$$

$$\psi = \eta \qquad \text{on } S_a \tag{2.26}$$

$$D\nabla\psi \cdot \mathbf{n} = 0 \qquad \text{on } \partial\Omega - S_a \tag{2.27}$$

where $c_0 \in \mathbb{R}$, τ_m is the membrane time costant, S_a is the physical boundary where the activation is prescribed and D is the conductivity tensor.
The Eikonal model permits to use coarser spatial resolution than the one required for the computation of the depolarization phase of the action potential by a reaction-diffusion model [Pezzuto et al., 2017] with the result of a shorter computation time.

Chapter 3

Numerical Formulation of the Electrophysiology Mathematical Problem

The Bidomain and the Monodomain models are more complex to integrate. This chapter briefly summarizes the main techniques used in literature for space and time discretization. Then we present a Monodomain space discretization based on the finite element method and two different approaches for time discretization: the first is a semi-implicit finite difference method for the reaction-diffusion equation coupled with Rush-Larsen scheme for the ODE's system. The second is an operator splitting strategy coupled with a predictor-corrector method applied to (3.19).

3.1 Space Discretization

Many different approaches have been developed for Bidomain and Monodomain space discretization. Finite difference methods have been proposed in Buist et al. [2003] and Trew et al. [2005], and Finite Elements have been extensively used [Quarteroni and Quarteroni, 2009], [Linge et al., 2009]. Recently Isogemetry Analysis has also been applied for space discretization of the Monodomain Model [Bucelli et al., 2021]

3.1.1 Variational formulation

Finite element discretization of the Monodomain model is based on the Galerkin variational formulation. Referring to Franzone et al. [2014], let V be the Sobolev

space $H^1(\Omega)$, where $\Omega \subset \mathbb{R}^3$ is the bounded physical region occupied by the cardiac tissue, and defined by

$$\begin{aligned} (\varphi, \psi) &= \int_\Omega \varphi\psi, \, dx && \forall \varphi, \psi \in L^2(\Omega) \\ a(\varphi, \psi) &= \int_\Omega (\boldsymbol{\nabla}\varphi)^T D(\mathbf{x}) \boldsymbol{\nabla}\psi \, dx && \forall \varphi, \psi \in H^1(\Omega) \end{aligned} \tag{3.1}$$

the usual L^2-inner product and elliptic bilinear forms. Now we can consider the variational formulation of the Monodomain model. Given $v_0, w_0 \in L^2(\Omega), I_{app} \in L^2(\Omega \times (0,T))$, find $v \in W^{1,1}((0,T); V)$, $w \in W^{1,1}((0,T); L^2(\Omega)^M)$, $c \in W^{1,1}((0,T); L^2(\Omega)^Q)$ such that $\forall t \in (0,T)$

$$\begin{cases} \chi C_m \dfrac{\partial}{\partial t}(v(t), \varphi) + a(v(t), \varphi) + \chi (I_{ion}(v, w), \varphi) = (I_{app}, \varphi) & \forall \varphi \in V \\ \dfrac{\partial}{\partial t}(w(t), \psi) = (R(v(t), w(t)), \psi) & \forall \psi \in L^2(\Omega)^M \\ \dfrac{\partial}{\partial t}(c(t), \zeta) = (S(v(t), w(t)), c(t), \zeta) & \forall \zeta \in L^2(\Omega)^Q \end{cases} \tag{3.2}$$

with the initial conditions $v(\mathbf{x}, 0) = u_i(\mathbf{x}, 0) - u_e(\mathbf{x}, 0) = v_0(\mathbf{x})$, $w(\mathbf{x}, 0) = w_0(\mathbf{x})$, $c(\mathbf{x}, 0) = c_0(\mathbf{x})$.

3.1.2 Finite element discretization for the Monodomain model

Let $\mathfrak{T}^h$ be a uniform triangulation of Ω and V^h the associated finite element space. It is possible to choose a finite element basis $\{\phi_i\}$ for V^h and to define the symmetric mass matrix and stiffness matrix

$$M_{ij} = \int_\Omega \phi_i \phi_j \, dx, \quad A_{ij} = \int_\Omega (\boldsymbol{\nabla}\phi_i)^T D(\mathbf{x}) \boldsymbol{\nabla}\phi_j \, dx$$

Denoting v^h, w^h, I^h_{ion} and I^h_{app} as nodal values of v, w,I_{ion} and I_{app}, the finite element discretization of the Monodomain equation needs to find the solution v^h of

$$\chi C_m M \frac{\partial v^h}{\partial t} + A v^h + \chi M I^h_{ion}(v^h, w^h) = M I^h_{app} \tag{3.3}$$

This equation is coupled with the semi-discrete approximations of the membrane model

$$\begin{cases} \dfrac{\partial w_h}{\partial t} = R(v_h, w_h) \\ \dfrac{\partial c_h}{\partial t} = S(v_h, w_h, c_h) \end{cases} \tag{3.4}$$

3.2 Time Discretization

There are several techniques for performing the time discretization of the Monodomain equations, and they involve explicit, semi-implicit, or fully implicit schemes. Some examples of explicit schemes can be found in Potse et al. [2006b] and Puwal and Roth [2007], while fully implicit methods have been considered in Murillo and Cai [2004], Munteanu and Pavarino [2009], and MUNTEANU and FRANCO PAVARINO [2007].

3.2.1 IMEX time integrator for the Monodomain system

In this section, we consider an implicit-explicit scheme that is able to combine the stability of implicit methods with the lower computational cost of explicit ones. In particular, the diffusion term is treated implicitly, while the reaction term, related to the ionic currents, is explicitly considered.
Let $\mathcal{T} = [0, T]$ be partioned into N intervals $[t^{n-1}, t^n]$ of costant time step $\tau = t^n - t^{n-1}$.
In general, the most diffused method for the time discretization of gating variables and concentrations are forward and backward Euler and Rush Larsen methods.
For the simulations of the Monodomain system coupled with the Luo-Rudy ionic model, we employ the Rush Larsen method for gating variables described by ordinary differential equations with the following form:

$$\frac{\partial w}{\partial t} = \alpha_w(v)(1-w) - \beta_w(v)w = \frac{w_\infty(V) - w}{\tau_w(v)} \tag{3.5}$$

In other words, m, h, j, d, f and x.
The Rush Larsen method assumes the action potential V constant all over the subintervals $[t^{n-1}, t^n]$. So (3.5) can be treated as a linear ODE with an exact solution given by:

$$w^n = w_\infty(v^{n-1}) + \left(w^{n-1} - w_\infty(v^{n-1})\right) e^{-\frac{\tau}{\tau_w(v^{n-1})}} \tag{3.6}$$

This method is equivalent to an explicit exponential integrator and ensures that gating variables belong to their physiological domain $[0, 1]$.
We adopt the forward Euler scheme for the remaining concentration and gating variables.
Then we can use the gating solutions for solving the Monodomain equation

$$\chi C_m \frac{v^n - v^{n-1}}{\tau} - Dv^n + \chi I_{ion}(v^{n-1}, w^n, c^n) = I_{app}(t^n) \tag{3.7}$$

It is also possible to consider a second-order scheme for the time derivative:

$$\chi C_m \frac{3v^n - 4v^{n-1} + u^{n-2}}{2\tau} - Dv^n + \chi I_{ion}(v^{n-1}, w^n, c^n) = I_{app}(t^n). \tag{3.8}$$

3.2.2 Operator Splitting

Operator Splitting is a useful technique for solving complex coupled PDE systems since they may be split into smaller parts that are easier to integrate. The class of methods we will refer to it is called $fractional\ step\ methods$.
We can consider a time interval $\mathcal{T} = [0, T]$ divided into N subintervals $[t^{n-1}, t^n]$ with a constant time step $\Delta t = t^n - t^{n-1}$ and an initial problem of the form

$$\frac{dv}{dt} = (L_1 + L_2)\, v, \quad \text{with } v(0) = v_0 \tag{3.9}$$

where L_1 and L_2 are operators and v_0 is a given initial condition.
The main idea is to consider a small time step Δt and to compute at first an approximate solution at $t = \Delta t$ of the problem

$$\frac{dv}{dt} = L_1(v), \quad \text{with } v(0) = v_0 \tag{3.10}$$

for $t \in [0, \Delta t]$.
Then we solve the problem

$$\frac{du}{dt} = L_2(u), \quad \text{with } u(0) = v(\Delta t) \tag{3.11}$$

for $t \in [0, \Delta t]$.
Let us now apply this algorithm to the Monodomain model

$$\begin{aligned} \frac{\partial v}{\partial t} &= D\nabla \cdot (\nabla v) - I_{ion}(v, w) \\ \frac{\partial w}{\partial t} &= R(v, w) \end{aligned} \tag{3.12}$$

following the scheme proposed by Qu and Garfinkel [1999a].
Then the two operator L_1 and L_2 are defined by

$$\begin{aligned} L_1 v &= -I_{ion}(v, w) \\ L_2 v &= D\nabla \cdot (\nabla v) \end{aligned} \tag{3.13}$$

noting that the nonlinear partial differential equation is reduced to a linear PDE (a diffusion problem) and a nonlinear ODE.

For the simplicity of notation, we define $v^n = v(t_n)$, the action potential at a fixed time t_n, and $w^n = w(t^n)$, the restoring variable at the time t^n. The first step of the splitting algorithm consists of solving

$$\begin{aligned} \frac{\partial v}{\partial t} &= -I_{ion}(v,w) \\ \frac{\partial w}{\partial t} &= R(v,w) \\ v(t^n) &= v^n \\ w(t^n) &= w^n \end{aligned} \tag{3.14}$$

for $t \in (t^n + \Delta t^n]$. Then we need to solve

$$\begin{aligned} \frac{\partial v}{\partial t} &= D\nabla \cdot (\nabla v) \\ v(t^n) &= v_*^n \end{aligned} \tag{3.15}$$

for $t \in (t^n, t^n + \Delta t]$, with v_*^n solution of v at $t = t^n + \Delta t$ in the previous step. This scheme, commonly referred to as Godunov splitting, is a first-order method. Hence it is of no benefit to solve the subproblem equations with greater than first-order accuracy.
A small modification permits us to make a second-order splitting algorithm: instead of solving the first step for a full-time step of length Δt, we solve the first subproblem for a time step of length $\Delta t/2$

$$\begin{aligned} \frac{\partial v}{\partial t} &= -I_{ion}(v,w) \\ \frac{\partial w}{\partial t} &= R(v,w) \\ v(t^n) &= v^n \\ w(t^n) &= w^n \end{aligned} \tag{3.16}$$

then we evaluate the solution of the second subproblem for a full-time step Δt

$$\begin{aligned} \frac{\partial v}{\partial t} &= D\nabla \cdot (\nabla v) \\ v(t^n) &= v_*^n \end{aligned} \tag{3.17}$$

with v_*^n resulting solution in the first step.
Finally, we solve the first subproblem again for a time interval of length $\Delta t/2$.

$$\begin{aligned} \frac{\partial v}{\partial t} &= -I_{ion}(v,w) \\ \frac{\partial w}{\partial t} &= R(v,w) \\ v(t^n + \Delta t/2) &= v_*^{n+1} \\ w(t^n + \Delta t/2) &= w_*^n \end{aligned} \tag{3.18}$$

where v_*^{n+1} is the solution of the action potential at the second subproblem, and w_*^n is the solution of the recovery variable in the first subproblem. This three step scheme is also known as Strang splitting.
To obtain an overall second-order accuracy of the Strang splitting, it is necessary to solve both the ODEs in the first and third steps and the PDE in the second step with at least a second-order method.

3.2.3 A second-order time integrator scheme

Starting from the Strang splitting algorithm, we combine a θ-rule of second-order accuracy for solving the linear PDE and a second-order predictor correct scheme for the nonlinear system in the first and third steps. The target is to obtain a second-order time integrator scheme.

Simplified Two-Variable Model time discretization

We apply this time integrator to the Two-variable model proposed by R. R. Aliev and A. V. Panfilov

$$\begin{cases} \frac{\partial v}{\partial t} &= d\nabla\cdot(\nabla v) - kv(v-a)(v-1) - vw \\ \frac{\partial w}{\partial t} &= \epsilon_0 + \frac{\mu_1 w}{(v+\mu_2)}(-w - kv(v-a-1)) \end{cases} \tag{3.19}$$

setting
We solve the linear PDE in the second step using a time discretization based on θ-rule, which is the most common technique used for the time discretization of PDEs. A simple finite difference approximation is used for the time derivative,

k	8.0
a	0.15
ϵ_0	0.002
μ_1	0.2
μ_2	0.3

Table 3.1. fixed parameters for numerical simulations

while the other terms are computed as weighted averages of the values from the start to the end of the time step

$$\frac{v^{n+1}-v^n}{\Delta t} = \theta\left(d\nabla\cdot(\nabla v^{n+1})\right) + (1-\theta)\left(d\nabla\cdot(\nabla v^n)\right) \tag{3.20}$$

A different accuracy is obtained for different choices of $\theta \in [0,1]$. Setting $\theta = 1/2$ we derive the Crank-Nicolson scheme, which is second-order accurate in time.

There are a large variety of methods for solving nonlinear differential systems, but we have to take into account that the cellular processes describing cardiac electrophysiology involve different time scales, making the equations stiff and challenging to solve. Implicit Runge-Kutta methods have been found suitable for time discretization of the first and third step of the splitting algorithm, but also explicit predictor-corrector schemes can be an opportunity.

In particular, we consider the problem

$$\begin{cases} \dfrac{\partial v}{\partial t} &= F(v,w) \\ \dfrac{\partial w}{\partial t} &= G(v,w) \end{cases} \tag{3.21}$$

with $F(v,w) = -kv(v-a)(v-1)-vw$ and $G(v,w) = \epsilon_0 + \frac{\mu_1 w}{(v+\mu_2)}(-w-kv(v-a-1))$ and let $v^n = v(t^n)$ and $w^n = w(t^n)$.

The predictor-corrector algorithm consists of a suitable combination of two different numerical methods (usually one explicit and the other implicit) and proceeds in two steps. First, the predictor step attempts to anticipate the function's value at a subsequent time step; then the corrector step refines the initial approximation by using a weighted average of function's values including the predicted one.

For the first predicted step, we apply the Explicit Euler method:

$$\begin{cases} v_*^{n+1} &= v^n + \Delta t F(v^n, w^n) \\ w_*^{n+1} &= w^n + \Delta t G(v^n, w^n) \end{cases} \tag{3.22}$$

with $\Delta t = t^{n+1} - t^n$.
Then we update the solution employing the predicted values v_*^{n+1} and w_*^{n+1}:

$$\begin{cases} v^{n+1} &= v^n + \Delta t F\left(\dfrac{v^n + v_*^{n+1}}{2}, \dfrac{w^n + w_*^{n+1}}{2}\right) \\ w^{n+1} &= w^n + \Delta t G\left(\dfrac{v^n + v_*^{n+1}}{2}, \dfrac{w^n + w_*^{n+1}}{2}\right) \end{cases} \tag{3.23}$$

Combing this explicit scheme for solving the nonlinear differential equation with the Crank-Nicolson method for solving the diffusion problem, we obtain an overall second-order accuracy time integrator that stands out from the common operator splitting methods for the use of a fully explicit scheme for the resolution of the nonlinear subproblem.

Benchmark and data

The computational domain considered for numerical simulations of the second-order time integrator scheme is a two-dimensional square Ω with a length side of 20[mm].

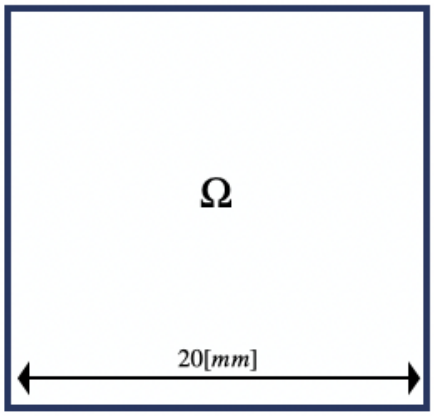

Figure 3.1. Computational domain for numerical simulations of the simplified two-variable model for cardiac action potential

Because of the stiff characteristics of the reaction-diffusion equation, we also include a smooth initial condition on a circled region on the left bottom of the computational domain

$$v_0 = v(0) = -\frac{1}{\pi}\arctan 20(x^2 + y^2 - 12.0) + 0.5 \tag{3.24}$$

This problem is independent of fibres direction and uses isotropic material properties considering the conductivity coefficient $d = 0.09529837251$. We need to recall that this simplified model involves dimensionless variables, and for obtaining the usual values, the following formulae are convenient

$$V[mV] = 100v - 80 \quad t[ms] = 12.9t[t.u.] \tag{3.25}$$

We perform the simulation on a time period $T = 38.76$[t.u.] $= 500$[ms] which is the usual action potential duration (APD) with a time step $\Delta t = 0.05$[t.u.].
We report the overtime plot of a fixed point on the domain Ω noting that compared to the usual simple model for membrane cells, the Aliev and Panfilov model is able to represent an action potential duration more similar to the cardiac one

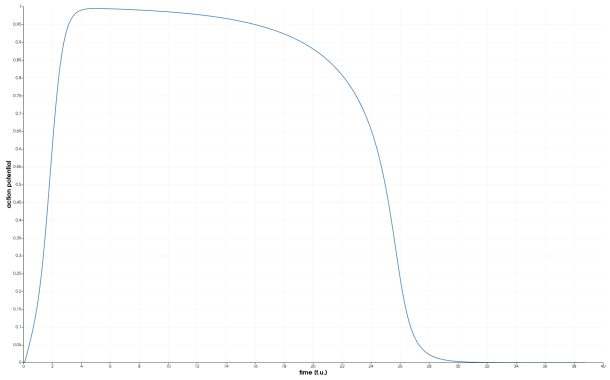

Figure 3.2. Over time plot of action potential on a fixed point of the computational

Next, we present some frames representing the evolution of action potential over the computational domain Ω showing the first depolarization phase, when the action potential reaches its pick value (nearly 20mV), and the subsequent repolarization phase characterized by the returning to the resting value after a plateau phase (typical of cardiac cells).

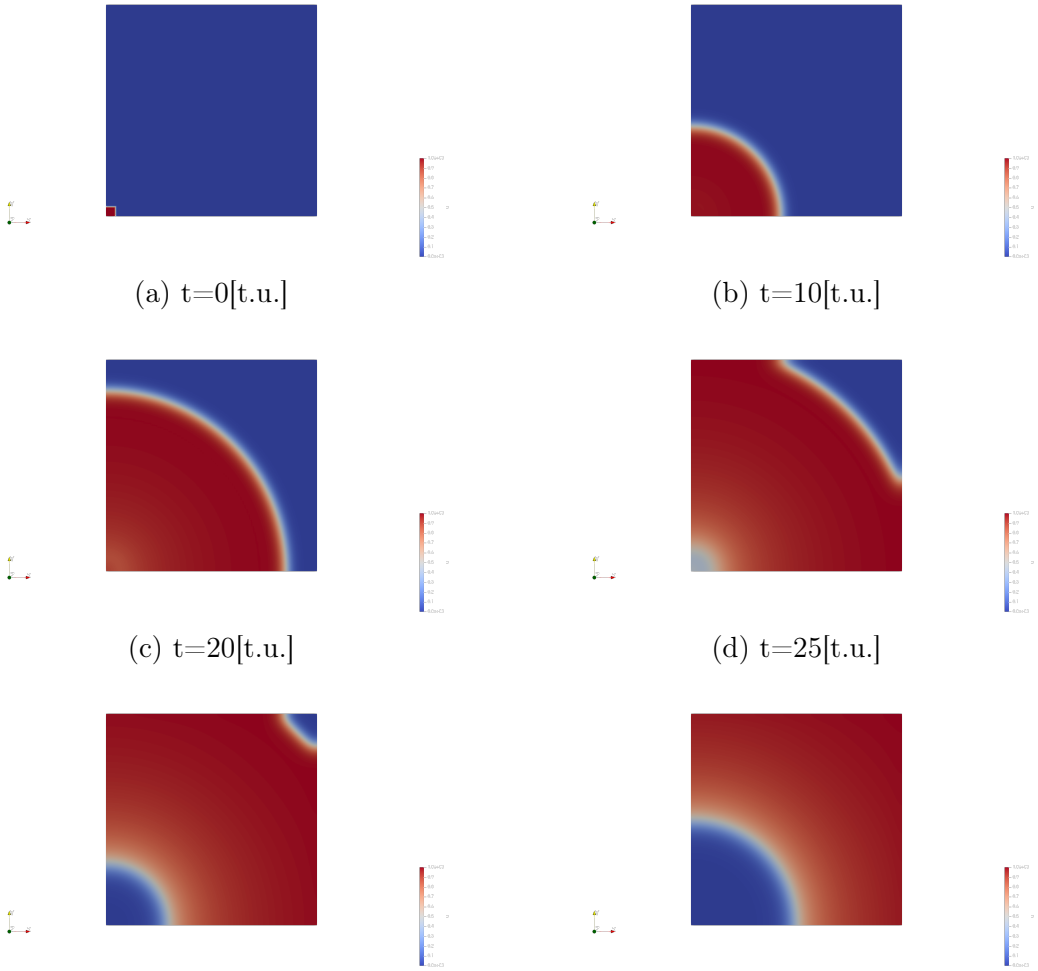

(a) t=0[t.u.] (b) t=10[t.u.]

(c) t=20[t.u.] (d) t=25[t.u.]

(e) t=30[t.u.] (f) t=35[t.u.]

Figure 3.3. Simulation of Alien and Panfilov membrane cell model with second-order time integrator scheme on a two-dimensional square

Convergence Study

Convergence results for the second-order time integrator are performed on the ICS (Institute of Computational Science) cluster (Lugano, Switzerland), composed of 42 compute nodes running CentOS 8.2.2004.x86_64 using the computational domain described in the previous section for different time step and mesh sizes.
Following Sundnes et al. [2007], the reference solution is computed with a time step $\Delta t = 0.001$ and a mesh size $h = 0.00625$ and $N = 3200 \times 3200$ elements. The table shows the L^2 norm of the errors e_{L^2} and the orders of convergence α estimated by comparing the solutions with the reference solution.

Δt	elements	e_{L^2}	α
0.25	40 × 40	0.3378	-
0.125	80× 80	0.0904	1.9024
0.0625	160× 160	0.0219	2.0433
0.03125	320× 320	0.0069	1.6742
0.015625	640× 640	0.0014	2.2842

Table 3.2. Convergence results for the monodomain model with the Aliev and Panfilov cardiac cell model

As we expected, we obtain an overall time integrator of second-order accuracy thanks to the combination of the second-order Strang splitting algorithm with the Crank-Nicolson model for the linear diffusive subproblem and the second-order predictor-corrector scheme for solving the nonlinear ODE related to the reaction term.
The proposed model can be compared to a traditional implicit time integrator based on a second-order θ-method scheme solved by the Newton method

$$\begin{cases} v_*^{n+1} & = v^n + \theta \Delta t F(v^n, w^n) + (1-\theta)\Delta t F(v^{n+1}, w^{n+1}) \\ w_*^{n+1} & = w^n + \Delta t G(v^n, w^n) + (1-\theta)\Delta t G(v^{n+1}, w^{n+1}) \end{cases} \tag{3.26}$$

with $\theta = \frac{1}{2}$.
The advantages are multiple. Even though explicit schemes have additional stability restrictions, implicit methods, like Newton, are usually time-consuming and too expensive for ionic models and refined mesh (Table2.3) In addition, the Newton method requires more than 6 iterations for the resolution of each step, while the predictor-corrector competes with only two iterations maintaining the same precision with comparable errors for different resolutions.

Δt	elements	Predictor-Corrector	Newton method
0.25	40 × 40	16.2028[ms]	16.2941[ms]
0.125	80× 80	15.7057[ms]	15.9594[ms]
0.0625	160× 160	82.8601[ms]	82.1158[ms]
0.03125	320× 320	210.447[ms]	209.554[ms]
0.015625	640× 640	811.383 [ms]	814.453[ms]
0.001	3200× 3200	50923.9[ms]	54481.8[ms]

Table 3.3. Solving time at each time step for predictor-corrector and Newton scheme on a Macbook Pro, chip M1 (ARM-based systems-on-a-chip (SoCs) designed by Apple Inc.) with 8 cores and a RAM of 16 GB.

Δt	elements	Predictor-Corrector	Newton method
0.25	40 × 40	0.2869	0.3638
0.125	80× 80	0.0696	0.0695
0.0625	160× 160	0.0180	0.0181
0.03125	320× 320	0.0068	0.0068
0.015625	640× 640	0.0010	0.0010

Table 3.4. L^2 norm errors for predictor-corrector and Newton scheme on a Macbook Pro, chip M1 (ARM-based systems-on-a-chip (SoCs) designed by Apple Inc.) with 8 cores and a RAM of 16 GB.

The described time integrator can also be applied to the Monodomain model with different ionic models.
The first step of the nonlinear subproblem can be reformulated to as:

$$\begin{cases} v_*^{n+1} & = v^n + \Delta t F(v^n, w^n, c^n) \\ w_*^{n+1} & = w^n + \Delta t G(v^n, w^n) \\ c_*^{n+1} & = c^n + \Delta t G(v^n, w^n, c^n) \end{cases} \tag{3.27}$$

with $\Delta t = t^{n+1} - t^n$.
$F(v, w, c)$ represents the ionic currents depending on gating variables w and ionic concentrations c. The second step updates the solution employing the predicted

values of v, w, and c as follows:

$$\begin{cases} v^{n+1} &= v^n + \Delta t F\left(\dfrac{v^n + v_*^{n+1}}{2}, \dfrac{w^n + w_*^{n+1}}{2}, \dfrac{c^n + c_*^{n+1}}{2}\right) \\ w^{n+1} &= w^n + \Delta t G\left(\dfrac{v^n + v_*^{n+1}}{2}, \dfrac{w^n + w_*^{n+1}}{2}\right) \\ c^{n+1} &= c^n + \Delta t G\left(\dfrac{v^n + v_*^{n+1}}{2}, \dfrac{w^n + w_*^{n+1}}{2}, \dfrac{c^n + c_*^{n+1}}{2}\right) \end{cases} \tag{3.28}$$

We need to remind that explicit schemes, instead of implicit or exponential methods, have additional stability restrictions, which result in fine mesh and smaller time steps.

3.3 Numerical simulations of electrophysiological models for cardiac cells

In this section, we will show some results of the numerical simulations of the Eikonal model and the Monodomain system with the Luo-Rudy ionic model. Both are implemented in the FE framework MOOSE [$https://github.com/Silvia-Caligari/pony.git$].
The Monodomain system is discretized using an IMEX time integrator scheme for the monodomain equation coupled with the Rush-Larsen and forward Euler methods for the resolution of the ordinary differential equations related to the gating variables and concentrations, while the Finite Element method is used for space discretization of both models (Monodomain and Eikonal) with a number of nodes N = 494762 and N = 57524 respectively.

3.3.1 Activation maps in a truncated ellipsoid

Geometry setup

The geometry we take into account is the volume contained in the endocardial and epicardial surfaces generated by the parametrization of a truncated ellipsoid proposed in Land et al. [2015a]

$$\mathbf{x} = \begin{pmatrix} x \\ y \\ z \end{pmatrix} = \begin{pmatrix} r_s \sin\phi \cos\psi \\ r_s \sin\phi \sin\psi \\ r_l \cos\phi \end{pmatrix} \tag{3.29}$$

where for the $endocardial\ surface$:

$$r_s = 7[\text{mm}] \quad r_l = 17[\text{mm}] \quad \phi \in [-\pi, -\arccos\frac{5}{17}] \quad \psi \in [-\pi, \pi]$$

and for the $epicardial\ surface$:

$$r_s = 10[\text{mm}] \quad r_l = 20[\text{mm}] \quad \phi \in [-\pi, -\arccos\frac{5}{20}] \quad \psi \in [-\pi, \pi]$$

with a base plane fixed at $z = 5[\text{mm}]$. The solid is then scaled by a factor 0.0025 and the base plane is set at $x = 0.005[\text{m}]$ and centered in $(0.005, 0.035, 0.035)$ in anticipation with FSI simulations where solid structure and fluid domain are expressed in meters. Space discretization in Eikonal simulation consists of 324376 $\mathbb{P}_1$ elements and 61216 nodes, while because of the stability properties of the Monodomain system, we consider a finer mesh for the simulation involving the

Monodomain equation coupled with LR1 model. The solid is discretized with 2595008 $\mathbb{P}_1$ elements and 460935 nodes

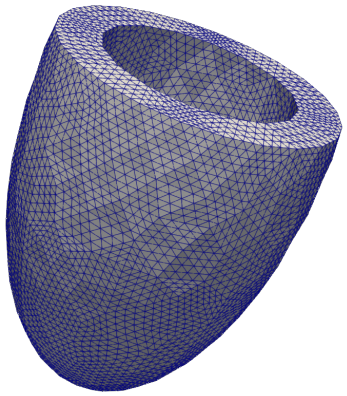

Figure 3.4. Volumetric geometry between the endocardial and epicardial surface

Eikonal model

We first evaluate the activation map generated by the Eikonal model (see Chapter 2). Because we don't include the activity of the Purkinje network, we apply stimuli at three different points on the epicardium. For the one-way electro-

$\sigma_l/C_m\chi$	$\sigma_t/C_m\chi$	$\sigma_n/C_m\chi$	c_0	τ_m
0.0001529	0.0000699	0.0000225	8.27	0.09

Table 3.5. Three-dimensional Eikonal parameters

fluid-structure coupling, we shift the activation of cardiac muscle according to the solution of the Eikonal equation (Chapter 6).
The inclusion of the fiber orientation plays a fundamental role in the propagation of the electrical signal since the electrical propagation velocity differs along the fiber and cross-fiber directions.

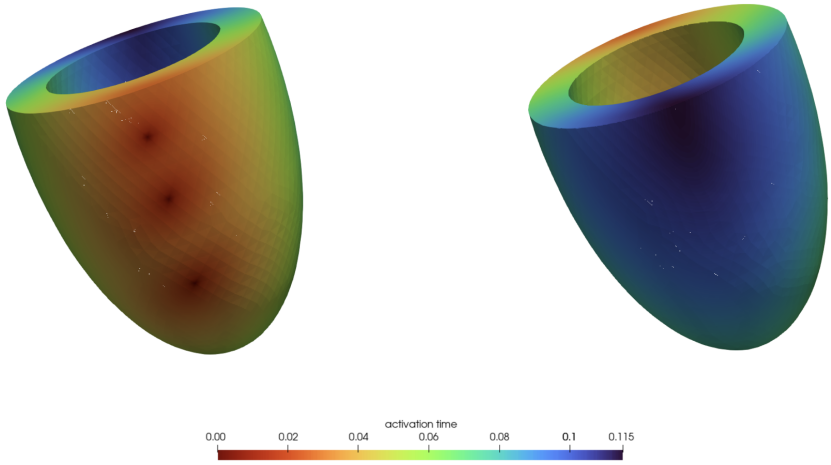

Figure 3.5. Eikoanl Model. Activation map in the three-dimensional left ventricle

In this thesis, we estimate the fibres orientation following the approach presented in Potse et al. [2006a], where we introduce a normalized coordinate that is null for points on the epicardium and equal to one for points on the endocardium of the left simplified ventricle.

Monodomain system coupled with Luo-Rudy ionic model

Differently from sinoatrial node (SAN) cells, which are a group of cardiac pacemaker cells located on the right atrium and able to reach autonomously excitation, ventricle cells need a proper electrical stimulus.
If the stimulus is below the threshold value (nearly -60mV), the transmembrane potential returns to its resting value. If the stimulus is above the threshold value, depolarization starts, and transmembrane potential increases.
Because our geometry consists of a simplified left ventricle, we need to apply an electrical stimulus at three different points on the epicardial surface (I_{app} in the Monodomain equation (2.17)).
In particular, we introduce an applied current $I_{app} = 50$ [mA/cm^3] for 2 [ms].

$\sigma_l[\Omega^{-1}cm^{-1}]$	$\sigma_t[\Omega^{-1}cm^{-1}]$	$\sigma_n[\Omega^{-1}cm^{-1}]$	$\chi[\ cm^{-1}]$	$C_m[mF/cm^2]$
0.0012	0.000225	0.00005	1000	0.001

Table 3.6. Three-dimensional Monodomain parameters

The model is run for 10000 time steps of 0.05 [ms], and coefficients are reported

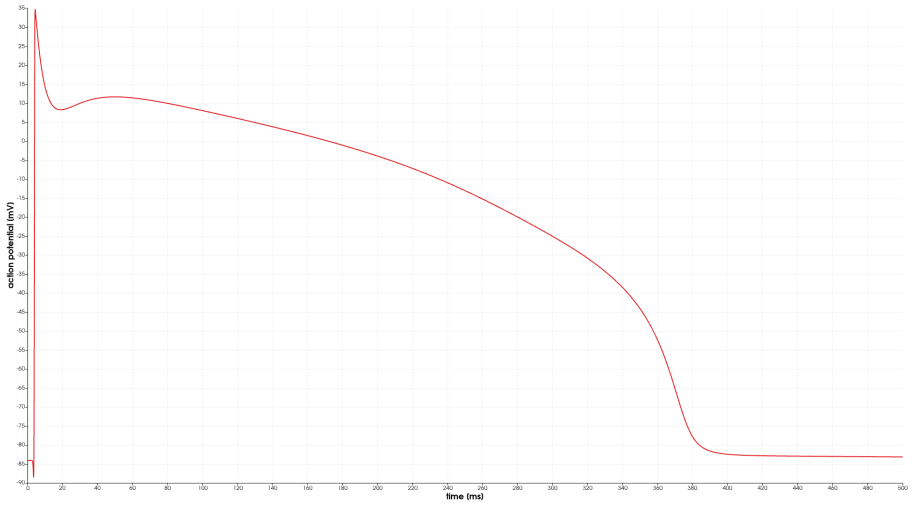

Figure 3.6. Action potential profile on a fixed point on the epicardial surface

in Table 3.6. We evaluate the voltage, the gating variables and concentrations, and the activation time at each time step.

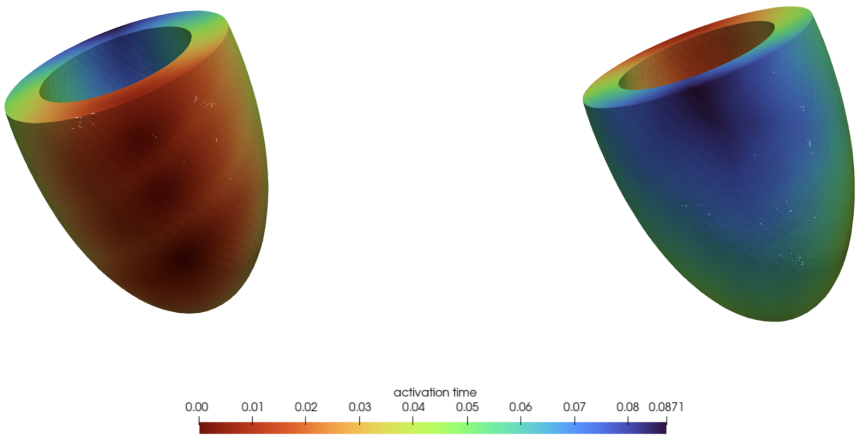

Figure 3.7. Monodomain with LR1 model. Activation map in the three-dimensional left ventricle

Chapter 4

Governing equations in Fluid-Structure Interaction Problem with Active Force

Fluid-structure interaction (FSI) is a multiphysics interaction between a deformable or moving structure and a surrounding external or internal fluid flow exchanging energy through an interface.
The FSI mathematical problem needs to account for the physical and geometrical interaction. At the numerical level, this calls for suitable methods able to maintain stability and accurately manage the coupling efficiently between the two subproblems.
First, we will present an overview of the fundamentals of continuum mechanics for introducing subsequently the equations related to the solid and fluid subproblems separately. Then we will describe the fluid-structure interaction problem by focusing on geometrical and physical coupling conditions.
Traditional FSI formulations typically focus on the coupling between fluid flow and passive elastic structures. However, to comprehensively study the fluid-structure interaction phenomena in cardiac models, it is essential to develop a generalized FSI framework that incorporates the active behavior of the cardiac muscle. In this chapter, we present an extension to the elastodynamic equations in the context of FSI, introducing an active term that accounts for the structure's behavior due to active contraction.

4.1 Fundamentals of continuum mechanics

In this section, we will briefly review the main principles of continuum mechanics, starting from introducing the notions of a continuum body and internal forces leading to the definitions of deformation map and stress tensor field. Then we

will report the main balance laws useful for the representation of the constitutive models for hyperelastic solids, also investigating materials reinforced by a family of fibers.

4.1.1 Kinematics

It is possible to make a basic assumption about any material body, ignoring its atomic structure, modeling the material involved as a continuum: at any fixed instant t, a material body can be identified as an open set $B \subset \mathbb{E}^3$ and each particle with a point $\mathbf{x} \in B$.
Let us assume that the mass of a body B is continuously distributed, and any subset of B has positive mass with positive volume and define a mass density field per unit volume $\rho : \Omega \subset B \to \mathbb{R}$ such that

$$\mathsf{mass}[\Omega] = \int_{\Omega} \rho(\mathbf{x}) dV \tag{4.1}$$

where Ω is an open subset of B and dV denote an infinitesimal volume element at $\mathbf{x} \in \Omega$.
Furthermore, the force field, exerted by an external presence, on a body B per unit volume can be given by a function $\hat{\mathbf{b}}(\mathbf{x}) : B \to \mathscr{V}$, then the resultant force on an open subset of B, Ω, is defined by

$$\mathbf{r}_b[\Omega] = \int_{\Omega} \hat{\mathbf{b}}(\mathbf{x}) dV \tag{4.2}$$

In the same way, it is used the term surface force to denote a force, per unit area, along a bounding surface of a body or an imaginary surface within the interior of a body. Let Γ be an oriented surface in B with a unit normal field $\mathbf{n} : \Gamma \to \mathscr{V}$, the surface force is given by a function $\mathbf{t}_\mathbf{n} : B \to \mathscr{V}$ called traction or surface force field.
The resultant force due to a surface force field on an oriented surface Γ is defined as

$$\mathbf{r}_s[\Gamma] = \int_{\Gamma} \mathbf{t}_\mathbf{n}(\mathbf{x}) dA \tag{4.3}$$

where dA represents an infinitesimal surface area element at $\mathbf{x} \in \Gamma$.
In particular the traction field $\mathbf{t}_\mathbf{n}$ depends only pointwise on the unit normal field $\mathbf{n}$ and there is a traction function $\mathbf{t} : \mathscr{N} \times B \to \mathscr{V}$ such that $\mathbf{t}_\mathbf{n} = \mathbf{t}(\mathbf{n}(\mathbf{x}), \mathbf{x})$, where $\mathscr{N} \subset \mathscr{V}$. The Cauchy's Theorem makes more evident the dependence of the traction function $\mathbf{t}(\mathbf{n}, \mathbf{x})$ from $\mathbf{n}$ and it is fundamental for the definition of the

Cauchy stress field for a body B.
Let $\mathbf{t} : \mathcal{N} \times B \to \mathcal{V}$ be a traction function for a body B satisfying the law of action and reaction, then $\mathbf{t}(\mathbf{n}, \mathbf{x})$ is linear in $\mathbf{n}$ and for each $\mathbf{x} \in B$ exists a second-order tensor $\mathbf{S}(\mathbf{x}) \in \mathcal{V}^2$ such that

$$\mathbf{t}(\mathbf{n}, \mathbf{x}) = \mathbf{S}(\mathbf{x})\mathbf{n} \tag{4.4}$$

The nine components of the stress tensor can be interpreted as the components of the traction vectors $\mathbf{t}(\mathbf{e}_j, \mathbf{x})$, where $\mathbf{e}_j$ are the normals on the coordinate planes at $\mathbf{x}$. In other words, the traction vectors represent the surface forces per unit area on an infinitesimal cube centered at $\mathbf{x}$.
Now we can proceed to introduce the main definitions and principles of deformation and motion that causes stresses or are caused by stresses in a material body. First of all, we consider a reference frame at a fixed origin O with an orthonormal basis $\{\mathbf{E}_i\}_{i=1,\dots,3}$. As the body B moves in space $\mathbb{E}^3$, at a given time t it occupies a sequence of geometrical regions which are called $configurations$ of B at that time t and are determined uniquely at any instant of time. When the position of a point $\mathbf{X}$ corresponds to a fixed reference time, the region occupied by the body is referred to as reference configuration and coordinates $\mathbf{X} = (X_1, X_2, X_3)$ are labeled as material coordinates. If we assume that this region moves into a new region at a subsequent time t, this new configuration is called current (or deformed) configuration, and particles may be identified by the position vector $\mathbf{x} = (x_1, x_2, x_3)$ and usually named ad spatial coordinates. If the motion is described by the material coordinates, it is said to be a material description of the motion or Lagrangian description. At the same time, the spatial description or Eulerian description is referred to a characterization of the motion in terms of spatial coordinates. In fluid mechanics, it is usually used the Eulerian description on the other hand, the Lagrangian description is often preferred for describing the constitutive behavior of solids.
A deformation is a vector field χ that maps points $\mathbf{X}$ located in the reference configuration to points $\mathbf{x}$ in the current configuration

$$\mathbf{x} = \chi(\mathbf{X}, t). \tag{4.5}$$

It is assumed to be uniquely invertible with the inverse motion denoted by χ^{-1}.

Thus it can be defined the displacement of a material particle from its initial location $\mathbf{X}$ to its final location $\mathbf{x}$ in the material description

$$\mathbf{U}(\mathbf{X}, t) = \mathbf{x} - \mathbf{X} = \chi(\mathbf{X}, t) - \mathbf{X}. \tag{4.6}$$

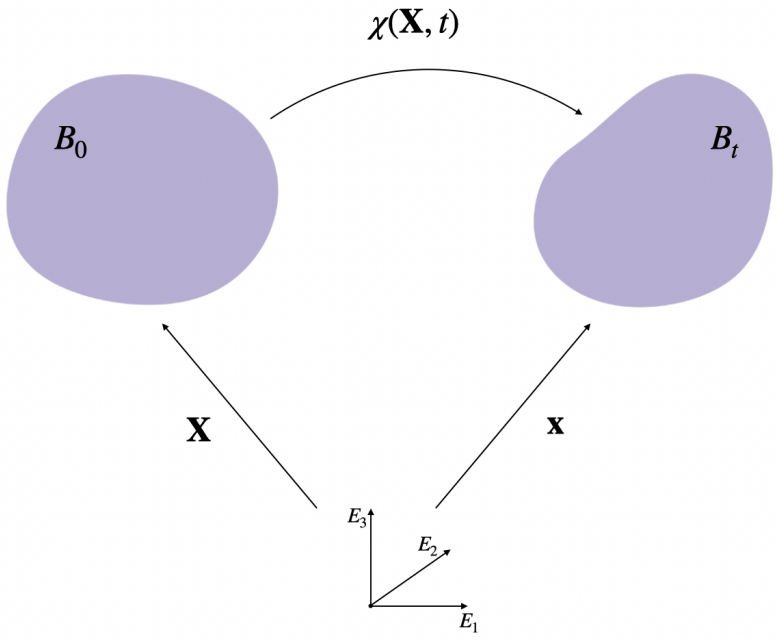

Figure 4.1. Deformation map between the reference configuration B_0 and the current configuration B_t

A principal measure of deformation is the deformation gradient, defined as

$$d\mathbf{x} = \mathbf{F}(\mathbf{X}, t)d\mathbf{X}, \quad \text{where } \mathbf{F}(\mathbf{X}, t) = \frac{\partial \chi(\mathbf{X}, t)}{\partial \mathbf{X}} \tag{4.7}$$

which describes a linear transformation generating a vector $d\mathbf{x}$ by the action of a second-order tensor $\mathbf{F}$ on a vector $d\mathbf{X}$. If we assume the existence of the inverse motion, then the inverse of the deformation gradient $\mathbf{F}^{-1}$ can be defined.
It could be useful to derive a relation able to transform integrals defined in material coordinates to integrals over the corresponding spatial coordinates and vice-versa. Let us consider an infinitesimal volume element dV at the point $\mathbf{X}$ in the reference configuration and the corresponding volume element dv at the point $\mathbf{x}$ in the current configuration. The infinitesimal volume dV can be represented as a triple scalar product of the three vectors based $d\mathbf{X}_1, d\mathbf{X}_2$ and $d\mathbf{X}_3$, then $dV = (d\mathbf{X}_1 \times d\mathbf{X}_2) \cdot d\mathbf{X}_3$. Recalling the definition of the deformation gradient (4.7) and noting that the infinitesimal vectors $d\mathbf{x}_1, d\mathbf{x}_2$ and $d\mathbf{x}_3$ can be used to

define the volume element dv we obtain

$$\begin{aligned} dv &= (d\mathbf{x}_1 \times d\mathbf{x}_2) \cdot d\mathbf{x}_3 = (\mathbf{F}(\mathbf{X},t)d\mathbf{X}_1 \times \mathbf{F}(\mathbf{X},t)d\mathbf{X}_2) \cdot \mathbf{F}(\mathbf{X},t)d\mathbf{X}_3 \\ &= \det(\mathbf{F}(\mathbf{X},t))(d\mathbf{X}_1 \times d\mathbf{X}_2) \cdot d\mathbf{X}_3 = \det(\mathbf{F}(\mathbf{X},t))dV \end{aligned} \tag{4.8}$$

We define $J(\mathbf{X},t) = \det(\mathbf{F}(\mathbf{X},t))$ known as Jacobian determinant. Since $\mathbf{F}$ is invertible then $J(\mathbf{X},t) = \det(\mathbf{F}(\mathbf{X},t)) \neq 0$ and because volume elements can not have negative volume, $J(\mathbf{X},t) > 0$ for all points $\mathbf{X}$ and time t.
The infinitesimal volume in the current configuration can be expressed as a dot product

$$dv = ds \cdot d\mathbf{x} \tag{4.9}$$

that can be rewritten as

$$(\mathbf{F}^T ds - J(\mathbf{X},t)ds) \cdot d\mathbf{X} = 0 \tag{4.10}$$

So we find the relation between the infinitesimal areas on the current and reference configurations, known as Nanson's formula

$$ds = J\mathbf{F}^{-T} dS \tag{4.11}$$

Changes in material elements during motion can be expressed in the form of second-order strain tensors, of which many definitions and names have been proposed in literature. Following Holzapfel [2002], we will present the most common definitions.
Let $\mathbf{a}_0$ be the unit vector at the position $\mathbf{X}$ in the reference configuration, describing the direction of a material line element (such as fibre), and $d\mathbf{X}$ the length of the material line element. The stretch vector in the direction of $\mathbf{a}_0$ is defined as

$$\lambda_{\mathbf{a}_0}(\mathbf{X},t) = \mathbf{F}(\mathbf{X},t)\mathbf{a}_0 \tag{4.12}$$

The modulus $\lambda = |\lambda_{\mathbf{a}_0}|$ is called stretch, and if we evaluate the square, we obtain

$$\lambda^2 = \mathbf{a}_0 \cdot \mathbf{F}^T\mathbf{F}\mathbf{a}_0 = \mathbf{a}_0 \cdot \mathbf{C}\mathbf{a}_0 \tag{4.13}$$

where $\mathbf{C} = \mathbf{F}^T\mathbf{F}$ is the symmetric and positive define right Cauchy-Green tensor. The inverse of the Cauchy-Green tensor $\mathbf{B} = \mathbf{C}^{-1}$ is called Piola deformation tensor.
Another strain measure is the change in the squared lengths in the direction of $\mathbf{a}_0$ at a point $\mathbf{X}$

$$\frac{1}{2}[(\lambda|d\mathbf{X}|)^2 - (|d\mathbf{X}|)^2] = d\mathbf{X} \cdot \mathbf{E} \tag{4.14}$$

with $\mathbf{E} = \frac{1}{2}(\mathbf{F}^T\mathbf{F} - \mathbf{I})$ the Green-Lagrange strain tensor.
An instant consequence of deformation and motion is stress, which is often responsible for the deformation of materials and is fundamental in continuum mechanics.
As we have seen in (4.4), surface tractions can be expressed in terms of stress fields acting on a normal vector for both material and spatial description. Then we define **t** the Cauchy traction vector, the force measured per unit surface area in the current configuration, and **T** the first Piola-Kirchoff traction vector, the force measured per unit surface area in the reference configuration. For the Cauchy's stress theorem, there exist second-order tensors so that

$$\begin{aligned} \mathbf{t}(\mathbf{x}, t, \mathbf{n}) &= \sigma(\mathbf{x}, t)\mathbf{n} \\ \mathbf{T}(\mathbf{X}, t, \mathbf{N}) &= \mathbf{P}(\mathbf{x}, t)\mathbf{N} \end{aligned} \tag{4.15}$$

where σ is the Cauchy stress tensor and **P** is called first Piola-Kirchoff stress tensor.
Because it is not convenient to work with stress tensors expressed in spatial coordinates in problems involving solids, it is possible to find a relation between the Cauchy stress tensor and the first Piola-Kirchoff stress tensor known as Piola transformation

$$\mathbf{P} = J\sigma\mathbf{F}^{-T} \tag{4.16}$$

4.1.2 Balance principles

In this section, we will recall the main balance principles applying to any material and fundamental in continuum mechanics.
As we have already observed (4.1), an integral expression of a mass of a body includes a continuous scalar field representing the mass density per unit volume. Let $\rho_0(\mathbf{X})$ be the reference mass density and $\rho(\mathbf{x}, t)$ the spatial mass density. Because mass can not be produced or destroyed (in the case of non-relativistic physics), it is a conserved quantity; in particular, if an element has a fixed mass in the reference configuration, then it must maintain the same mass during its motion. This statement is known as conservation of mass and can be expressed as

$$\text{mass}[\Omega_0] = m = \int_{\Omega_0} \rho_0(\mathbf{X}) dV = \int_{\Omega} \rho(\mathbf{x}, t) dv \tag{4.17}$$

for all times. Then,

$$\frac{Dm}{Dt} = \frac{D}{Dt} \int_{\Omega} \rho(\mathbf{x}, t) dv = 0 \tag{4.18}$$

From (4.8), it is possible to rewrite this relation as

$$\int_{\Omega_0} [\rho_0(\mathbf{X}) - \rho(\chi(\mathbf{X},t),t)J(\mathbf{X},t)]dV = 0 \tag{4.19}$$

The arbitrariness of Ω_0 allows to convert the integral equality into the pointwise one

$$\rho_0(\mathbf{X}) = \rho(\chi(\mathbf{X},t),t)J(\mathbf{X},t) \tag{4.20}$$

Before introducing the next balance principles, let us consider a set of particles occupying a region Ω with volume $V_\mathbf{x}$, with a motion given by $\mathbf{x} = \chi(\mathbf{X},t)$, a smooth spatial velocity field $\mathbf{v} = \mathbf{v}(\mathbf{x},t)$, a spatial mass density field $\rho = \rho(\mathbf{x},t)$ and a smooth spatial scalar field $\phi = \phi(\mathbf{x},t)$ describing a physical quantity per unit volume at a time t.
The status of the continuum body subjected to the scalar field ϕ may be characterized by the integral function

$$I(t) = \int_\Omega \phi(\mathbf{x},t)dv \tag{4.21}$$

If we want to compute the material time derivate of $I(t)$, we need to transform the integral in terms of variables that refer to the reference configuration since the region Ω depends on time

$$\begin{aligned} \frac{D}{Dt}I(t) &= \frac{D}{Dt}\int_{\Omega_0} \phi(\chi(\mathbf{X},t),t)J(\mathbf{X},t)dV \\ &= \int_{\Omega_0}\left[\frac{D}{Dt}\phi(\chi(\mathbf{X},t),t)J(\mathbf{X},t) + \phi(\chi(\mathbf{X},t),t)\frac{D}{Dt}J(\mathbf{X},t)\right]dV \end{aligned} \tag{4.22}$$

Then, if we convert the volume integral to the current configuration $dv = J(\mathbf{X},t)dV$:

$$\begin{aligned} \frac{D}{Dt}\int_\Omega \phi(\mathbf{x},t) &= \int_\Omega \left[\frac{D}{Dt}\phi(\mathbf{x},t) + \phi(\mathbf{x},t)\frac{\frac{D}{Dt}J(\mathbf{X},t)}{J(\mathbf{X},t)}\right]dv \\ &= \int_\Omega \left[\frac{D}{Dt}\phi(\mathbf{x},t) + \phi(\mathbf{x},t)\nabla\cdot\mathbf{v}(\mathbf{x},t)\right]dv \\ &= \int_\Omega \left[\frac{\partial\phi(\mathbf{x},t)}{\partial t} + \nabla\cdot(\phi(\mathbf{x},t)\mathbf{v}(\mathbf{x},t))\right]dv \end{aligned} \tag{4.23}$$

Applying the divergence theorem

$$\frac{D}{Dt}\int_\Omega \phi(\mathbf{x},t) = \int_\Omega \frac{\partial\phi}{\partial t}dv + \int_{\partial\Omega}\phi\mathbf{v}\cdot\mathbf{n}ds \tag{4.24}$$

The first term on the right-hand side represents the local time rate of change of the spatial field ϕ, while the second term describes the outward normal flux of $\phi\mathbf{v}$ across the surface $\partial\Omega$. This relation is known as Reynolds transport theorem, and it is fundamental for the derivation of conservation principles. Applying the theorem to (4.18), it is possible to obtain the rate form of continuity mass equation in the spatial description

$$\frac{D}{Dt}\int_{\Omega}\rho(\mathbf{x},t)dv=\int_{\Omega}\frac{\partial\rho}{\partial t}+\nabla\cdot(\rho\mathbf{v})dv=0 \tag{4.25}$$

and because of the arbitrariness of the volume, it follows that

$$\frac{\partial\rho}{\partial t}+\nabla\cdot(\rho\mathbf{v})=0 \tag{4.26}$$

We now define the linear momentum

$$\mathbf{L}(t)=\int_{\Omega}\rho(\mathbf{x},t)\mathbf{v}(\mathbf{x},t)dv \tag{4.27}$$

and the angular momentum at a fixed point $\mathbf{x}_0$

$$\mathbf{J}(t)=\int_{\Omega}\mathbf{r}\times\rho(\mathbf{x},t)\mathbf{v}(\mathbf{x},t)dv \tag{4.28}$$

with $\mathbf{r}=\mathbf{x}-\mathbf{x}_0$.
The linear and angular momentum balance principles are generalizations of the first and second principles of motions in continuum mechanics, then the contributions to linear and angular momentum are due to external sources, $\mathbf{F}(t)$ and $\mathbf{M}(t)$, which represent the resultant force and the resultant moment (i.e., the moment of $\mathbf{F}(t)$ at a fixed point $\mathbf{x}_0$) respectively.
The resultant force in the current configuration is given by the additive form

$$\mathbf{F}(t)=\int_{\partial\Omega}\mathbf{t}ds+\int_{\Omega}\mathbf{b}dv \tag{4.29}$$

where $\mathbf{t}$ represents the Cauchy traction vector and $\mathbf{b}$ the volumetric force field. Then, the conservation of linear momentum reads as

$$\begin{aligned}\frac{D}{Dt}\mathbf{L}(t)&=\frac{D}{Dt}\int_{\Omega}\rho(\mathbf{x},t)\mathbf{v}(\mathbf{x},t)dv=\mathbf{F}(t)\\&=\int_{\Omega}\mathbf{b}dv+\int_{\partial\Omega}\mathbf{t}ds\end{aligned} \tag{4.30}$$

and the momentum balance as

$$\begin{aligned}\frac{D}{Dt}\mathbf{J}(t) &= \frac{D}{Dt}\int_{\Omega}\mathbf{r}\times\rho(\mathbf{x},t)\mathbf{v}(\mathbf{x},t)dv = \mathbf{M}(t)\\ &= \int_{\Omega}\mathbf{r}\times\mathbf{b}dv + \int_{\partial\Omega}\mathbf{r}\times\mathbf{t}ds\end{aligned} \tag{4.31}$$

The Cauchy stress theorem ensures the existence of a second-order tensor $\sigma(\mathbf{x},t)$ such that $\mathbf{t}(\mathbf{x},t,\mathbf{n}) = \sigma(\mathbf{x},t)\mathbf{n}$. Applying the divergence theorem to (4.30), we obtain the Cauchy's first equation of motion

$$\int_{\Omega}[\nabla\cdot\sigma + \mathbf{b} - \rho(\mathbf{x},t)\frac{D}{Dt}\mathbf{v}(\mathbf{x},t)]dv = 0 \tag{4.32}$$

and by assuming Ω is arbitrary, we have the local relation

$$\nabla\cdot\sigma + \mathbf{b} = \rho(\mathbf{x},t)\frac{D}{Dt}\mathbf{v}(\mathbf{x},t) \tag{4.33}$$

Since working with material coordinates is usually more convenient, we would rewrite the Cauchy equation of motion in terms of coordinates related to the reference configuration.
First of all, we need to introduce the Piola identity

$$\nabla\cdot(J\mathbf{F}^{-1}) = 0 \tag{4.34}$$

which combined with Piola transformation (4.16), gives us the transformation of the first Piola-Kirchhoff stress tensor

$$\nabla\cdot\mathbf{P} = J\nabla\cdot\sigma \tag{4.35}$$

After a change of variables (and using the relation $dv = JdV$), the resultant Cauchy's first equation of motion in material coordinates reads as

$$\int_{\Omega_0}[\nabla\cdot\mathbf{P} + \mathbf{B} - \rho_0(\mathbf{X})\frac{D}{Dt}\mathbf{V}(\mathbf{X},t)]dV = 0 \tag{4.36}$$

The fundamental equations introduced are essential for characterizing kinematics, stress, and balance principles and are valid for any continuum body. For this reason, they do not permit to distinguish one material from another, and we need to establish additional equations in the form of constitutive laws to specify the material properties we take into account.

A constitutive law should approximate the physical behavior of a material under specific conditions of interest. It is usually considered a phenomenological approach that describes the macroscopic nature of the material as continua. The main idea is to fit mathematical equations to experimental data even though the relation of mechanism of deformation with the microscopic physical structure of the material is not possible.
If the constitutive equations regard physical objects like fluid, we call the field of continuum mechanics *fluid mechanics*; on the other hand, if the constitutive equations are valid for solids is known as *solid mechanics*.

4.2 Mathematical modeling of the solid problem

Usually, the elastodynamic equations referred to the solid are written in the Lagrangian framework, with respect to an observer that moves with the structure displacement.
Then, let $\hat{\Omega}_s \subset \mathbb{R}^3$ be a bounded Lipschitz domain representing the reference configuration of the solid body and $\hat{\mathbf{x}}_s \in \hat{\Omega}_s$ the material position. To pass to the current configuration for scalar and vectorial functions, we need to consider the unique deformation vector field $\chi : \hat{\Omega}_s \times [0,T] \to \mathbb{R}^3$ such that $\mathbf{x}_s = \chi(\hat{\mathbf{x}}_s, t)$, where $\mathbf{x}_s$ is the current position in the current configuration $\Omega_s(t)$ of the solid structure.

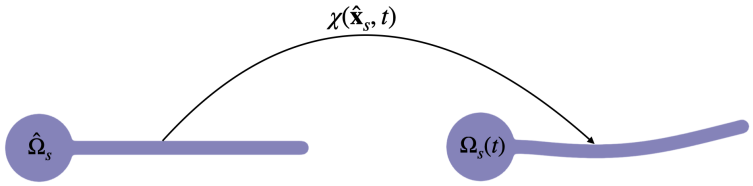

Figure 4.2. Reference configuration and current configuration of the solid domain.

The boundary $\partial\hat{\Omega}_s$ is split into the Dirichlet $\hat{\Gamma}_D$ and Neumann $\hat{\Gamma}_N$ parts, such that $\partial\hat{\Omega}_s = \hat{\Gamma}_D \cup \hat{\Gamma}_N$ and $\hat{\Gamma}_D \cap \hat{\Gamma}_N = \emptyset$.
The behavior of the solid structure is then described by the following mathematical problem

$$\rho_s \frac{\partial^2 \hat{\mathbf{u}}_s}{\partial t^2} - \hat{\nabla} \cdot \hat{\mathbf{P}} = \mathbf{b} \qquad \text{in } \hat{\Omega}_s \tag{4.37}$$

$$\hat{\mathbf{u}}_s = \hat{\mathbf{u}}_b \qquad \text{on } \hat{\Gamma}_D \tag{4.38}$$

$$\hat{\mathbf{P}}\hat{\mathbf{n}} = \hat{\Psi} \qquad \text{on } \hat{\Gamma}_N \tag{4.39}$$

where the vectorial function $\hat{\mathbf{u}}_s = \hat{\mathbf{u}}_s(\hat{\mathbf{x}}_s, t)$ is the displacement field, ρ_s is the mass density per unit undeformed volume, $\hat{\mathbf{P}}(\hat{\mathbf{u}}_s)$ is the first Piola-Kirchoff stress tensor, $\hat{\nabla}\cdot$ is the divergence operator computed in the reference configuration, the vectorial function $\mathbf{b}$ represents the volume force per unit volume acting on the solid and $\hat{\mathbf{u}}_b$, $\hat{\Psi}$ are two given suitable vectorial functions.

The relation between the stress tensor $\hat{\mathbf{P}}$ and the displacements $\hat{\mathbf{u}}_s$ (usually nonlinear) is the constitutive law and characterizes the material properties chosen for the solid structure.
Since this relation involves the gradient of the displacements, the elastodynamics equations form a system of three hyperbolic partial differential equations.
The first Piola-Kirchoff stress tensor $\hat{\mathbf{P}}$ of the reference configuration and the Cauchy stress tensor σ_s of the current configuration are related by the Piola transformation

$$\hat{\mathbf{P}} = J\sigma_s \mathbf{F}^{-T}$$

where $\mathbf{F}^{-T}$ is the deformation tensor and $J = \det(\mathbf{F})$ is the Jacobian determinant defining the changes of volumes between the reference and the current configurations ($J = 1$ means no change in volume).
When the relation between the first Piola-Kirchoff stress tensor $\hat{\mathbf{P}}$ and the displacement field $\hat{\mathbf{u}}_s$ is linear, we have perfectly linear elastic material, and the relationship is also known as Hooke's law. This law is used only for small displacements as a consequence of the linearization of a general material.
In particular, we have

$$\hat{\mathbf{P}}(\hat{\mathbf{u}}_s) = 2\mu\varepsilon(\hat{\mathbf{u}}_s) + \lambda\nabla\cdot\hat{\mathbf{u}}_s\mathbf{I} \tag{4.40}$$

where $\varepsilon(\mathbf{v}) = \frac{1}{2}(\nabla\mathbf{v} + \nabla\mathbf{v}^T)$ and the material parameters μ and λ are known as the Lamè constants, and μ is also called the shear modulus. They both have the dimensions of pressure, and they measure a solid's ability to withstand deformation: λ and μ take large values for "hard" materials like steel or diamond, and lower values for "soft" materials like rubber.
Often they are written in terms of the Young modulus E and Poisson ratio υ

$$\lambda = \frac{E\upsilon}{(1+\upsilon)(1-\upsilon)}, \quad \mu = \frac{E}{1+\upsilon} \tag{4.41}$$

E accounts for the elastic properties while υ for the degree of incompressibility ($\upsilon = \frac{1}{2}$ means incompressible material).
A nonlinear constitutive theory suitable to describe a class of materials that respond elastically even when they are subjected to large deformations is known as finite hyperelasticity theory.
The main characteristic of this theory is the postulation of the existence of a Helmholtz free-energy function Ψ, which is defined per unit reference volume.
If the energy function depends only on the deformation gradient $\Psi(\mathbf{F})$ or some strain tensor, it is referred to as the strain-energy function, which we assume to be continuous.
We restrict our attention to the case of homogeneous material, that is, the distributions of internal components are assumed to be uniform. For this type of

material, the strain-energy function is a function of only the deformation gradient **F**, while for non-homogeneous material (heterogeneous material), the strain-energy function Ψ will depend additionally on the position of a particle in the structure.
A hyperelastic material is characterized by the following relation determining the first Piola-Kirchoff stress tensor

$$\hat{\mathbf{P}} = \frac{\partial \Psi}{\partial \mathbf{F}} \tag{4.42}$$

In this work, we will consider three different benchmarks for fluid-structure interaction simulations: the two-dimensional Turek-Hron benchmark Turek and Hron [2006], a two-dimensional idealized left ventricle, and a three-dimensional idealized left ventricle.
For the two-dimensional simulations, we consider the Saint-Venant-Kirchoff constitutive relation, which reads as follows

$$\Psi = \frac{\lambda_s}{2}[Tr(\hat{\mathbf{E}})]^2 + \mu_s Tr(\hat{\mathbf{E}}^2) \tag{4.43}$$

where $\hat{\mathbf{E}} = \frac{1}{2}(\hat{\mathbf{F}}^T\hat{\mathbf{F}} - \mathbf{I})$ is the Green-Lagrangian strain tensor, $Tr(\cdot)$ is the trace operator, λ_s and μ_s are the constitutive parameters (see Table 6.1 and Table 6.5).
For the three-dimensional ventricle, we consider the Guccione-Costa constitutive law [Guccione et al., 1995] to model the elastic behavior of the human ventricle with the constitutive parameters derived from Nikou et al. [2015] (reported in Table 6.7). To fulfill the nearly incompressibility condition of soft tissue, the penalty technique is employed. In this method, a volumetric energy term $\Psi_V(\hat{J}) = 1/2\kappa(\hat{J}-1)^2$ is added to the expression of the strain energy function Ψ with κ representing the penalty coefficient.

Weak formulation of solid subproblem

Let

$$\hat{V} = \left\{\hat{\phi} \in \left[H^1(\hat{\Omega}_s)\right]^3 : \hat{\phi}_{|\Gamma_D} = \mathbf{0}\right\}$$
$$\hat{V}_b = \left\{\hat{\phi} \in \left[H^1(\hat{\Omega}_s)\right]^3 : \hat{\phi}_{|\Gamma_D} = \hat{\mathbf{u}}_b\right\}$$

suitable spaces of vector functions.
The weak formulation of the elastodynamic equation with boundary conditions read:

Find $\hat{\mathbf{u}}_s \in \hat{V}_b$ with $\hat{\mathbf{u}}_s(\hat{\mathbf{x}_s}, 0) = \hat{\mathbf{u}}_{s,0}$ and $\frac{\partial \hat{\mathbf{u}}_s}{\partial t}(\hat{\mathbf{x}_s}, 0) = \hat{\mathbf{v}}_{s,0}$ such that for each time

$$\left(\rho_s \frac{\partial^2 \hat{\mathbf{u}}_s}{\partial t^2}, \hat{\phi}\right) - \left(\hat{\nabla} \cdot \hat{\mathbf{P}}, \hat{\phi}\right) = \left(\hat{\mathbf{b}}, \hat{\phi}\right) \tag{4.44}$$

where $(\cdot, \cdot)$ is the $L^2(\hat{\Omega}_s)$ inner product.
Integrating by parts we obtain

$$\left(\rho_s \frac{\partial^2 \hat{\mathbf{u}}_s}{\partial t^2}, \hat{\phi}\right) - \left(\hat{\nabla} \cdot \hat{\mathbf{P}}, \hat{\phi}\right) = \left(\hat{\mathbf{b}}, \hat{\phi}\right) \int_{\hat{\Gamma}_N} \hat{\Psi} \hat{\phi} \, dS_{\hat{\mathbf{x}}} \tag{4.45}$$

4.3 Mathematical modeling of the fluid problem

Let $\Omega_f \subset \mathbb{R}^3$ be a fixed bounded domain representing the current configuration of the fluid domain. To allow for the Dirichlet and Neumann boundary conditions, the boundary $\partial\Omega_f$ is split into the Dirichlet Γ_D and Neumann Γ_N parts, such that $\partial\Omega_f = \Gamma_D \cup \Gamma_N$ and $\Gamma_D \cap \Gamma_N = \emptyset$.
The Navier-Stokes equations for an incompressible and homogeneous (the fluid density is constant in space and time) fluid read for $\mathbf{x} \in \Omega$, $t \in (0, T]$

$$\begin{cases} \rho_f \dfrac{D\mathbf{v}_f}{Dt} - \nabla \cdot \mathbf{T}_f(\mathbf{v}_f, p_f) = \mathbf{b}_f \\ \nabla \cdot \mathbf{v}_f = 0 \end{cases} \tag{4.46}$$

with the initial condition $\mathbf{v}_f(\mathbf{x}, 0) = \mathbf{v}_{0,f}(\mathbf{x})$ and boundary conditions

$$\begin{aligned} \mathbf{v}_f &= \mathbf{v}_b \quad \text{on } \Gamma_D \\ \mathbf{T}_f(\mathbf{v}_f, p_f)\mathbf{n} &= \boldsymbol{\Psi} \quad \text{on } \Gamma_N \end{aligned} \tag{4.47}$$

where $\mathbf{v}_b$ and $\boldsymbol{\Psi}$ are suitable given data, $\mathbf{n}$ is the outward unit normal to $\partial\Omega_f$, $\frac{D}{Dt}$ is the material derivative, $\mathbf{v}_f = \mathbf{v}_f(\mathbf{x}, t) : \Omega_f \times (0, T] \to \mathbb{R}^3$ the vectorial function representing the fluid velocity, $p_f = p_f(\mathbf{x}, t) : \Omega_f \times (0, T] \to \mathbb{R}^3$ the scalar function representing the pressure of the fluid, $\mathbf{T}_f$ is the Cauchy stress tensor formed by a viscous part depending on $\mathbf{v}_f$ and a hydrostatic part depending on p_f.
We restrict our attention to incompressible Newtonian fluids, characterized by a linear relation

$$\mathbf{T}_f(\mathbf{v}_f, p_f) = \mu_f \left(\nabla \mathbf{v}_f + (\nabla \mathbf{v}_f)^T\right) - p_f \mathbf{I} \tag{4.48}$$

where μ_f is the constant fluid viscosity.
If we recall the definition of the material derivative

$$\frac{D\mathbf{v}_f}{Dt} = \frac{\partial \mathbf{v}_f}{\partial t} + \mathbf{v}_f \cdot \nabla \mathbf{v}_f$$

we have for an incompressible Newtonian fluid the point-wise form of Navier-Stokes equations in an Eulerian formulation

$$\begin{cases} \rho_f \dfrac{\partial \mathbf{v}_f}{\partial t} + \rho_f(\mathbf{v}_f \cdot \nabla \mathbf{v}_f) - \mu_f \Delta \cdot \mathbf{v}_f + \nabla p_f = \mathbf{b}_f \\ \nabla \cdot \mathbf{v}_f = 0 \end{cases} \tag{4.49}$$

The Navier-Stokes equations are four scalar equations in the four unknows $\mathbf{v}_{f,x}$, $\mathbf{v}_{f,y}$, $\mathbf{v}_{f,z}$ and p_f. The first three equations describe the conservation of momentum, while the last one the conservation of mass.
Notice that if $\Gamma_N = \emptyset$ we have

$$0 = \int_{\Omega_f} \nabla \cdot \mathbf{v}_f d\mathbf{V}_\mathbf{x} = \int_{\partial\Omega_f} \mathbf{v}_f \cdot \mathbf{n} d\mathbf{S}_\mathbf{x} = \int_{\partial\Omega_f} \mathbf{v}_b \cdot \mathbf{n} d\mathbf{S}_\mathbf{x} \tag{4.50}$$

Moreover, p_f is defined up to a constant, and for this reason, it is usually required that $\int_{\Omega_f} p_f d\mathbf{V}_\mathbf{x} = 0$.

Weak formulation of fluid subproblem

Assume $\Gamma_N \neq \emptyset$, $\mu \in L^\infty(\Omega_f)$,$\mathbf{v}_b \in \left[H^{\frac{1}{2}}(\Gamma_D)\right]^3$, $\mathbf{\Psi} \in \left[L^2(\Gamma_D)\right]^3$ for almost each time and set

$$\begin{aligned} V &= \left\{\phi \in \left[H^1(\Omega_f)\right]^3 : \phi_{|\Gamma_D} = \mathbf{0}\right\} \\ V_b &= \left\{\phi \in \left[H^1(\Omega_f)\right]^3 : \phi_{|\Gamma_D} = \mathbf{v}_b\right\} \\ Q &= L^2(\Omega) \end{aligned}$$

where the equality in the first set is in the sense of the trace and notice that if $\Gamma_N = \emptyset$ then $Q = L^2_0(\Omega) = \left\{q \in Q : \int_\Omega q = 0\right\}$. Thus, the weak formulation of Navier-Stokes equations for an incompressible Newtonian fluid reads almost each time: Find $\mathbf{v} \in V_b$ and $p \in Q$ such that

$$\begin{cases} \left(\dfrac{\partial \mathbf{v}}{\partial t}, \phi\right) + ((\mathbf{v} \cdot \nabla \mathbf{v}), \phi) - \left(\mu_f \Delta \cdot \mathbf{v}, \phi\right) + (\nabla p, \phi) = (\mathbf{b}, \phi) \quad \forall \phi \in V \\ (\nabla \cdot \mathbf{v}, q) = 0 \quad \forall q \in Q \end{cases} \tag{4.51}$$

where the fluid density ρ_f is fixed at 1 without any loss of generality and $(\cdot,\cdot)$ is the $L^2(\Omega)$ inner product.
Integrating by parts and recalling Gauss theorem, we obtain the following relations

$$-\int_\Omega \mu_f \Delta \mathbf{v}\cdot\phi = \int_\Omega \mu_f \nabla\mathbf{v}\cdot\nabla\phi - \int_{\partial\Omega} \mu_f \frac{\partial \mathbf{v}}{\partial \mathbf{n}}\cdot\phi$$

$$\int_\Omega \nabla p\cdot\phi = -\int_\Omega p\nabla\cdot\phi + \int_{\partial\Omega} p\phi\cdot\mathbf{n}$$

and we get

$$\begin{cases} \left(\frac{\partial \mathbf{v}}{\partial t},\phi\right) + ((\mathbf{v}\cdot\nabla\mathbf{v}),\phi) + \left(\mu_f\nabla\mathbf{v},\nabla\phi\right) - (p,\nabla\cdot\phi) = (\mathbf{b},\phi) + \int_{\Gamma_N}\psi\cdot\phi \quad \forall\phi\in V \\ (\nabla\cdot\mathbf{v},q) = 0 \quad \forall q\in Q \end{cases} \tag{4.52}$$

From this formulation, it is clear the role of the Lagrange multiplier played by p.

4.4 Fluid-structure interaction problem

The interaction between a flowing fluid and an immersed or surrounded solid structure is the base of different physical phenomena with applications in distinct fields of engineering, such as the aerospace industry, construction projects, and biomedical research.
Fluid–structure interaction problems are often too complex to solve analytically, and so they have to be analyzed by numerical simulations. There exist two principal approaches for the resolution of fluid-structure interaction problems. One consists of a monolithic scheme, where a single solver is used for both the fluid and solid governing equations simultaneously. The other one solves each subproblem separately with two distinct numerical solvers.
The main difficulties related to the numerical simulation of fluid-structure interaction problems regard the presence of a two-field problem where the common boundary of the fluid and structure subdomains is an unknown of the problem, the choice and analysis of interface coupling conditions which need to ensure no-slip conditions, i.e., perfect adherence between particles of the fluid and structure, through the continuity of the velocity on the interface and the third Newton law, namely the action-reaction principle implying that the surface forces exerted by the fluid at the interface should be compensated by that exerted by the structure, through the continuity of stress on the interface. Lastly, all the

complications due to the material properties of the solid structure may induce large deformations and the transition from laminar to turbulent flow.
We now introduce the governing equations describing the fluid-structure interaction problem in a Newtonian fluid.

Let $\Omega_f(t)$ and $\Omega_s(t)$ the current configurations of the fluid domain and solid, respectively, such that $\Omega = \Omega_f(t) \cup \Omega_s(t)$ is the computational domain and let $\Gamma^{fsi}(t)$ be the fluid-structure interaction interface.

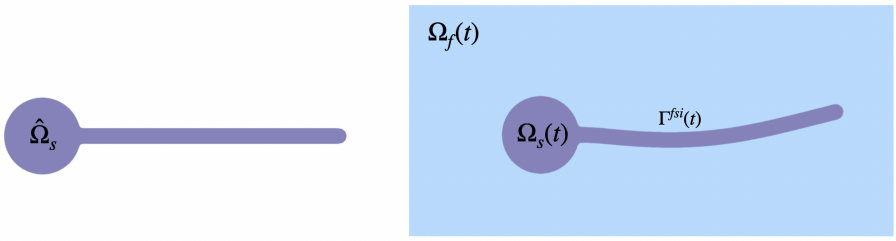

Figure 4.3. Reference configuration of the solid domain on the left. Current configurations of structure $\Omega_s(t)$ and fluid domain $\Omega_f(t)$ and fluid-structure interaction interface $\Gamma^{fsi}(t)$ on the right

A Lagrangian formulation is adopted for the elastodynamics equations representing the structure behavior, while the Navier-Stokes equations are written using the Eulerian formulation.
Let $\hat{\Omega}_s \subset \mathbb{R}^3$ a bounded domain representing the reference configuration of the solid structure. The material $\hat{\mathbf{x}}_s \in \hat{\Omega}_s$ and spatial $\mathbf{x}_s \in \Omega_s(t)$ positions are linked through a unique deformation vector field over a time integral $[0, T]$ such that $\chi : \hat{\Omega}_s \times [0, T] \to \mathbb{R}^3$ and $\mathbf{x}_s = \chi(\hat{\mathbf{x}}_s, t)$.
For granting Dirichlet boundary conditions as well as coupling conditions on the interface, the boundary $\partial\hat{\Omega}_s$ is disjointed into the Dirichlet $\hat{\Gamma}_s^D$ and fluid-structure interaction $\hat{\Gamma}^{fsi}$ parts, such that $\partial\hat{\Omega}_s = \hat{\Gamma}_s^D \cup \hat{\Gamma}^{fsi}$ and $\hat{\Gamma}_s^D \cap \hat{\Gamma}^{fsi} = \emptyset$.
The same considerations need to be done for the fluid subproblem, then the boundary of the fluid domain $\partial\Omega_f(t)$ is split into the Dirichlet $\Gamma_f^D$and FSI $\Gamma^{fsi}(t)$boundary such that $\partial\Omega_f = \Gamma_f^D \cup \Gamma^{fsi}(t)$ and $\Gamma_f^D \cap \Gamma^{fsi}(t) = \emptyset$.

Thus, the fluid-structure interaction problem read as

$$\rho_s \frac{\partial^2 \hat{\mathbf{u}}_s}{\partial t^2} - \hat{\nabla} \cdot \hat{\mathbf{P}} = \mathbf{b} \qquad \text{in } \hat{\Omega}_s \tag{4.53}$$

$$\rho_f \frac{\partial \mathbf{v}_f}{\partial t} + \rho_f (\mathbf{v}_f \cdot \nabla \mathbf{v}_f) - \mu_f \Delta \cdot \mathbf{v}_f + \nabla p_f = \mathbf{b}_f \qquad \text{in } \Omega_f \tag{4.54}$$

$$\nabla \cdot \mathbf{v}_f = 0 \qquad \text{in } \Omega_f \tag{4.55}$$

with initial conditions

$$\hat{\mathbf{u}}_s(\hat{\mathbf{x}}_s, 0) = \hat{\mathbf{u}}_s^0 \qquad \text{in } \hat{\Omega}_s \tag{4.56}$$

$$\frac{\partial \hat{\mathbf{u}}_s}{\partial t}(\hat{\mathbf{x}}_s, 0) = \frac{\partial \hat{\mathbf{u}}_s^0}{\partial t} \qquad \text{in } \hat{\Omega}_s \tag{4.57}$$

$$\mathbf{v}_f(\mathbf{x}, 0) = \mathbf{v}_f^0 \qquad \text{in } \Omega_f \tag{4.58}$$

and boundary conditions

$$\hat{\mathbf{u}}_s = \hat{\mathbf{u}}_b \qquad \text{on } \hat{\Gamma}_s^D \tag{4.59}$$

$$\mathbf{v}_f = \mathbf{v}_b \qquad \text{on } \Gamma_f^D \tag{4.60}$$

$$\mathbf{v}_f = \frac{\partial \hat{\mathbf{u}}_s}{\partial t} \qquad \text{on } \Gamma^{fsi}(t) \tag{4.61}$$

$$\hat{J}^{-1} \hat{\mathbf{P}} \hat{\mathbf{F}}^T \mathbf{n} = \sigma_f \mathbf{n} \qquad \text{on } \Gamma^{fsi}(t) \tag{4.62}$$

where ρ_s is the mass density per unit volume, $\hat{\mathbf{u}}_s$ is the displecement field, $\hat{\mathbf{P}}$ is the first Piola-Kirchoff stress tensor, $\hat{\nabla}\cdot$ is the material divergence operator, ρ_f is the fluid density, μ_f is the fluid viscosity, $\mathbf{v}_f$ is the fluid velocity field, p_f is the fluid pressure and $\hat{\mathbf{u}}_b$ is a given suitable boundary vectorial function.
Equations (4.91) and (4.92) guarantee the continuity of the velocity and force equilibrium on the interface $\Gamma^{fsi}(t)$, with $\hat{\mathbf{F}}$ deformation gradient, $\hat{J}$ the corresponding determinant $\hat{J} = \det(\hat{\mathbf{F}})$,$\sigma_f$ is the Cauchy stress for the Newtonian fluids depending on $\mathbf{v}_f$ and p_f, $\mathbf{n}$ is the outward normal to the structure boundary of the current configuration.

4.4.1 Immersed boundary approach

The resolution of fluid-structure interaction problems often involves evaluating the fluid dynamic equations in the moving domain. Various approaches have been investigated to overcome the difficulties related to the reconstruction of the mesh at each time step.

The Arbitrary Lagrangian-Eulerian (ALE) method is one of the most used, usually coupled with the solid structure analyzed in a Lagrangian fashion. Although this approach has been used successfully with accurate results at the interface between solid and fluid, its implementation is expensive since the mesh follows the movement of the solid, adapting its shape to the structure's behavior. If the movements are too large, they may be involved large deformation of elements such that the accuracy of the solution and numerical stability can be affected.
A completely different approach was introduced by Peskin [Peskin, 1977] to study the blood flow in the heart, known as immersed boundary method (IBM). One of the advances proposed by this method is the use of a fixed cartesian mesh for the fluid and an independent immersed structure. The method proposed was based on the finite difference for the spatial discretization, which employs two independent grids: one for the Eulerian formulation of the fluid problem and the other for the Lagrangian variables related to the immersed boundary.

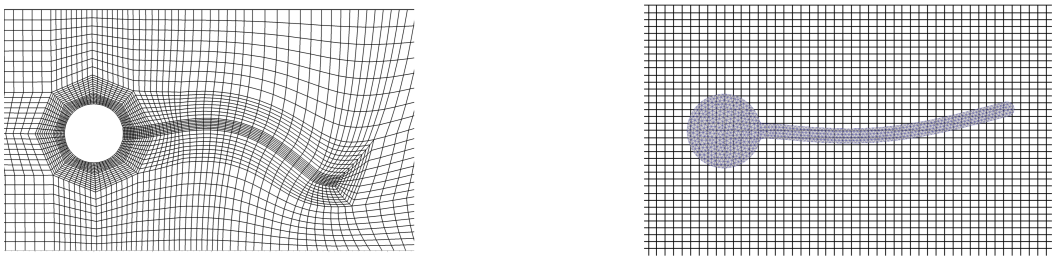

(a) ALE approach (b) Immersed boundary method

Figure 4.4. Two approaches for managing fluid-structure interaction coupling. (4.4a) represents the distorted mesh due to ALE method. (4.4b) represents the cartesian grid mesh for the fluid and the independent immersed structure for the immersed boundary method [Nestola et al., 2019]

In the immersed boundary method, the immersed solid body is modelled as an elastic incompressible material in two or three-dimensional space or simply in the form of a closed curve or surface. The presence of the structure is taken into account by thinking of the solid as a part of the fluid where additional forces are applied, and additional mass is located.
The equations involved are the modified Navier-Stokes equations

$$\begin{cases} \rho_f \dfrac{\partial \mathbf{v}_f}{\partial t} + \rho_f(\mathbf{v}_f \cdot \nabla \mathbf{v}_f) - \mu_f \Delta \cdot \mathbf{v}_f + \nabla p_f = \mathbf{F} \\ \nabla \cdot \mathbf{v}_f = 0 \end{cases} \tag{4.63}$$

where $\mathbf{F}$ is a vector field representing the force density of the solid acting on the

fluid.
The mass density of the immersed structure can be described through a Lagrangian mass density $M(\hat{\mathbf{x}}_s)$, where $\hat{\mathbf{x}}_s$ denotes the Lagrangian coordinates in the reference configuration of the solid structure. This term represents the difference between the mass of the elastic structure and the displaced mass of the fluid due to the presence of a solid.
Thus, the force exerted on the fluid and the fluid density can be expressed involving a smoothed approximation of the Dirac delta function δ

$$\rho(\mathbf{x},t) = \rho_f + \int_{\hat{\Omega}_s} M(\hat{\mathbf{x}}_s)\delta(\mathbf{x} - \chi(\hat{\mathbf{x}}_s,t)dV_{\hat{\mathbf{x}}} \tag{4.64}$$

$$\mathbf{F}(\mathbf{x},t) = \int_{\hat{\Omega}_s} \mathbf{f}(\hat{\mathbf{x}}_s,t)\delta(\mathbf{x} - \chi(\hat{\mathbf{x}}_s,t)dV_{\hat{\mathbf{x}}} \tag{4.65}$$

where **F** is the force term on the right-hand side of the Navier-Stokes equation and **f** considers the solid material's elasticity properties.
At each time step, only the fluid system with the added force term need to be solved, which means a reduction of the computational cost. However, a consistent approximation of the Dirac delta function is difficult to find. Peskin proposed a discrete Dirac delta function that must be continuous (for guaranteeing the continuity of the velocity and the applied force on the immersed boundary), have a compact and smallest possible support, and be exact for linear interpolation.

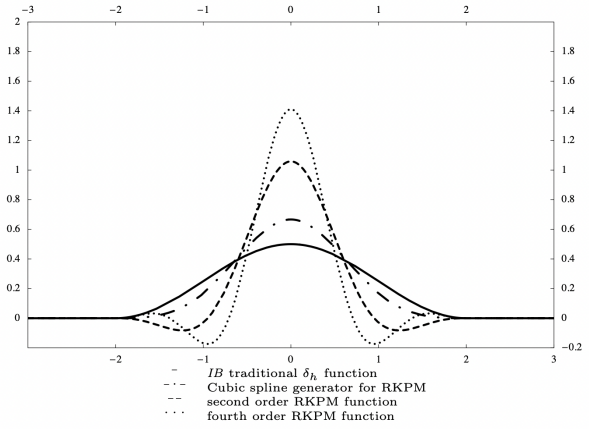

Figure 4.5. Traditional discrete Dirac delta function $\frac{1}{4}(1+\cos(\frac{\pi r}{2}))$ and more recent reproducing kernel particle method

Since the original immersed boundary method was proposed by Peskin, various

other methods based on this approach have been developed. For example, several attempts have been made to consider a finite element formulation for both fluid and solid discretization, adopting also reproducing particle method to approximate the Dirac delta function [Glowinski and Kuznetsov, 2007] or involving the Dirac delta function in a variational way [Boffi and Gastaldi, 2003], so there is no need of approximating.
This dissertation has been considered a framework inspired by the immersed boundary method able to solve fluid-structure interaction of hyperelastic and anisotropic structures immersed in incompressible, laminar, transitional, or turbulent flow [Nestola et al., 2019]. The main characteristics of this method are the use of a variational transfer based on L^2-projections for coupling conditions, a high-order finite difference solver for Navier-Stokes equations, and the solid motion evaluated through the resolution of the elastodynamics equations.
Then, the fluid-structure interaction problem we consider read as follows:

Solid subproblem:

$$\rho_s \frac{\partial^2 \hat{\mathbf{u}}_s}{\partial t^2} - \hat{\nabla} \cdot \hat{\mathbf{P}} = \mathbf{0} \qquad \text{in } \hat{\Omega}_s \tag{4.66}$$

$$\hat{\mathbf{u}}_s = \hat{\mathbf{u}}_b \qquad \text{on } \hat{\Gamma}_s^D \tag{4.67}$$

Fluid subproblem:

$$\rho_f \frac{\partial \mathbf{v}_f}{\partial t} + \rho_f (\mathbf{v}_f \cdot \nabla \mathbf{v}_f) - \mu_f \Delta \cdot \mathbf{v}_f + \nabla p_f = \mathbf{f}_{fsi} \qquad \text{in } \Omega_f \tag{4.68}$$

$$\nabla \cdot \mathbf{v}_f = 0 \qquad \text{in } \Omega_f \tag{4.69}$$

$$\mathbf{v}_f = \mathbf{v}_b \qquad \text{on } \Gamma_f^D \tag{4.70}$$

Initial conditions:

$$\hat{\mathbf{u}}_s(\hat{\mathbf{x}}_s, 0) = \hat{\mathbf{u}}_s^0 \qquad \text{in } \hat{\Omega}_s \tag{4.71}$$

$$\frac{\partial \hat{\mathbf{u}}_s}{\partial t}(\hat{\mathbf{x}}_s, 0) = \frac{\partial \hat{\mathbf{u}}_s^0}{\partial t} \qquad \text{in } \hat{\Omega}_s \tag{4.72}$$

$$\mathbf{v}_f(\mathbf{x}, 0) = \mathbf{v}_f^0 \qquad \text{in } \Omega_f \tag{4.73}$$

FSI Coupling conditions:

$$\mathbf{v}_f = \frac{\partial \hat{\mathbf{u}}_s}{\partial t} \qquad \text{on } \Gamma^{fsi}(t) \tag{4.74}$$

$$\hat{J}^{-1} \hat{\mathbf{P}} \hat{\mathbf{F}}^T \mathbf{n} = \sigma_f \mathbf{n} \qquad \text{on } \Gamma^{fsi}(t) \tag{4.75}$$

where $\mathbf{f}_{fsi}$ represents the interaction term which considers the presence of the solid superimposing the stresses of the structure into the fluid stress.

4.5 Fluid-stricture interaction problem with active term

One fascinating and challenging area within FSI is the study of cardiac models, where the dynamic behavior of the heart is influenced by both fluid dynamics and the active contraction of cardiac muscle. However, to accurately capture the dynamic behavior of the heart, it is crucial to account for the active contraction and its impact on fluid flow patterns.In this section, we present a generalized approach to the Fluid-Structure Interaction (FSI) framework. We achieve this by incorporating an active term into the elastodynamic equations, enabling us to capture the dynamic behavior of the structure arising from active contraction.
There are typically two different ways in the literature for modeling an activation term in solid mechanics: the first one consists of decomposing the total stress into a passive mechanical part and an active part, and it is called $active\ stress$. The second one was inspired by the ideas in plasticity and theories of growth and decomposes the deformation gradient tensor into an active deformation tensor and an elastic deformation tensor. It is named $active\ strain$.
A comparison between the two different approaches has been efficiently proposed in Guan et al. [2022] and Rossi et al. [2012], as a matter of fact, both procedures have strong motivations: the active stress can easily fit into experiments, on the other hand, active strain is mathematically more robust.
In our proposed framework, we extend the elastodynamic equations by introducing an active stress term. Unlike previous approaches that relied on active strain, we utilize active stress as a more comprehensive measure of the force generated by the active contraction of the structure. By incorporating active stress into the elastodynamic equations, we aim to provide a more accurate representation of the dynamic behavior.
Firstly, we consider a uniform time-dependent active stress that allows us to investigate the overall impact of active contraction on fluid-structure interactions. This approach provides a straightforward and computationally efficient method to assess the general behavior of the system.
We further enhance the framework by incorporating activation maps obtained through the resolution of electrophysiological models.

4.5.1 Active stress

The active stress method decomposed the Cauchy stress tensor into a mechanical part and an active part, and both can induce deformations.

$$\hat{\boldsymbol{\sigma}} = \hat{\boldsymbol{\sigma}}_m + \hat{\boldsymbol{\sigma}}_a \tag{4.76}$$

If we consider an active stress exerted only along the fibres direction, the first Piola-Kirchoff tensor associated with $\hat{\boldsymbol{\sigma}}_a$ is

$$\hat{\mathbf{P}}_a = T_a \hat{\mathbf{F}}(\mathbf{f} \otimes \mathbf{f}) \tag{4.77}$$

where the scalar value T_a represents the active component along the fiber direction $\mathbf{f}$. The total Piola stress tensor can be rewritten as

$$\hat{\mathbf{P}}_t = \hat{\mathbf{P}}_m + \hat{\mathbf{P}}_a \tag{4.78}$$

Citing Ambrosi and Pezzuto [2012], it is possible to reinterpret in terms of active strain for polynomial energy. Consider, for example, a basic constitutive equation for the active strain $\hat{\mathbf{F}}_a$ that describes the contraction of the fibers

$$\hat{\mathbf{F}}_a = \mathbf{I} - \gamma \mathbf{f} \otimes \mathbf{f} \tag{4.79}$$

and let us suppose that the strain energy is the sum of a neo-Hookean isotropic term and a transverse isotropic one

$$\mathscr{W} = \frac{\mu_1}{2} \hat{\mathbf{F}}_e : \hat{\mathbf{F}}_e + \frac{\mu_2}{2} \hat{\mathbf{F}}_e \mathbf{f} \cdot \hat{\mathbf{F}}_e \mathbf{f} \tag{4.80}$$

The Cauchy stress is

$$\hat{\sigma} = \det\big(\hat{\mathbf{F}}_a\big) \frac{\partial \mathscr{W}}{\partial \hat{\mathbf{F}}_e} \hat{\mathbf{F}}_a^{-T} \hat{\mathbf{F}} = \det\big(\hat{\mathbf{F}}_a\big) \big(\mu_1 \hat{\mathbf{F}}_e + \mu_2 \hat{\mathbf{F}}_e \mathbf{f} \otimes \mathbf{f}\big) \hat{\mathbf{F}}_a^{-T} \hat{\mathbf{F}}^T \tag{4.81}$$

and noting that $\hat{\mathbf{F}}_e \mathbf{f} = \hat{\mathbf{F}} \hat{\mathbf{F}}_a^{-1} \mathbf{f}$ we obtain :

$$\hat{\sigma} = \mu_1 \left(\hat{\mathbf{F}} \hat{\mathbf{F}}^T - \gamma \hat{\mathbf{F}} \hat{\mathbf{F}}^T + \gamma \frac{2-\gamma}{1-\gamma} \hat{\mathbf{F}} \mathbf{f} \otimes \hat{\mathbf{F}} \mathbf{f} \right) + \mu_2 \left(1 + \frac{\gamma}{1-\gamma} \right) \hat{\mathbf{F}} \mathbf{f} \otimes \hat{\mathbf{F}} \mathbf{f} \tag{4.82}$$

where all the terms depending on γ can be seen as the active dynamics contribution.
Thus we can reformulate the fluid-structure interaction problem by adopting the active stress model on the elastodynamics equations of the solid subproblem for simulating active contractions:

Solid subproblem:

$$\rho_s \frac{\partial^2 \hat{\mathbf{u}}_s}{\partial t^2} - \hat{\nabla} \cdot \hat{\mathbf{P}}_t = \mathbf{0} \qquad \text{in } \hat{\Omega}_s \tag{4.83}$$

$$\hat{\mathbf{u}}_s = \hat{\mathbf{u}}_b \qquad \text{on } \hat{\Gamma}_s^D \tag{4.84}$$

Fluid subproblem:

$$\rho_f \frac{\partial \mathbf{v}_f}{\partial t} + \rho_f(\mathbf{v}_f \cdot \nabla \mathbf{v}_f) - \mu_f \Delta \cdot \mathbf{v}_f + \nabla p_f = \mathbf{f}_{fsi} \qquad \text{in } \Omega_f \tag{4.85}$$

$$\nabla \cdot \mathbf{v}_f = 0 \qquad \text{in } \Omega_f \tag{4.86}$$

$$\mathbf{v}_f = \mathbf{v}_b \qquad \text{on } \Gamma_f^D \tag{4.87}$$

Initial conditions:

$$\hat{\mathbf{u}}_s(\hat{\mathbf{x}}_s, 0) = \hat{\mathbf{u}}_s^0 \qquad \text{in } \hat{\Omega}_s \tag{4.88}$$

$$\frac{\partial \hat{\mathbf{u}}_s}{\partial t}(\hat{\mathbf{x}}_s, 0) = \frac{\partial \hat{\mathbf{u}}_s^0}{\partial t} \qquad \text{in } \hat{\Omega}_s \tag{4.89}$$

$$\mathbf{v}_f(\mathbf{x}, 0) = \mathbf{v}_f^0 \qquad \text{in } \Omega_f \tag{4.90}$$

FSI Coupling conditions:

$$\mathbf{v}_f = \frac{\partial \hat{\mathbf{u}}_s}{\partial t} \qquad \text{on } \Gamma^{fsi}(t) \tag{4.91}$$

$$\hat{J}^{-1} \hat{\mathbf{P}}_t \hat{\mathbf{F}}^T \mathbf{n} = \boldsymbol{\sigma}_f \mathbf{n} \qquad \text{on } \Gamma^{fsi}(t) \tag{4.92}$$

where $\mathbf{f}_{fsi}$ represents the interaction term which considers the presence of the solid superimposing the stresses of the structure into the fluid stress and $\hat{\mathbf{P}}_t = \hat{\mathbf{P}}_m + \hat{\mathbf{P}}_a$ is the sum of mechanical stress and active stress tensors.
In this work, the electromechanical coupling is not considered. However, the active stress term is characterized by a time-dependent activation function $\alpha(t)$ and takes into account the orientation of the fibres.

$$\hat{\mathbf{P}}_a = \alpha(t)\mathbf{F}\mathbf{g}\mathbf{n} \otimes \mathbf{n} \tag{4.93}$$

We first consider a linear time-dependent activation function. Then, to establish a first unidirectional link between the FSI framework and electrophysiology, we propose to use the activation time Ψ_a evaluated by electrophysiological models (such as the reduced eikonal model) in the activation function.

Chapter 5

Discretization of the Generalized Fluid-Structure Interaction Problem

5.1 Space discretization

The main idea of Immersed boundary method is to embed the solid structure into the fluid domain and modify the fluid dynamics subproblem by adding s source force term which accounts for the reaction force exerted from the solid to the fluid. One of the advances proposed by this method is the use of a fixed cartesian mesh for the fluid and an independent mesh for the immersed structure. The method proposed by Peskin was based on finite difference for the spatial discretization but other recent approaches have included a finite element spatial discretization for the Lagrangian subproblem related to the solid [Boffi and Gastaldi, 2003], [Griffith and Luo, 2017a], [Glowinski and Kuznetsov, 2007].
Following the methodology proposed by Nestola et al. [2019], we adopt the finite element method for the spatial discretization of the elastodynamics equations and the finite difference method for the spatial discretization of Navier-Stokes equations.
This approach, inspired by the immersed boundary method, embeds the solid structure in the computational domain Ω and the fluid subproblem is solved in Ω, including the part in the interior of the immersed structure, where an additional force term in Navier-Stokes equations guarantees the balance of the stresses on the interface $\Gamma^{fsi}(t)$.

Solid subproblem

Let us consider $\hat{\Omega}_s^h$ as the discrete domain of the solid domain $\hat{\Omega}_s$ and $\hat{T}_s^h = \{\hat{E}_s \subseteq \hat{\Omega}_s^h | \bigcup \hat{E}_s = \hat{\Omega}_s^h\}$ the associated triangulation such that $\hat{E}_s^1, \hat{E}_s^2 \subseteq \hat{T}_s^h$ with $\hat{E}_s^1 \neq \hat{E}_s^2$ then $\hat{E}_s^1 \cap \hat{E}_s^2 = \emptyset$.
If we take into account first-order finite elements, the function space read as

$$\hat{X}_s^h(\hat{T}_s^h) = \{\hat{\psi}_s^h \in C^0(\hat{\Omega}_s^h), \hat{\psi}_{s|\hat{E}_s}^h \in \mathbb{P}_1 \forall \hat{E}_s \in \hat{T}_s^h\}$$

where $\mathbb{P}_1$ is the space of linear polynomials defined on each element $\hat{E}_s \in \hat{T}_s^h$.
Let $\hat{\psi}_s^h$ be the test functions of the function space $\hat{V}_s^h = H^1_{\hat{\Gamma}_D}(\hat{\Omega}_s) \cap \hat{X}_s^h$. Thus, the Galerkin formulation of the elastodynamics equations read as:

$$\int_{\hat{\Omega}_s} \rho_s \frac{\partial^2 \hat{\mathbf{u}}_s^h}{\partial t^2} \cdot \hat{\psi}_s^h dV_{\hat{\mathbf{x}}} - \int_{\hat{\Omega}_s} \hat{\nabla} \cdot \hat{\mathbf{P}}_t(\hat{\mathbf{u}}_s^h) \cdot \hat{\psi} dv_{\hat{\mathbf{x}}} = \mathbf{0} \quad \forall \hat{\psi}_s^h \in \hat{V}_s^h \tag{5.1}$$

where $\hat{\mathbf{P}}_t = \hat{\mathbf{P}}_m + \hat{\mathbf{P}}_a$
Applying the Green-s formula we obtain

$$\int_{\hat{\Omega}_s} \rho_s \frac{\partial^2 \hat{\mathbf{u}}_s^h}{\partial t^2} \cdot \hat{\psi}_s^h dV_{\hat{\mathbf{x}}} + \int_{\hat{\Omega}_s} \hat{\mathbf{P}}_t(\hat{\mathbf{u}}_s^h) : \hat{\nabla} \hat{\psi} dv_{\hat{\mathbf{x}}} = \int_{\hat{\Gamma}^{fsi}} \hat{\mathbf{P}}_t(\hat{\mathbf{u}}_s^h) \hat{\mathbf{n}} \cdot \hat{\psi} dv_{\hat{\mathbf{x}}} \quad \forall \hat{\psi}_s^h \in \hat{V}_s^h \tag{5.2}$$

The term $\hat{\mathbf{P}}_t(\hat{\mathbf{u}}_s^h)\hat{\mathbf{n}}$ can be decoded as the force exerted on the solid on the interface and plays the role of Lagrange multiplier associated to the constraint related to the continuity of the velocity.
We define

$$(\hat{\varphi}, \cdot)_{L^2(\hat{\Omega}_s)} = \int_{\hat{\Omega}_s} \hat{\varphi} \cdot \hat{\psi} dV_{\hat{\mathbf{x}}}$$

$$(\hat{\varphi}, \cdot)_{L^2(\hat{\Gamma}^{fsi})} = \int_{\hat{\Gamma}^{fsi}} \hat{\varphi} \cdot \hat{\psi} dV_{\hat{\mathbf{x}}}$$

the L^2 inner product operators and

$$(\hat{\mathbf{f}}_{s \to f}, \cdot)_{L^2(\hat{\Omega}_s)} = (\hat{\mathbf{P}}_t(\hat{\mathbf{u}}_s^h \hat{\mathbf{n}}, \cdot)_{L^2(\hat{\Gamma}^{fsi})}$$

the term representing the force exerted from the solid to the fluid.
Then, the Galerkin formulation can be rewritten as

$$(\hat{\mathbf{f}}_{s \to f}, \cdot)_{L^2(\hat{\Omega}_s)} = \left(\rho_s \frac{\partial^2 \hat{\mathbf{u}}_s^h}{\partial t^2} + \hat{\mathbf{f}}_{int}, \cdot \right)_{L^2(\hat{\Omega}_s)} \tag{5.3}$$

where

$$\left(\rho_s \frac{\partial^2 \hat{\mathbf{u}}_s^h}{\partial t^2}, \cdot\right)_{L^2(\hat{\Omega}_s)} = \int_{\hat{\Omega}_s} \rho_s \frac{\partial^2 \hat{\mathbf{u}}_s^h}{\partial t^2} \cdot \hat{\psi}_s^h dV_{\hat{\mathbf{x}}} \tag{5.4}$$

$$\left(\hat{\mathbf{f}}_{int}, \cdot\right)_{L^2(\hat{\Omega}_s)} = \int_{\hat{\Omega}_s} \hat{\mathbf{P}}_t(\hat{\mathbf{u}}_s^h) : \hat{\nabla}\hat{\psi} dv_{\hat{\mathbf{x}}} \tag{5.5}$$

Then it is possible to evaluate the coupling force term $\hat{\mathbf{f}}_{s\to f}$ as the residual of the variational equality (5.3).
Let $\{\hat{\phi}_{s,i}^h\}_{i\in I_s}$ be the Langrangian basis of $\hat{V}_s^h$ where I_s is a set of index. We can write the matrix formulation of (5.2)

$$\rho_s \mathbf{m} \frac{\partial^2 \hat{\mathbf{u}}_s}{\partial t^2} + \mathbf{k}(\hat{\mathbf{u}}_s) = \mathbf{m}\hat{\mathbf{f}}_{s\to f} \tag{5.6}$$

where $\mathbf{m}$ is the mass matrix

$$m_{ij} = \int_{\hat{\Omega}_s} \mathbf{p}\hat{\mathbf{h}}\mathbf{i}_{s,j} \cdot \hat{\phi}_{s,i} dV_{\hat{\mathbf{x}}}$$

$\mathbf{k}$ represents the vector of nonlinear mechanical and active forces

$$k_i = \int_{\hat{\Omega}_s} \hat{\mathbf{P}}_t(\hat{\mathbf{u}}_s^h) : \hat{\nabla}\hat{\phi}_{s,i} dV_{\hat{\mathbf{x}}}$$

$\hat{\mathbf{u}}_s$ is the vector of the displacement field and $\hat{\mathbf{f}}_{s\to f}$ is the vectorial function representing the fluid-structure interaction force density.

fluid subproblem

The Navier-Stokes equations defined in the fluid-structure interaction problem in a domain $\Omega_f(t)$ are solved in Ω, including the region in the interior of the immersed structure and adding the interaction force term $\mathbf{f}_{f\to s}$ with the intention of superimposing the stresses of the structure into the fluid stresses.
The Navier-Stokes equations can be rewritten using matrix operators

$$\rho_f \frac{\partial}{\partial t}\begin{bmatrix}\mathbf{v}_f \\ \mathbf{0}\end{bmatrix} + \begin{bmatrix}-\mathscr{L} & \mathscr{G} \\ \mathscr{D} & 0\end{bmatrix}\begin{bmatrix}\mathbf{v}_f \\ p_f\end{bmatrix} = \begin{bmatrix}\mathscr{N}(\mathbf{v}_f) + \mathbf{f}_{f\to s} \\ \mathbf{0}\end{bmatrix} \tag{5.7}$$

where $\mathscr{L}$ is the Laplacin operator and $\mathscr{G}, \mathscr{D}$ are the gradient and divergence operators respectively. $\mathscr{N}$ represents all the other terms except for the time derivative.

For space discretization, we follow the approach proposed by Henniger et al. [2010] and introduce a rectangular domain on a Cartesian grid.
We apply finite differences on a staggered grid for the velocity and the pressure.

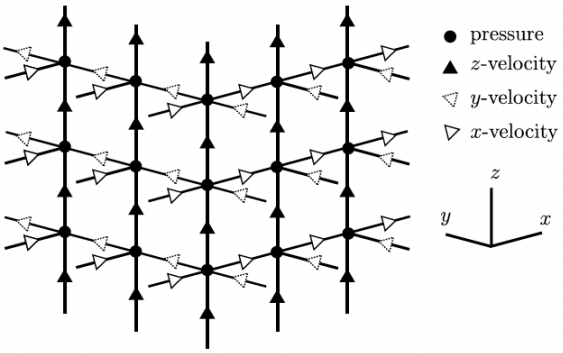

Figure 5.1. Staggered grid in three dimensions [Nestola et al., 2019].

We consider four subgrids: one for each velocity component, labeled $1, 2$ and 3 (corresponding to the direction of the velocity component) and one for the pressure labeled 0.
We also eliminate the zero diagonal block in (5.7) and derive a Poisson problem for the pressure by evaluating the Schur complement, which is solved with the iterative Krylov subspace method BiCGstab with right preconditioning by a V-cycle geometric multigrid preconditioner of Gauss-Seidel type. For a detailed description the reader may refer to Henniger et al. [2010].
Hence the momentum equations are solved on the velocity grid, while the continuity equation is satisfied on the pressure grid. The discrete divergence operator **D** performs first derivatives on the grid 0 from values from the grid $1, 2$ and 3. On the other hand, the discrete gradient operator **G** performs first derivatives on the grid $1, 2$ and 3 from values on the grid 0. The discrete Laplace operator **L** performs operations on one grid only.
The discrete form of the operator $\mathcal{N}$ demands products between velocity components and the first derivatives of the other velocity components. The discrete operator **C** represents the first derivative on the i-th grid in the j direction

$$c_{ij} = \frac{\partial (\cdot)_i}{\partial x_j}.$$

A central stencil width n has been chosen for all operators. In the interior of the domain, because of **L** and **C** have the variable and its derivative defined on the

same grid, the convergence order is $n-1$ (and becomes $n-2$ in the presence of upwind-biased schemes). For all the other operators **D**, **G**, which transfer information between different grids, the convergence orders are identical to the stencil widths.

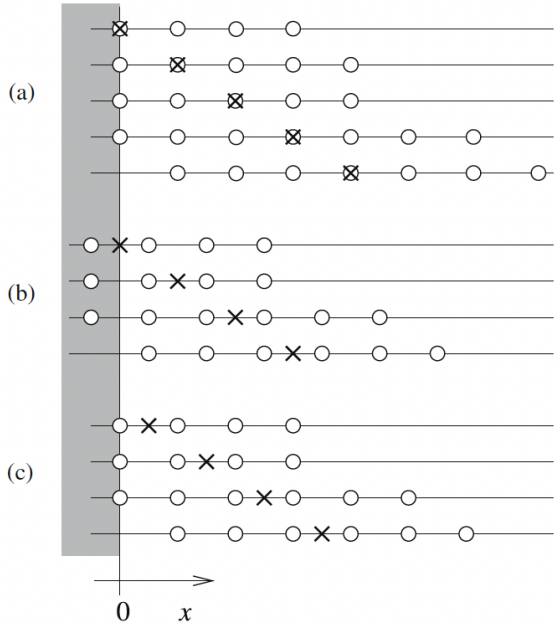

Figure 5.2. An example of a differentiation scheme near the boundary: (a) from a velocity grid to the same velocity grid, (b) from a velocity grid to the pressure grid, and (c) from the pressure grid to a velocity grid [Nestola et al., 2019].

5.2 Fluid-structure coupling based on variational transfer

The coupling between the solid and fluid subproblems necessitates to transfer the velocities $\mathbf{v}_f$ from the Eulerian fluid grid to the Lagrangian solid mesh and the force densities $\mathbf{f}_{s\to f}$ from the Lagrangian solid mesh to the Eulerian fluid grid. In the immersed boundary method the force exerted on the fluid and the fluid velocity can be expressed involving a smoothed approximation of the Dirac delta function even though a consistent approximation of the Dirac delta function is difficult to find and it suffers from poor volume conservation.
More recently transfer operators based on variational approaches, such as L^2-projections or pseudo-L^2-projections, have been developed. This dissertation considers a framework inspired by the immersed boundary method with the use of exact L^2-projections approach for coupling conditions [Nestola et al., 2019].

5.2.1 L^2-projection approach

We start with a short introduction of the mortar projection, which will be the base for the formulation of L^2-projection approach.
Let $\Omega_m, \Omega_s \subset \mathbb{R}^d$, with $d = 2, 3$ and $I = \Omega_m \cap \Omega_s$ the intersection of the two domains.
The domains Ω_m and Ω_s can be approximated by the discrete domains Ω_m^h and Ω_s^h with the associated mesh $\mathcal{T}_k^h = \{E_k \subseteq \Omega_k^h | \bigcup E_k = \Omega_s^h\}$ and $k = m, s$, where its elements E_k form a partition such that if $E_k^1, E_k^1 \subset \Omega_k$ and $E_k^1 \neq E_k^2$ then $E_k^1 \cap E_k^2 = \emptyset$.
Lastly, let us denote by $V_h = V_h(\mathcal{T}_m^h)$ and $W_h = W_h(\mathcal{T}_s^h)$ the associated finite element spaces, $I_h = \Omega_m^h \cap \Omega_s^h$ the intersection of the two discretized domains and N_m, N_s the set of nodes of the meshes.
For simplicity, we assume $\Omega_s^h \subseteq \Omega_m^h$ and define $M_h = M_h(\mathcal{T}_s^h)$ which is a suitable discrete space of Lagrange multipliers based on the same mesh as W_h (the association with $\mathcal{T}_{\Updownarrow}^{\langle}$ or $\mathcal{T}_s^h$ is arbitrary).
The space W_h is often referred to as slave while V_h as master. The main idea of mortar projection is to map a function from to the master discrete space V_h to the slave discrete space W_h through a projection operator $P : V_h \to W_h$ which for a function $v_h \in V_h$ finds $w_h = P(v_h) \in W_h$ such that

$$(P(v_h), \mu_h)_{L^2(I_h)} = (v_h, \mu_h)_{L^2(I_h)} \quad \forall \mu_h \in M_h \tag{5.8}$$

where $(\cdot,\cdot)_{L^2(I_h)}$ is the L^2-inner product.
Let $\{\phi_i\}_{i\in J_v}$, $\{\varphi_j\}_{j\in J_w}$ and $\{\psi_k\}_{k\in J_\mu}$ be the basis of V_h, W_h and M_h repsectively and

J_v, J_w, J_μ sets of indices. We can write (5.8) as a matrix equation

$$\mathbf{Bv} = \mathbf{Dw} \tag{5.9}$$

with

$$b_{k,i} = \int_{I_h} \phi_i \psi_k dV$$
$$d_{k,j} = \int_{I_h} \varphi_j \psi_k dV$$

Assuming the invertibility of **D** it is possible to define the algebraic representation of the discrete mortar projection operator **T**

$$\mathbf{w} = \mathbf{D}^{-1}\mathbf{Bv} = \mathbf{Tv} \tag{5.10}$$

Depending on the choice of M_h we can obtain different transfer operators.
If we set $M_h = W_h$, the projection operator **T** becomes the discrete representation of L^2-projection.
Since the evaluation of the inverse of the matrix **D** might be computationally expensive, we can apply the transfer operator solving each time the linear system, keeping the matrices **D** and **B** separated.

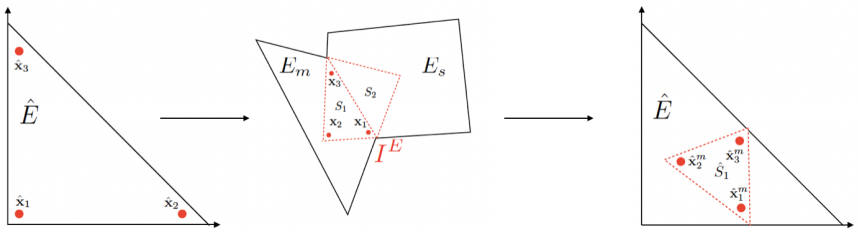

Figure 5.3. Quadrature points mapped to the simplex S_1 and transformed to the reference element [Krause and Zulian, 2016].

Following Krause and Zulian [2016] we give an example procedure for the assembly of the coupling operator **T**.

- First we need to determine all pairs of intersecting elements by means of tree-search algorithm and data structures.

- For each pair of intersecting elements we compute the intersection generated polytope $I^E = E_m \cap E_s$ and we define a triangulation $\mathscr{T}^{\langle}_{\mathscr{GE}} = \{S_i \subseteq I^E | \bigcup S_i = I^E\}$, where S_i is a simplex.

- We generate the quadrature points by mapping points from quadrature rules defined on a reference element $\hat{E}$ to each simplex S_i and choosing a suitable quadrature formula with K points $\{\hat{x}_k\}_{k=1}^K \subset \hat{E}$ and weights $\{\alpha_k\}_{k=1}^K$ such that $\sum_{k=1}^K \alpha_k = 1$.

- We transform the quadrature points in S_i to the reference element $\hat{E}$ for both master and slave mesh. Then we compute the local element-wise contributions by means of numerical quadrature and finally assemble **B** and **D**

5.2.2 Spatial discretization of fluid-structure coupling

In order to use the L^2-approach for the coupling space discretization we need to attach Lagrangian basis functions to the finite difference grid of the fluid subproblem and to introduce the corresponding auxiliary finite-element space $V_f^h = V_f^h(\mathscr{T}_f^h) \subset H^1_{\Gamma_f^D}(\Omega)$, where $\mathscr{T}_f^h$ is the fluid grid.
Let M_{fsi}^h a discrete space of Lagrange multipliers based on the current configuration of the slave mesh $\mathscr{T}^{\langle}_{\int}$, coinciding with the current configuration of the solid mesh.
We define the fluid-structure interaction operator $\Pi : V_f^h(\mathscr{T}_f^h) \to V_s^h(\mathscr{T}^{\langle}_{\int}(\sqcup))$ for transferring the discrete velocity field from the fluid grid to the current configuration of the solid mesh, then for each component of the fluid velocity $v_f^h \in V_f^h$ we want to find $w_s^h \in V_s^h$ such that

$$\int_{I_h} (v_f^h - \Pi(v_f^h))\lambda_{fsi}^h dV = \int_{I_h} (v_f^h - w_s^h)\lambda_{fsi}^h dV = 0 \quad \forall \lambda_{fsi}^h \in M_{fsi}^h \tag{5.11}$$

with $I_h = \mathscr{T}_s^h(t) \cap \mathscr{T}_f^h$ the overlapping region between solid mesh and fluid grid and w_s^h the solid velocity field in the current configuration $w_s^h = \hat{w}_s^h \circ \chi(\hat{\mathbf{x}}_s, t)$.
Let $\{\varphi_{s,i}^h\}_{i\in J_s}$, $\{\varphi_{f,j}^h\}_{j\in J_f}$ and $\{\varphi_{fsi,k}^h\}_{k\in J_{fsi}}$ be the Lagrangian basis functions of V_s^h, V_f^h and M_{fsi}^h repsectively and J_s, J_f, J_{fsi} sets of indices. We can write the mortar matrix in (5.9)

$$\mathbf{B}\mathbf{v}_f = \mathbf{D}\mathbf{w}_s \tag{5.12}$$

with

$$b_{k,j} = \int_{I_h} \varphi^h_{f,j} \cdot \varphi^h_{fsi,k} dV$$
$$d_{k,i} = \int_{I_h} \varphi^h_{s,i} \cdot \varphi^h_{fsi,k} dV$$

and $\mathbf{w}_s, \mathbf{v}_f$ are the vectors of coefficients entries $w^h_{s,i}$ and $v^h_{f,j}$.
The discrete mortar projection operator reads as

$$\mathbf{w}_s = \mathbf{D}^{-1}\mathbf{B}\mathbf{v}_f \tag{5.13}$$

but for reducing computational costs, we solve the linear system at each time getting the projected velocity $\mathbf{w}_s$. Then we use only the values related to the interface $\Gamma^{fsi}(t)$ for imposing the velocity constraint

$$\mathbf{v}_{s,\Gamma^{fsi}(t)} = \mathbf{w}_{s|\Gamma^{fsi}(t)} \tag{5.14}$$

where $\mathbf{v}_{s,\Gamma^{fsi}(t)}$ is the velocity of the structure at the interface and we use it as boundary condition for the solid problem.
Then we need to transfer the fluid-structure interaction force density term from the solid mesh to the fluid grid, so the adjoint operator $\tilde{\mathbf{T}} = \mathbf{T}^T$ is adopted

$$\mathbf{f}_{f\to s} = \tilde{\mathbf{T}}\mathbf{f}_{s\to f} \tag{5.15}$$

where $\mathbf{f}_{s\to f}$ is the force density evaluated in the current configuration $\Omega_s(t)$ and $\mathbf{f}_{f\to s}$ is the source term added to the right-hand side of the Navier-Stokes equations.

5.3 Time discretization

In this section, we describe the time discretization of the entire fluid-structure interaction system.
For solving a fluid-structure interaction problem there can be used two different approaches.
The first one, known as loosely coupling, is based on the solution of the fluid and structure subproblems only once at each time step, while the second one, known as strongly coupling, performs the fluid and structure subproblem at every time step until synchronization is obtained between the solutions.

Loosely coupled schemes are less expensive in terms of computational costs but they require rigid restrictions for maintaining stability. It has been proved they feature instabilities under certain choices of the physical parameters, in particular when the fluid and structure densities are comparable, as in hemodynamics [Causin et al., 2005]. However, recent works have been focused on loosely coupled schemes based on Robin interface conditions with the introduction of suitable parameters that influence the stability of the numerical solution [Gigante and Vergara, 2021].
A strongly coupled scheme, with a fully implicit treatment of the FSI system, is a better choice for overcoming these limitations.
We start from the time discretization of the solid subproblem, where we adopt the Newmark scheme. Then we consider the discretization in time of the fluid subproblem following the strategy proposed by Henniger et al. [2010], where a third-order Runge-Kutta scheme is used. Lastly, we present the fluid-structure algorithm used for improving the solution of the fluid-structure interaction system.

Solid suproblem

We recall the elastodynamics equations obtained by the finite element spatial discretization

$$\rho_s \mathbf{m} \frac{\partial^2 \hat{\mathbf{u}}_s}{\partial t^2} + \mathbf{k}(\hat{\mathbf{u}}_s) = \mathbf{m}\hat{\mathbf{f}}_{s\to f} \tag{5.16}$$

where $\hat{\mathbf{u}}_s$ is the vector of the displacement field, $\hat{\mathbf{f}}_{s\to f}$ is the vectorial function representing the fluid-structure interaction force density, $\mathbf{m}$ is the mass matrix and $\mathbf{k}(\hat{\mathbf{u}}_s)$ describes the mechanic and active forces:

$$m_{ij} = \int_{\hat{\Omega}_s} \hat{\phi}^h_{s,j} \cdot \hat{\phi}^h_{s,i} dV_{\hat{\mathbf{x}}} \tag{5.17}$$

$$k_i = \int_{\hat{\Omega}_s} \hat{\mathbf{P}}_t(\hat{\mathbf{u}}_s) : \hat{\nabla}\hat{\phi}^h_{s,i} dV_{\hat{\mathbf{x}}} \tag{5.18}$$

with $\hat{\mathbf{P}}_t = \hat{\mathbf{P}}_m + \hat{\mathbf{P}}_a$ and $\{\hat{\phi}^h_{s,i}\}_{i\in I_s}$ Lagrangian basis of $\hat{V}^h_s = H^1_{\hat{\Gamma}^D_s}(\hat{\Omega}_s) \cap \hat{X}^h_s$.
Let's consider a time interval $[0T]$ divided into N equal subintervals of length Δt. Set $t^n = n\Delta t$ and denote $\hat{\mathbf{u}}^n_s$ the approximation of $\hat{\mathbf{u}}_s$ at time t^n.
We adopt the Newmark scheme, which is one of the most used approaches for structural dynamics:

$$\rho_s \mathbf{m} \frac{\hat{\mathbf{u}}^{n+1}_s}{\Delta t^2} + \mathbf{k}(\hat{\mathbf{u}}^{n+1}_s) = \mathbf{m}\hat{\mathbf{f}}^{n+1}_{s\to f} + \mathbf{r}_s(\hat{\mathbf{u}}^n_s) \tag{5.19}$$

with

$$\mathbf{r}_s(\hat{\mathbf{u}}_s^n) = \rho_s \mathbf{m}\left(\frac{2\hat{\mathbf{u}}_s^n}{\Delta t^2} - \frac{\hat{\mathbf{u}}_s^{n-1}}{\Delta t^2}\right) \tag{5.20}$$

Fluid subproblem

It is possible to write Navier-Stokes equations in matrix operator form

$$\rho_f \frac{\partial}{\partial t}\begin{bmatrix}\mathbf{v}_f \\ \mathbf{0}\end{bmatrix} + \begin{bmatrix}-\mathscr{L} & \mathscr{G} \\ \mathscr{D} & 0\end{bmatrix}\begin{bmatrix}\mathbf{v}_f \\ p_f\end{bmatrix} = \begin{bmatrix}\mathscr{N}(\mathbf{v}_f) + \mathbf{f}_{f\to s} \\ \mathbf{0}\end{bmatrix} \tag{5.21}$$

where $\mathscr{L}$, $\mathscr{G}$ and $\mathscr{D}$ are the Laplace, gradient and divergence operators respectively. $\mathscr{N}$ contains all the remaining terms except for the time derivative. The presence of the structure is taken into account by the interaction force term $\mathbf{f}_{f\to s}$ where the stresses of the structure are imposed into the fluid stresses which also included internal forces of the fluid.
We use explicit finite difference for the spatial discretization, leading to a linear system of equations

$$\rho_f \frac{\partial}{\partial t}\begin{bmatrix}\mathbf{v}_f \\ \mathbf{0}\end{bmatrix} + \begin{bmatrix}-\mathbf{L} & \mathbf{G} \\ \mathbf{D} & 0\end{bmatrix}\begin{bmatrix}\mathbf{v}_f \\ p_f\end{bmatrix} = \begin{bmatrix}\mathbf{N}(\mathbf{v}_f) + \mathbf{f}_{f\to s} \\ \mathbf{0}\end{bmatrix} \tag{5.22}$$

where **L**, **G** and **D** represent the Laplace, gradient and divergence discrete operators.
We apply an explicit time integration with a low-storage third-order accurate Runga-Kutta scheme [Wray, 1986]. The equation related to the conservation of mass is independent of time and must be satisfied at each time step, then an implicit treatment is required. The same consideration can be made for the pressure gradient.
Let $\mathbf{v}_f^{m=0} = \mathbf{v}_f^n$ and $\mathbf{v}_f^{m=3} = \mathbf{v}_f^{n+1}$. Then we obtain the following algebraic system

$$\begin{bmatrix}\mathbf{J} & \mathbf{G}^m \\ \mathbf{D} & 0\end{bmatrix}\begin{bmatrix}\mathbf{v}_f^m \\ p_f^m\end{bmatrix} = \begin{bmatrix}\mathbf{q}(\mathbf{v}_f^{m-1}, \mathbf{v}_f^{m-2}, \mathbf{f}_{f\to s}^{n+1}) \\ \mathbf{0}\end{bmatrix} \tag{5.23}$$

with **J** equal to the identity matrix **I** except that the rows correspond to the boundary points, which contain velocity boundary conditions. The discretized diffusive and convective terms are contained in **q** together with the interaction force $\mathbf{f}_{f\to s}$ which is reevaluated for each Runge-Kutta subtime step.

Fluid-structure interaction coupling

A fully implicit treatment is used for the nonlinear FSI system, which can be written employing an algebraic formulation as follow

$$\mathbf{S}(\hat{\mathbf{u}}_s^{n+1}) = \mathbf{m}\hat{\mathbf{f}}_{s\to f}^{n+1} + \mathbf{r}_s(\hat{\mathbf{u}}_s^n) \tag{5.24}$$

$$\mathbf{v}_{s,\Gamma^{fsi}(t)}^{n+1} - (\mathbf{T}\mathbf{v}_f^{n+1})_{|\Gamma^{fsi}(t)} = 0 \tag{5.25}$$

$$\mathbf{F}(\mathbf{v}^{n+1,p_f^{n+1}}) = \mathbf{r}_s(\mathbf{f}_{f]\to s}^{n+1}, \mathbf{v}_f^n) \tag{5.26}$$

$$\mathbf{f}_{f\to s} - \tilde{\mathbf{T}}\mathbf{f}_{s\to f}^{n+1} = 0 \tag{5.27}$$

A strategy for solving the system is the iteration of the Block-Gauss-Seidel method between the fluid and the solid subproblems. Then we can start by writing it as a fixed point problem. For each time step we need to solve:

$$\hat{\mathbf{u}}_s = \mathscr{S}(\hat{\mathbf{u}}_s, \mathbf{v}_f) \tag{5.28}$$

$$(\mathbf{v}_f, p_f) = \mathscr{F}((\mathbf{v}_f, p_f), \hat{\mathbf{u}}_s) \tag{5.29}$$

where the operator $\mathscr{S}$ represents the first two equations of the FSI system related to the solid subproblem, while $\mathscr{F}$ takes the place of the remaining equations describing the fluid subproblem. The time step indices are omitted for facilitating the notation.
We initialize the variables at the previous time step, whose values are given $\hat{\mathbf{u}}_s^0 = \hat{\mathbf{u}}_s^n$, $\mathbf{v}_f^0 = \mathbf{v}_f^n$ and $p_f^0 = p_f^n$ and for $l \geq 0$

$$\hat{\mathbf{u}}_s^{l+1} = \mathscr{S}(\hat{\mathbf{u}}_s^l, \mathbf{v}_f^{l+1}) \tag{5.30}$$

$$(\mathbf{v}_f^{l+1}, p_f^{l+1}) = \mathscr{F}((\mathbf{v}_f^l, p_f^l), \hat{\mathbf{u}}_s^{l+1}) \tag{5.31}$$

The iterative procedure terminates when one of the following criteria is satisfied and the solid displacement and fluid velocity variables are updated:

Relative convergence criterion

$$\frac{\| \mathbf{f}_{s\to f}^{l+1} - \mathbf{f}_{s\to f}^{l} \|_\infty}{\| \mathbf{f}_{s\to f}^{0} \|} < \epsilon_R \tag{5.32}$$

Absolute convergence criterion

$$\| \mathbf{f}_{s\to f}^{l+1} - \mathbf{f}_{s\to f}^{l} \|_\infty < \epsilon_A \tag{5.33}$$

A scheme of the iterative algorithm is now proposed:

Algorithm 1 Algorithm

Step 0:
The displacement, velocity, and pressure variables are initialized.

$$\hat{\mathbf{u}}_s^0 = \hat{\mathbf{u}}_s^n \quad \mathbf{v}_f^0 = \mathbf{v}_\mathbf{f}^\mathbf{n} \quad p_f^0 = p_f^n$$

Step 1:
The fluid velocity is transferred from the cartesian fluid grid to the current configuration of the solid mesh.

$$\mathbf{w}_s^{l+1} = \mathbf{T}\mathbf{v}_f^l$$
where $\mathbf{w}_s$ is the spatial velocity of the solid in the current configuration.

Step 2:
The displacement field of the solid structure is computed on the interface. Γ^{fsi}

$$\hat{\mathbf{u}}^{l+1}_{s,\Gamma^{\hat{f}si}} = \hat{\mathbf{u}}^{n}_{s,\Gamma^{\hat{f}si}} + \Delta t \hat{\mathbf{w}}^{l+1}_{s|\Gamma^{\hat{f}si}}$$
where $\hat{\mathbf{w}}_s$ is the material velocity of the solid in the reference configuration $\hat{\mathbf{u}}_s = \mathbf{w}_s \circ \hat{\chi}^{-1}(\hat{\mathbf{x}}_s, t)$.

Step 3:
The discrete elastodynamics equations are solved by applying the Newmark scheme and imposing $\hat{\mathbf{u}}^{l+1}_{s,\Gamma^{\hat{f}si}}$ as Dirichlet boundary condition.

Step 4:
The reaction force $\mathbf{f}^{l+1}_{s\to s}$ is computed and transferred from the current configuration of the solid mesh to the cartesian fluid grid.

$$\mathbf{f}^{l+1}_{f\to s} = \tilde{\mathbf{T}}\mathbf{f}^{l+1}_{s\to f}$$

Step 5:
The Navier-Stokes equations are solved employing the three-order Runge-Kutta method.

Step 6:
If the absolute or relative convergence criteria are satisfied, the solution is updated, otherwise, the index l is incremented and the iteration restarts from step 0.

$$\hat{\mathbf{u}}_s^{n+1} = \hat{\mathbf{u}}_s^{l+1} \quad \mathbf{v}_f^{n+1} = \mathbf{v}_f^{l+1} \quad p_f^{n+1} = p_f^{l+1}$$

Chapter 6

Benchmark Fluid-Structure Interaction Problems with Active Stress

In this chapter, we present the outcomes of parallel numerical simulations conducted on various benchmarks involving the interaction of an incompressible fluid with an elastic solid structure. All experiments were carried out on two high-performance computing systems: the Euler Institute cluster in Lugano, Switzerland, which consists of 42 compute nodes running CentOS 8.2.2004.$x86_64$, and the Piz Daint supercomputer at CSCS, also located in Lugano, Switzerland. The Piz Daint system is a hybrid Cray XC40/XC50 with a substantial capacity of 5320 compute nodes.
The fluid-structure interaction algorithm is implemented in the FE framework MOOSE including the FSI coupling based on a parallel algorithm framework [Krause and Zulian, 2016] and the flow solver IMPACT, validated and widely used for different complex flow configurations [Henniger et al., 2010].

6.1 Modified Turek-Hron benchmark with active force

We begin our analysis by considering the Turek-Hron benchmark, a well-established reference Turek and Hron [2006] frequently utilized to evaluate and compare different numerical methods for fluid-structure interaction (FSI) problems. This benchmark offers specific configurations that aid in testing and validating FSI algorithms.
In the computational domain, the fluid region possesses a length of $L_f = 3.0$ and a height of $H_f = 0.41$. The immersed structure within the domain consists of a disk centered at coordinates $C = (0.2, 0.2)$ relative to the lower-left corner of the rectangular fluid domain. The disk has a radius of $r = 0.05$. An elastic bar

is also incorporated, measuring $l = 0.35$ in length and $h = 0.02$ in height (Fig. 6.1). For the structure's disk, two fixed points are subjected to Dirichlet bound-

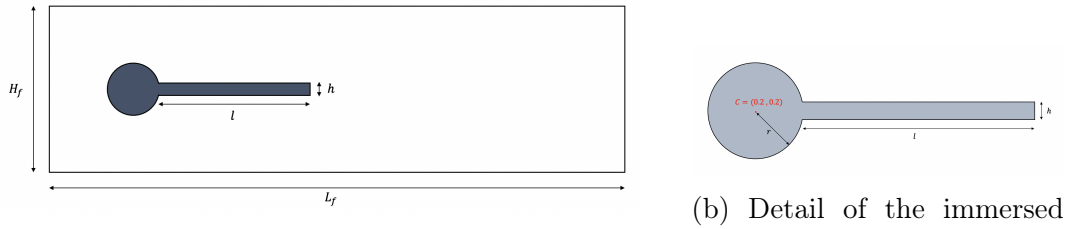

(a) Computational Domain

(b) Detail of the immersed structure

Figure 6.1. Geometry of the modified Turek-Hron benchmark

ary conditions. The fluid channel, on the other hand, employs periodic boundary conditions at both the inlet and outlet, also considering no-slip boundary conditions on the top and the bottom of the fluid domain.
At the inflow section of the left channel, a parabolic velocity profile is enforced by incorporating a fringe forcing term. This ensures that the fluid flow exhibits a well-defined parabolic shape as it enters the computational domain

$$\mathbf{v}_0(\mathbf{x}, t) = 1.5U \cdot \frac{y(H_f - y)}{\left(\frac{H_f}{2}\right)^2} \tag{6.1}$$

such that the mean of the inflow velocity is U and the maximum is $1.5U$.
To address the challenges associated with boundary conditions in simulations of transitional and turbulent boundary layers, the fringe region techniques were introduced Spalart [1989]. These techniques have proven useful in eliminating complications arising from boundary conditions.
In the computational domain, two distinct regions are defined: the utility region and the fringe region. The fringe region, located at the boundaries of the domain, incorporates an additional forcing function on the right-hand side of the Navier-Stokes equations. This compensation accounts for the periodic nature of the problem and mitigates any nonphysical phenomena occurring in the fringe region. It is assumed that these phenomena do not invalidate the solution within the remaining computational domain.
Similar techniques resembling the fringe region approach were utilized in previous studies, such as Kloker et al. [1993]. In that work, a weighting function was employed to suppress vorticity perturbations near the outflow region. Other strategies include implementing a stretched grid combined with a filter to minimize reflections from the outflow boundary Colonius et al. [1993], as well as

modifying the governing equations within the fringe region to expedite convergence to a steady state solution Karni [1992].
In our case, the fringe function has the following form:

$$\lambda(x) = \hat{\lambda}\left[S\left(\frac{x - x_{start}}{\Delta_{rise}}\right) - S\left(\frac{x - x_{end}}{\Delta_{fall}} + 1\right)\right] \tag{6.2}$$

where $\hat{\lambda} = 10$ is the maximum strength of the damping, $x_{start} = 2.5$ and $x_{end} = 3.0$ are the endpoints of the region $x_{start} < x < x_{end}$ where the damping function is nonzero, $\Delta_{rise} = \Delta_{fall} = 0.025$ are the rise and the fall distances respectively, and $S(x)$ is a smooth step function rising from zero for negative x to 1 for $x \geq 1$. We have used

$$S(x) = \begin{cases} 0, & x \leq 0, \\ \frac{1}{1+\exp\left(\frac{1}{x+1} + \frac{1}{x}\right)} & 0 < x < 1, \\ 1, & x \geq 1 \end{cases} \tag{6.3}$$

which has the advantage of having continuous derivates of all orders. In the forcing region, we enforce the velocity profile $\mathbf{v}_0$, and the fluid pressure increase by

$$\mathbf{f}_{fringe} = \lambda(x)\left[(\mathbf{v}_0 - \mathbf{v}_f) + \frac{L_f}{\hat{\lambda}(x_{end} - x_{start})} \cdot \frac{8\mu}{H_f^2}\frac{3U}{2}\right] \tag{6.4}$$

In our analysis, the structure is considered to be both elastic and incompressible. Thus, the material properties are characterized by specifying the second Piola-Kirchhoff tensor S_m using the constitutive law for Saint-Venant-Kirchhoff material.

$$S_m = \lambda_s \mathrm{Tr}(\mathbf{E}) + 2\mu_s \mathbf{E} \tag{6.5}$$

where $\mathbf{E} = \frac{1}{2}(\mathbf{F}^T\mathbf{F} - \mathbf{I})\mathbf{I}$ is the Green-Lagrangian strain tensor and $\lambda_s = k_s - 2\frac{\mu_s}{d}$, with d mesh dimension (Table 6.1).
The fluid domain is discretized using a Cartesian grid with dimensions 769×129, while the solid structure is meshed using 1405 $\mathbb{P}_1$ finite elements, resulting in 806 nodes. The chosen time step for the simulations is $\Delta t = 10^{-5}$ [ms].
In a fluid-structure interaction (FSI) simulation, the choice between using an active stress or an active strain approach depends on the specific requirements and characteristics of the problem at hand.
We refer to a study by [Lin et al., 2019] where they assumed the elastic material to follow the Neo-Hookean model and employed an active strain approach to investigate the swimming motion of thin robots.
Nevertheless, active stress formulations provide greater flexibility in modeling

par. dim.	
$\rho_s\ [kg/m^3]$	1000
$\mu_s\ [kg/ms^2]$	2000000
$k_s\ [kg/ms^2]$	4666667
$\rho_f\ [kg/m^3]$	1000
$\mu_f\ [Pa \cdot s]$	1
$U\ [m/s]$	2

Table 6.1. Parameters of the modified Turek-Hron benchmark

the active behavior of the solid structure; by directly prescribing the stress tensor, it is possible to have more control over the distribution and magnitude of forces and to reproduce and validate the experimental stress profiles in the FSI simulation.
In our setup, we model the first 10% of the length of the bar as a passively deformed solid structure. In the middle, an active segment of length δ is connected, where a periodic time-dependent contractile field is applied (Fig. 6.2). This configuration allows for the incorporation of active behavior in the solid structure. The contraction strength is characterized by the active stress function (assum-

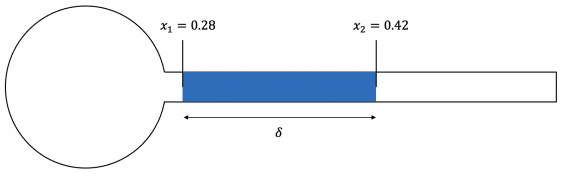

Figure 6.2. Schematic representation of the active segment

ing fibre direction oriented along the x-direction), where the maximum stress is imposed on the surface with an exponential decay in the thickness direction

$$\alpha(t) = \begin{cases} 5 \cdot 10^5 \cdot \sin\left(\dfrac{2\pi t}{T}\right) \cdot \exp\left(-\dfrac{0.21 - y}{0.006667}\right), & 0 \le t \le T/2 \\ 5 \cdot 10^5 \cdot \sin\left(\dfrac{2\pi t}{T}\right) \cdot \exp\left(-\dfrac{y - 0.19}{0.006667}\right), & T/2 < t \le T \end{cases} \tag{6.6}$$

For our numerical simulations, we first applied the active stress along the first principal direction, and we can compare the results with the ones computed without the active term (only fluid-structure interaction)[Fig. 6.5a]. Then the

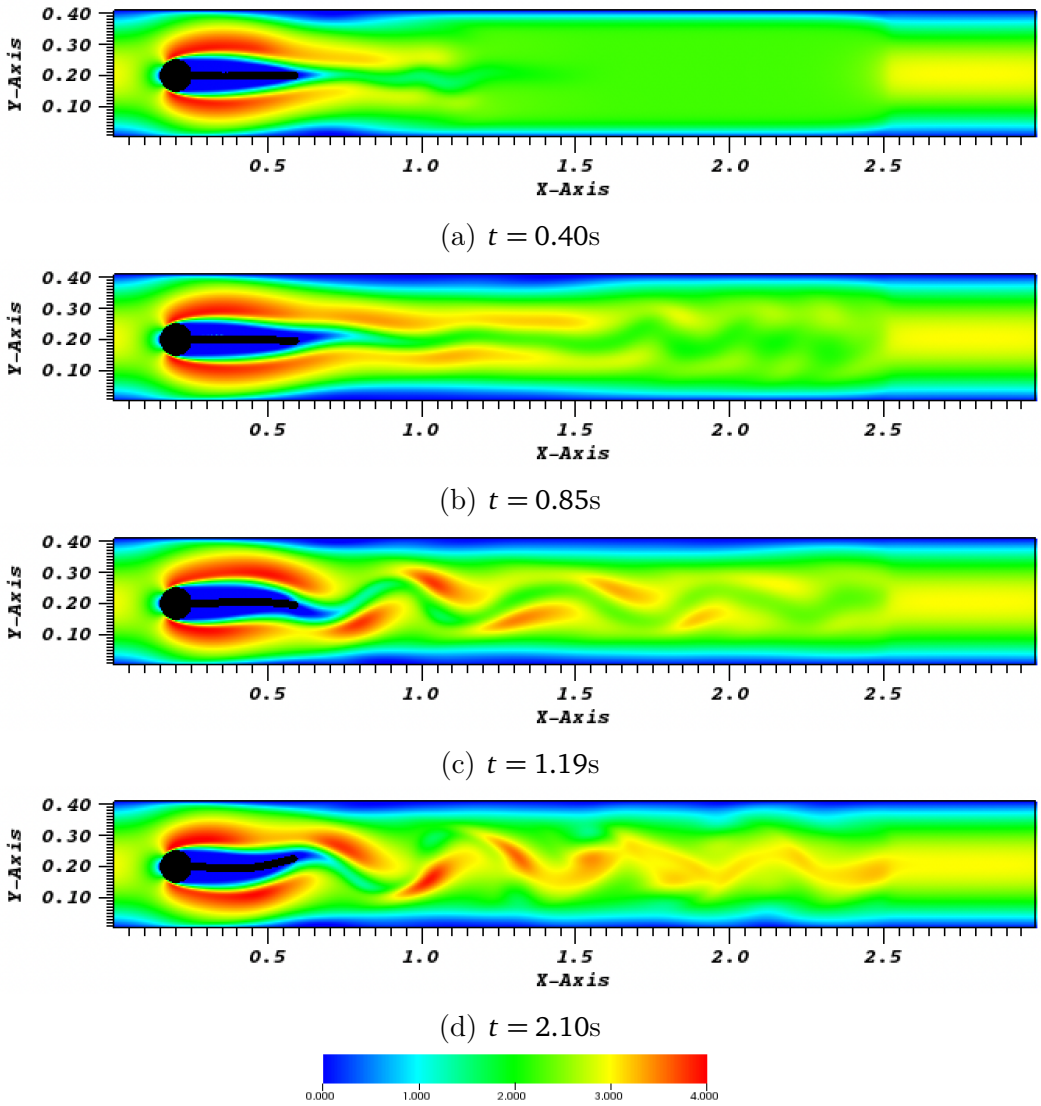

(a) $t = 0.40$s

(b) $t = 0.85$s

(c) $t = 1.19$s

(d) $t = 2.10$s

Figure 6.3. First component of fluid velocity v_{fx} and immersed displaced structure with active stress term applied along the x-direction

active stress was applied along the second principal direction, where periodic behavior was more evident. Also, in this case, the results have been compared with the simulations in the absence of active term [Fig.6.5b].
The FSI simulation using the Turek-Hron benchmark with an active stress approach offers a comprehensive understanding of the dynamic interplay between the fluid and solid domains.
The presence of active stress leads to dynamic changes in the behavior of the

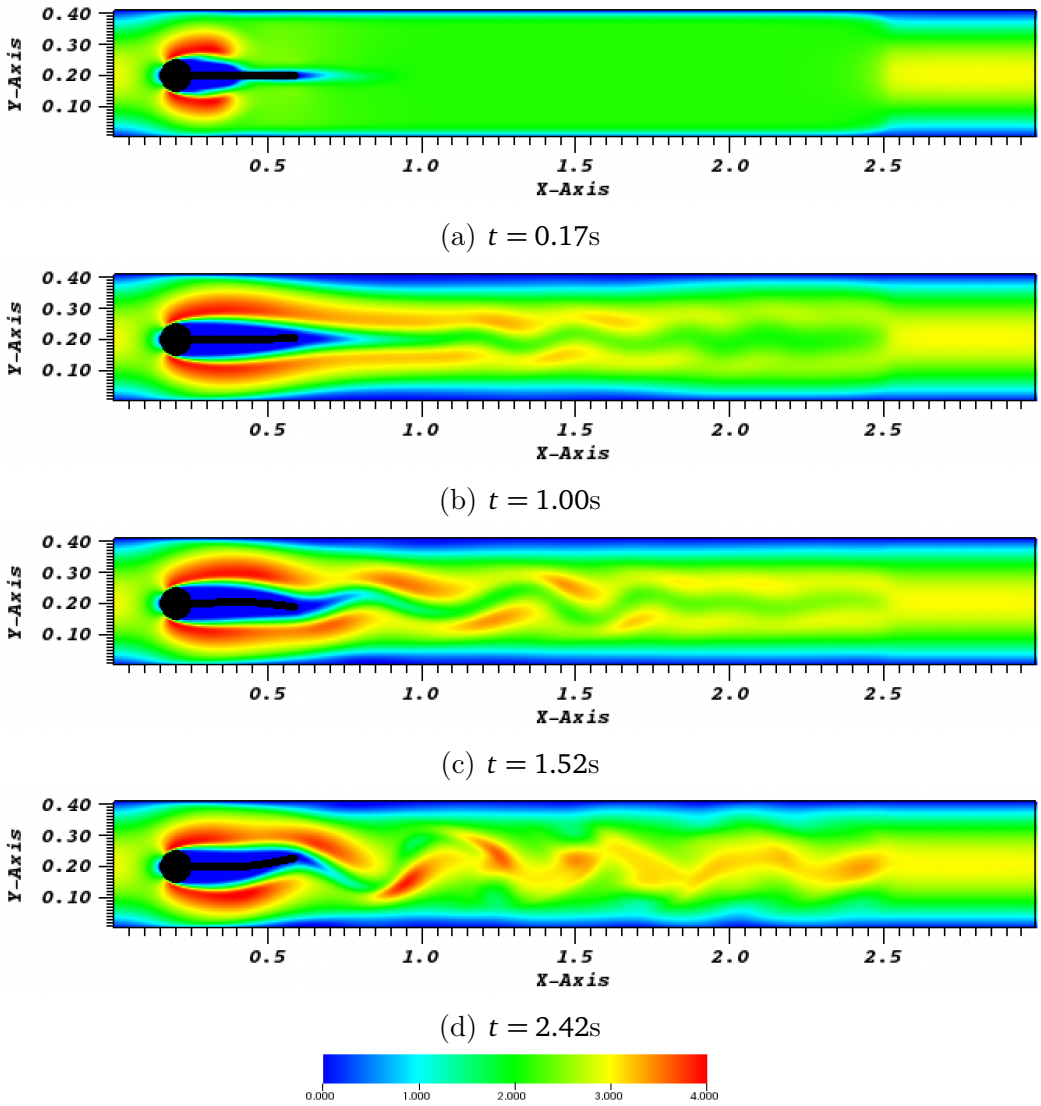

(a) $t = 0.17$s

(b) $t = 1.00$s

(c) $t = 1.52$s

(d) $t = 2.42$s

Figure 6.4. First component of fluid velocity v_{fx} and immersed displaced structure with active stress term applied along the y-direction

fluid and solid domains. These changes are observed in various aspects of the simulation, including the deformation of the solid structure (Fig. 6.5), the flow patterns within the fluid domain, and the interaction between the fluid and the solid (Fig. 6.3 and Fig. 6.4).

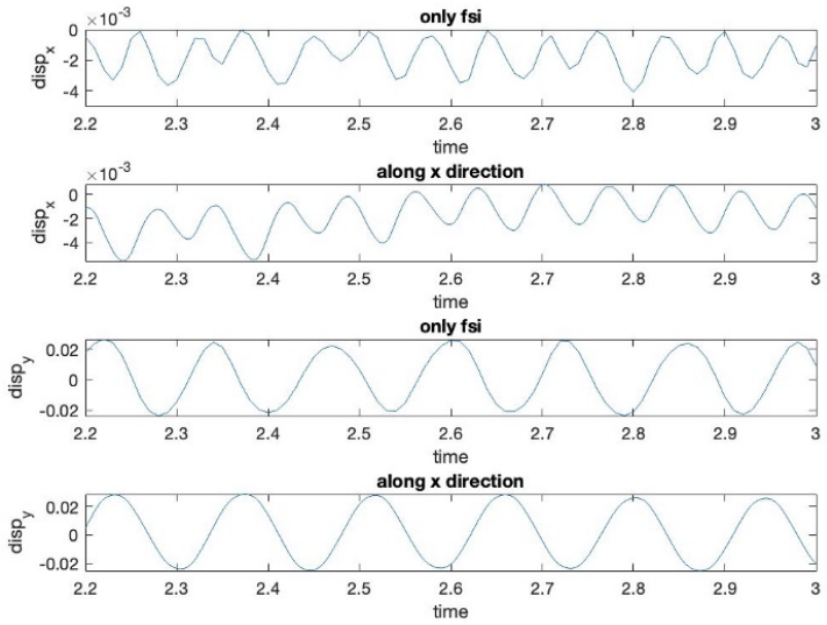

(a) Active stress applied along x-direction

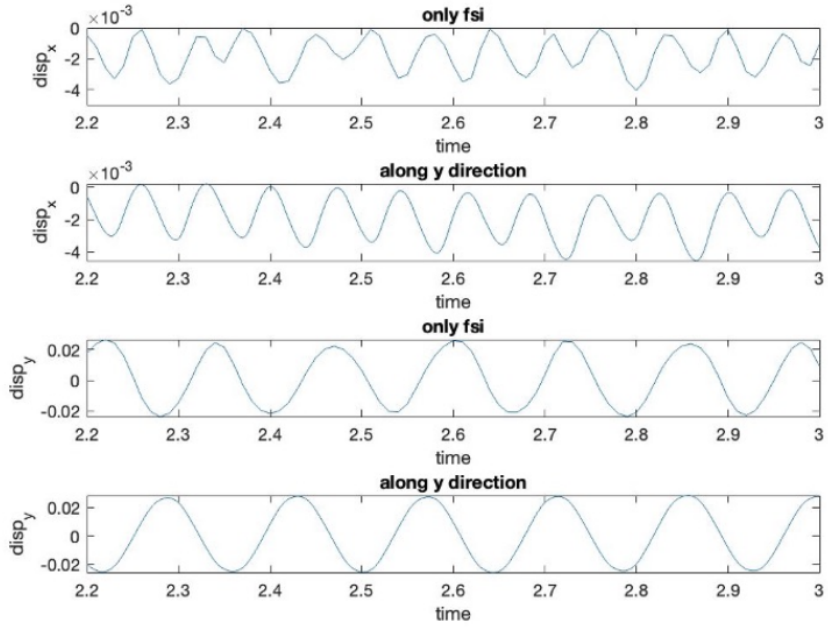

(b) Active stress applied along y-direction

Figure 6.5. First and second components of displacements of a fixed point centered in the active region of the bar in relation to the displacements performed without the active term

6.1.1 Convergence study

A series of fluid-structure interaction (FSI) simulations with active stress have been conducted using different meshes to analyze the convergence behavior in space. From the results obtained, the case where the active stress is applied along the second principal direction has demonstrated superior performance, prompting us to focus on this particular configuration.
For the reference solution, a high-resolution grid was employed, consisting of a 9217×1521 Cartesian grid for the fluid domain. The solid structure was discretized using a mesh composed of 740 032 $\mathbb{P}_1$ elements, corresponding to 372 277 nodes. The time discretization parameter Δt was set to 4×10^{-6}.
To ensure comparability with previous studies, the fluid grids were sized to match the dimensions reported in Nestola et al. [2019]. This ensures that the results can be directly compared to previous research (Table 6.2). In all the simulations, a common time step size of $\Delta t = 1 \times 10^{-5}$ was employed.

	solid mesh nodes/elements	fluid grid
coarse	6065/11 563	1153×193
medium	23 692/46 252	2305×385
fine	93 635/185 008	4609×761
reference	372 277/740 032	9217×1521

Table 6.2. Solid mesh and fluid grid sizes

The L^2-norm errors of the two components of the displacements (u_{sx} and u_{sy}) are computed with respect to the reference solution (Table 6.3), while the ∞-norm errors (Table 6.4) are evaluated for the velocity components of the fluid (v_{fx} and v_{fy}).

mesh	u_{sx} L^2-norm error	u_{sy} L^2-norm error
coarse	0.061844	0.12708
medium	0.03413	0.095554
fine	0.013625	0.05215

Table 6.3. Solid displacement errors

The analysis of the displacement errors in the FSI simulations reveal a convergence rate ranging between first and second order (see Fig. 6.6 and Fig. 6.7). This behavior aligns with the expected convergence rates reported in [Nestola

mesh	v_{fx} L_∞-norm error	v_{fy} L_∞-norm error
coarse	0.017578	0.019206
medium	0.0023986	0.00091625
fine	0.0010562	0.00041403

Table 6.4. Fluid velocity errors

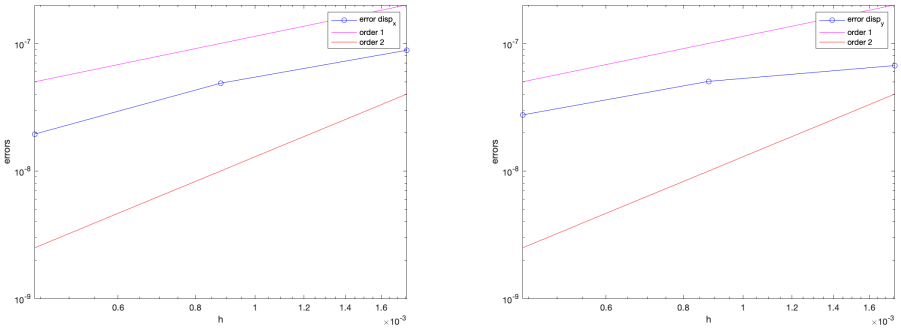

(a) u_{sx} L^2-norm error (b) u_{sy} L^2-norm error

Figure 6.6. Solid displacement field convergence rate

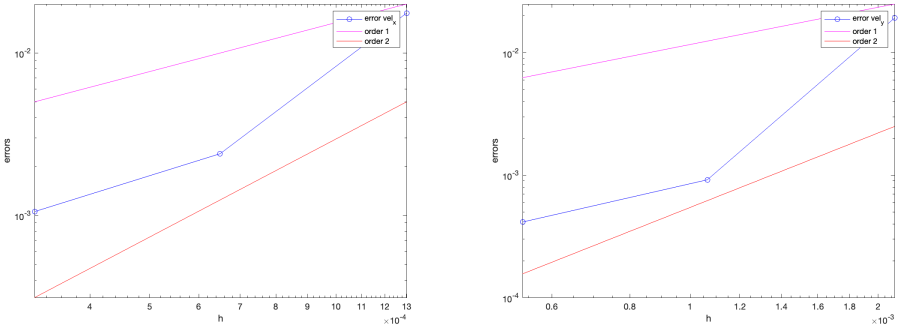

(a) v_{fx} L_∞-norm error (b) v_{fy} L_∞-norm error

Figure 6.7. Fluid velocity convergence rate

et al., 2019].

However, it is noteworthy that the overall convergence rate of the velocity fields is lower, despite employing a sixth-order scheme for the fluid solver. This lower convergence rate can be attributed to the use of $\mathbb{P}_1$ finite elements for the solid subproblem. While the fluid solver utilizes a higher-order scheme, the limitations imposed by the lower-order solid discretization affect the overall convergence

rate. However, It is essential to carefully consider the trade-offs between computational efficiency and accuracy when selecting finite element types for both the fluid and solid domains in FSI simulations. Higher-order finite elements for the solid domain may lead to improved convergence rates but at the cost of increased computational complexity.

6.1.2 Computational Capabilities

The generalized fluid-structure interaction (FSI) framework provides a powerful tool for investigating the complex interplay between fluid dynamics and cardiac mechanics.
The computational performance of the framework was evaluated using the Piz Daint supercomputer machine. The machine's high-performance computing capabilities allowed for efficient execution of the simulations and enabling the investigation of realistic three-dimensional cardiac models.
For the two-dimensional simulations, a single node consisting of 8 processors

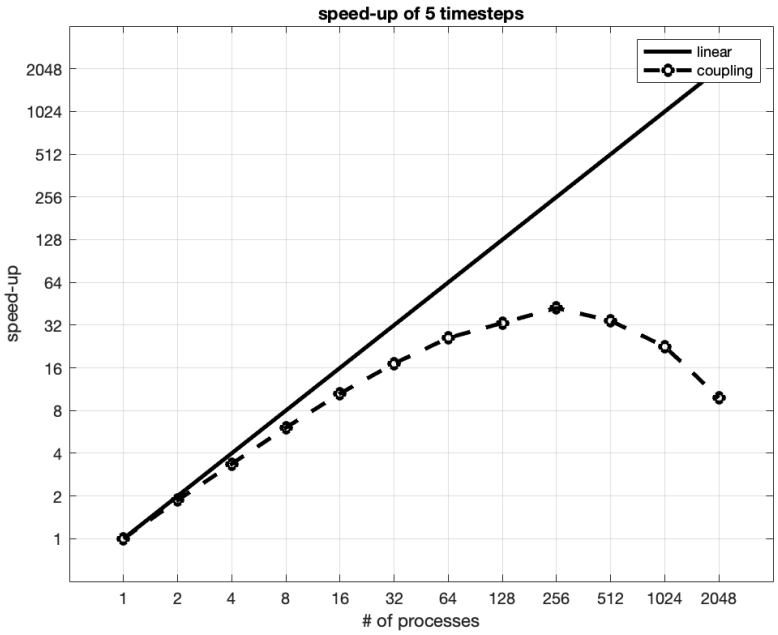

Figure 6.8. Perfomance of the parallel computation of FSI problem compared with the ideal speed-up.

was employed. This configuration provided sufficient computational power to accurately capture the fluid-structure interaction phenomena in a reduced dimen-

sionality setting, while in the case of three-dimensional simulations, the framework utilized 8 nodes, each containing 32 processors.
To assess the scalability and performance of the framework, a strong scaling technique was employed. This technique involves increasing the number of processors while keeping the problem size constant. The framework exhibited near-optimal scaling, indicating that the computational workload was effectively distributed among the processors, resulting in efficient utilization of computing resources (see Fig. 6.8).
It is important to note that the computational performance discussed here does not take into account the electrophysiological subproblem. The coupling between the electrophysiological and mechanical aspects of the heart was achieved through the separated evaluation of the activation map, which was then incorporated into the formulation of the active stress. This approach allowed for the investigation of the electromechanical coupling without explicitly solving the electrophysiological problem.

6.2 A two-dimensional idealized left ventricle

The cardiac cycle describes the performances of the atria and ventricles from the beginning of one heartbeat to the beginning of the next. Each cardiac cycle has a diastolic phase (called diastole), where the heart's chamber is relaxed and refills with blood, and a systolic phase (called systole), characterized by robust contraction and pumping of blood (see Appendix).
Since ventricular contraction is the most important from a dynamic point of view, we focus on the ventricular cardiac cycle, and systole and diastole can be further subdivided. The first phase of ventricular systole consists of an isovolumetric contraction, while the second phase is referred to as ejection. The diastolic phase starts with the closing of semilunar valves, followed by an isovolumetric relaxation. The imbalance of pressure between the atria and ventricles involves the opening of the atrioventricular (AV) valves with a rapid filling, then a slow filling phase occurs (called diastasis), whose length depends on the heart rate.

This section introduces a benchmark that serves as an initial approximation to the physiology of the human left ventricle, represented within an idealized vertical section immersed in a fluid channel.
The fluid domain in the benchmark has a length of $L_f = 0.7$ [m] and a height of $H_f = 0.3$ [m]. It is important to note that the fluid, in this case, is considered to be incompressible and exhibits Newtonian behavior.
The immersed structure comprises the section of the ventricle connected to an open channel. The channel has a thickness of 0.0134 [m] and a length of $L = 0.15$ [m]. The surface that represents the ventricle is defined by the inner curve, which corresponds to the endocardial surface, and the outer curve, which represents the epicardial surface. These curves delineate the boundaries of the approximated ventricle in the benchmark (Fig. 6.9). Each curve is parametrized by ellipses equations with different values for semiaxes

$$\begin{aligned} a_{epi} &= 0.08[\text{m}] \qquad b_{epi} = 0.04[\text{m}] \\ a_{endo} &= 0.068[\text{m}] \quad b_{endo} = 0.028[\text{m}] \end{aligned}$$

The top of the channel is fixed at $x = 0.01$.
To account for the high deformability of human cardiac tissue, the solid domain in the benchmark is divided into two separate regions. The first region encompasses the open channel and a small portion of the ventricle ($x < 0.183473$), while the second region includes the remaining portion of the ventricle's section (see Fig. 6.10). This division allows for the consideration of two distinct groups of coefficients for the hyperelastic constitutive material models used to describe

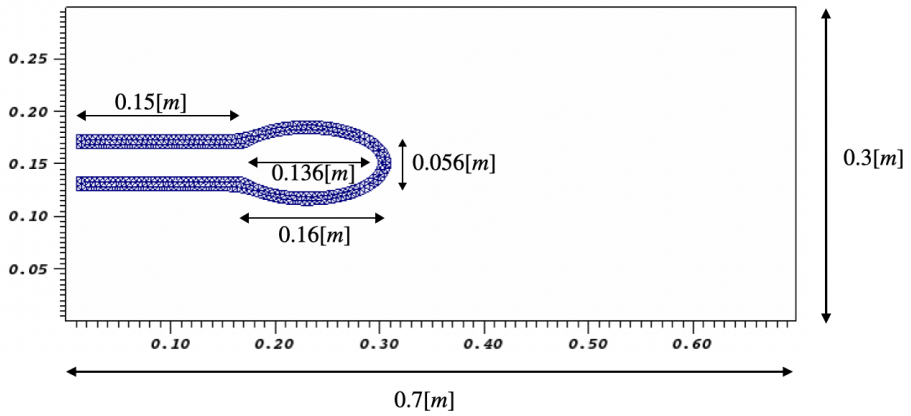

Figure 6.9. Computational domain representing the rectangular fluid domain and the immersed two-dimensional idealized ventricle connected with an open channel

the structure.
In particular, assuming that the fiber direction within the tissue is oriented along the x-direction, the material properties are assumed to be isotropic. The behavior of the material in this region is characterized by the second Piola-Kirchhoff tensor S_m, which is determined by the constitutive law for Saint-Venant-Kirchhoff material (see Table 6.5).
By considering different material properties for the two regions of the ventricle, the benchmark aims to capture the heterogeneity and anisotropic nature of the cardiac tissue, allowing for a more accurate representation of its mechanical response and deformation characteristics.

$$S_m = \lambda_s \mathrm{Tr}(\mathbf{E}) + 2\mu_s \mathbf{E} \tag{6.7}$$

where $\lambda_s = k_s - \mu_s$.
The first set of parameters used for the channel's material is equal to the one used for simulations with the modified Turk-Hron benchmark, while the second group takes into account the soft property of cardiac tissue.
The fluid domain is discretized using a cartesian grid 561×241, while the solid mesh consists of 727 $\mathbb{P}_1$ finite elements with 492 nodes. The time step is chosen at $\Delta t = 10^{-5}$[ms].

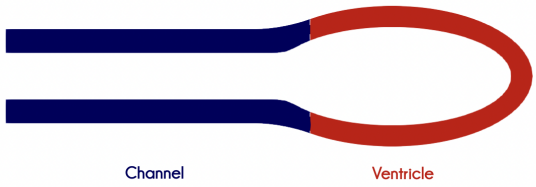

Figure 6.10. Representation of the partition of the solid domain: the first subdomain colored in blue and the second domain colored in red.

par. dim.	
μ_s[kg/ms^2]	2000000
k_s[kg/ms^2]	4666667

(a) Bulk and shear moduli used for the cannel's material

par. dim.	
μ_s[kg/ms^2]	250000
k_s[kg/ms^2]	583333

(b) Bulk and shear moduli used for the ventricle's material

Table 6.5. Material coefficients of the two-dimensional idealized ventricle.

6.2.1 Simulation of filling phase

The E-wave is an important component of the cardiac cycle and represents the passive flow of blood from the left atrium to the left ventricle. It occurs following the closing of the aortic valve and the subsequent relaxation of the ventricular muscles.
During this phase, the ventricular muscles relax, leading to a rapid decrease in ventricular pressure. This pressure gradient, combined with the opening of the mitral valve (the atrioventricular valve located between the left atrium and left ventricle), facilitates the flow of blood from the atrium to the ventricle.
The simulation of the rapid filling of the left ventricle using the idealized two-dimensional benchmark provided valuable insights into the fluid dynamics and behavior of the ventricular filling process (Fig. 6.13). The simulation was performed starting from a relaxed conformation of the solid without including a model for the mitral valve. The fluid's viscosity and density parameters were set to the same values as in the Turek-Hron simulation, with the reference length set at $L_{ref} = 0.1$.

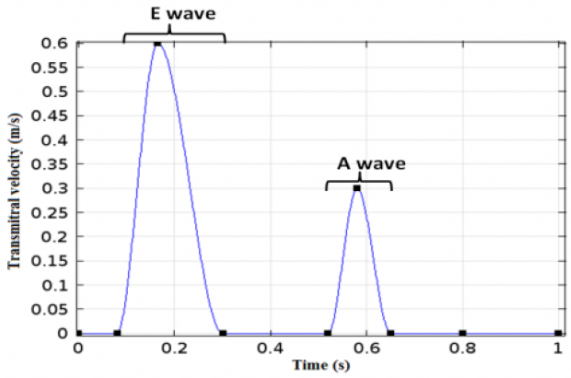

Figure 6.11. Inlet flow velocity profile proposed in [Chan et al., 2012]

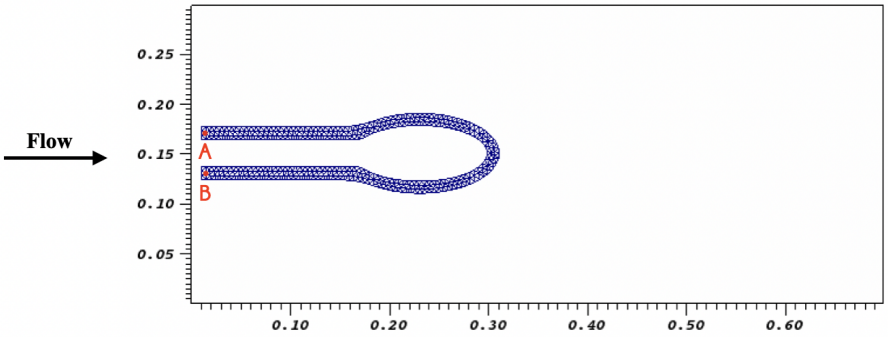

Figure 6.12. Relaxed two-dimensional ventricle and two fixed points (A and B) at the top of the channel

A null Dirichlet boundary condition is imposed at two fixed points of the structure's channel (points A and B in (Fig. 6.12)) with periodic boundary conditions at the inlet and outlet of the fluid domain and no-slip boundary conditions on the top and bottom walls.
To enforce a sinusoidal velocity profile at the left fluid channel inflow, the fringe force technique was employed. This technique allowed us to impose a time-varying velocity profile that mimics the filling phases observed in clinical data.

$$\mathbf{v}_0(\mathbf{x}, t) = 1.5U \cdot \left[0.0001 \sin\left(\frac{\pi}{2}t\right)\right] \tag{6.8}$$

In this case, the fringe function has the same form of (6.2), where $\hat{\lambda} = 10$, the endpoint of the fringe region are $x_{start} = -0.02$, $x_{end} = 0.02$ and the rise and fall distances are $\Delta_{rise} = 0.01$, $\Delta_{fall} = 0.005$ respectively.
Comparisons were made between the velocity profile at two distinct points in our

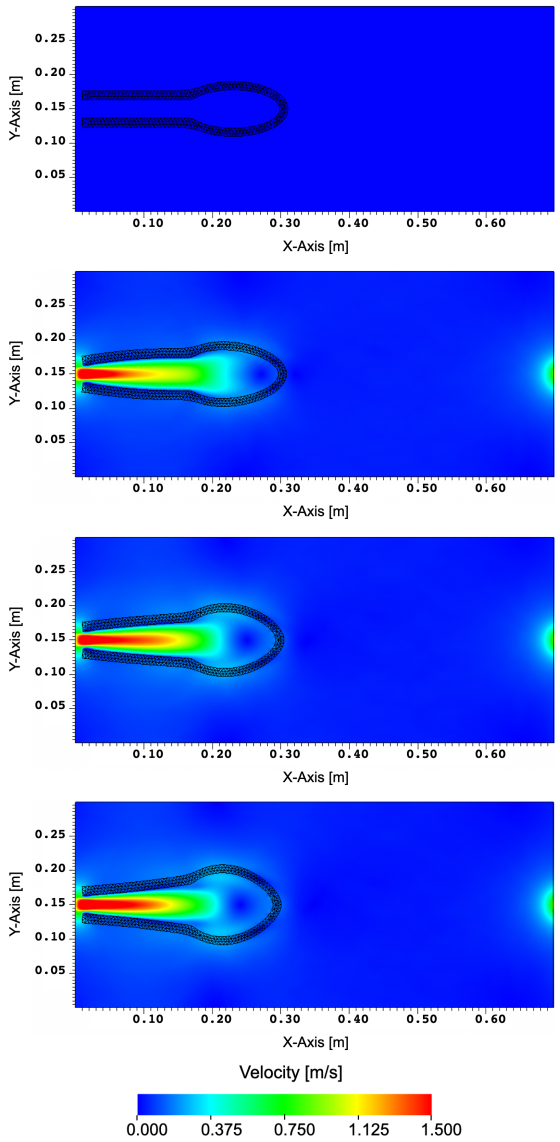

Figure 6.13. Fluid velocity m/s at times $t = 0.00, 0.14, 0.16, 0.18$[s] and immersed displaced ventricle

simulation and a profile proposed in a previous study [Chan et al., 2012], where the effects of the dilated cardiomyopathy (characterized by low ejection fraction and decreased wall motion) on the intraventricular flow dynamics was studied. In particular, the velocity profile was adapted from clinical data and represented a time-varying pattern of the filling phase, including the E-wave, diastasis, and A-wave (see Fig. 6.11).

The simulation results revealed important aspects of the ventricular filling process. The imposed sinusoidal velocity profile accurately captured the filling phases, and the E-wave, representing the rapid early diastolic filling, was clearly evident in the velocity profile (Fig. 6.14). The simulation revealed that the velocity inside

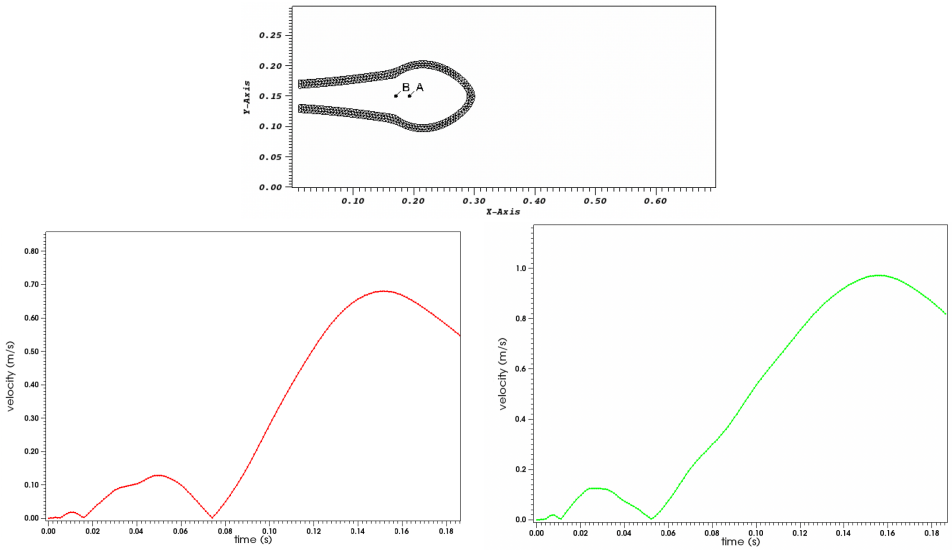

(a) point A (b) point B

Figure 6.14. Velocity profile at two fixed points of coordinates A(0.1925, 0.15), inside the ventricle (a), and B(0.17, 0.15) close to the entry of the ventricle region (b).

the ventricle reached a peak value of 0.68 m/s (Fig. 6.15), which is comparable to the velocity reported in [Chan et al., 2012].
However, it is important to note that our simulation did not include a model for the mitral valve, and it may have influenced the flow patterns and dynamics within the ventricle. Specifically, without the presence of the valve's geometry, the jet of fluid entering the ventricle may not have extended as far down into the ventricle as reported in another study [Kronborg et al., 2022a], where different geometries for the mitral valve were considered.
Despite the absence of the mitral valve model, our simulation still provided valuable insights into the inflow dynamics of the left ventricle, and the exact value of the E-wave peak can vary depending on factors such as age, cardiac health, and individual variations.
However, the peak velocity of 0.68 m/s indicates a relatively rapid inflow, contributing to efficient filling of the ventricle during the diastolic phase. This velocity magnitude is consistent with the findings also reported in [Sattarzadeh et al.,

2015], where the mitral peak E velocity of the studied population is 0.7 ± 0.1, which suggests that our simulation accurately captured the flow characteristics observed in clinical data.
Our results highlight the importance of considering the mitral valve geometry when aiming to reproduce the full extent of the jet. Future studies incorporating a comprehensive mitral valve model may provide a more detailed representation of the inflow patterns and further improve the accuracy of the simulation.

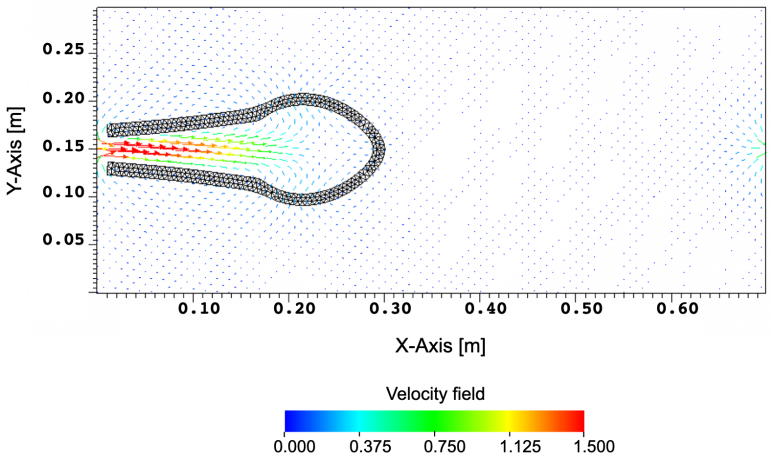

Figure 6.15. Velocity field at time $t = 0.18$s and displaced 2D ventricle mesh.

6.2.2 Simulation of contraction

Ventricular systole is the phase of the cardiac cycle that begins when the heart is filled with blood and subsequently contracts, forcing blood into the aorta and pulmonary trunk. This process consists of two main phases: the isovolumetric contraction and the ejection [Little, 2001]. During the isovolumetric contraction, the left ventricle contracts forcefully. All the heart valves, including the mitral valve (between the left atrium and left ventricle) and aortic valve (between the left ventricle and aorta), are closed (see Appendix). This closure prevents any backflow of blood into the atrium and aorta. Despite the contraction, there is no change in the volume of blood within the ventricle. As the ventricular pressure exceeds the pressure in the aorta, the aortic valve opens. This allows the blood to be ejected from the left ventricle into the aorta and subsequently distributed to the entire body. The contraction of the ventricle is rapid and forceful during this phase, facilitating efficient blood ejection. To simulate the rapid contraction, we partitioned the domain into two distinct subdomains. In this approach, we

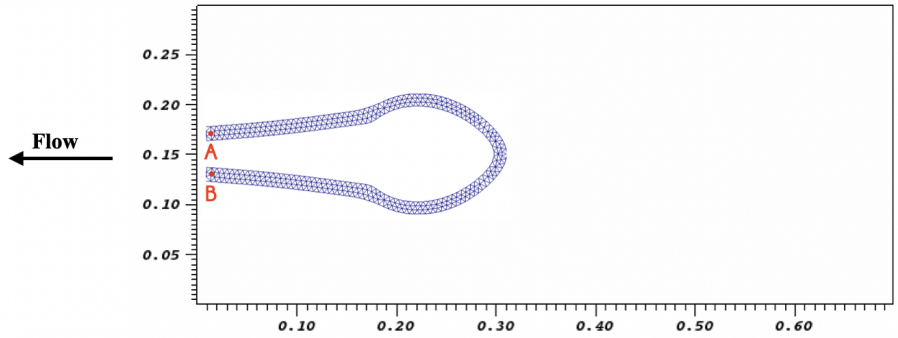

Figure 6.16. Deformed two-dimensional ventricle and two fixed points (A and B) at the top of the channel

designate the channel's subdomain (where $x < 0.183473$) as passive, meaning it does not exhibit active contraction. On the other hand, the subdomain representing the ventricle is subjected to a contractile field (see Fig. 6.10).
The contraction process is characterized by a linear time-dependent active stress function, which is incorporated into the elastodynamics equation using the first Piola-Kirchhoff stress. This stress function takes into account the orientation of the fibers present in the ventricular tissue. By considering these factors, we can accurately model the mechanical behavior of the ventricle during contraction in our simulation with the following form:

$$\begin{aligned} \hat{\mathbf{P}} &= \hat{\mathbf{P}}_m + \hat{\mathbf{P}}_a \\ \hat{\mathbf{P}}_a &= \alpha(t)\mathbf{F}\mathbf{g}\mathbf{n} \otimes \mathbf{n} \end{aligned} \tag{6.9}$$

with $\hat{\mathbf{P}}_m$ first Piola-Kirchoff passive stress tensor and

$$\alpha(t) = (t \leq 0.0001) \cdot 0.0 + (10^6 \cdot (t - 0.0001)) \cdot (t > 0.0001). \tag{6.10}$$

To initiate the simulation, the deformed solid mesh obtained from the final step of the inflation simulation is utilized as the initial condition for the solid subproblem. This ensures that the geometry accurately represents the deformed state of the ventricle before contraction.
To establish the boundary conditions, we set null Dirichlet boundary conditions at two fixed points located at the top of the channel, specifically points A and B, as illustrated in Fig.6.16. Additionally, in the fluid domain, zero flow is considered at the left side, while the top and bottom walls exhibit no-slip boundary conditions.

To avoid reflection effects resulting from the outflow generated by the ven-

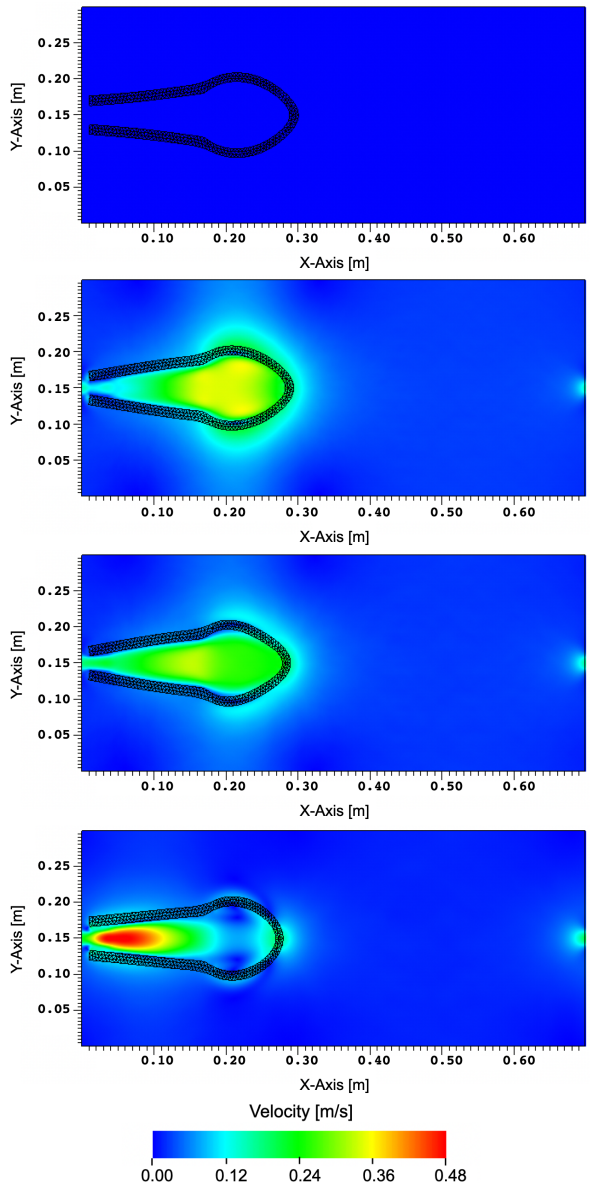

Figure 6.17. Fluid velocity m/s at time $t = 0.00, 0.04, 0.06, 0.12$ and the displaced ventricular mesh showing the active contraction

tricular contraction, a second fringe force function is generated. This function incorporates a pressure difference in the opposite direction compared to the previously defined fringe forcing condition (6.4). By implementing this opposite pressure difference, the simulation accounts for the impact of the ventricular

contraction without inducing unwanted reflections in the fluid domain.

$$\mathbf{f}_{fringe} = \lambda(x)\left[(0.0 - \mathbf{v}_f) - \frac{L_f}{\hat{\lambda}(x_{end} - x_{start})} \cdot \frac{8\mu}{H_f^2}\frac{3U}{2}\right] \tag{6.11}$$

with $\hat{\lambda} = 10$, $x_{start} = -0.02$, $x_{end} = 0.02$ and $\Delta_{rise} = 0.0005$, $\Delta_{fall} = 0.001$. By plotting the module of the velocity, we can observe the flow patterns and understand the overall fluid dynamics during ventricular contraction (Fig. 6.17). This representation provides a visual insight into the movement and direction of the fluid within the ventricle and the connected channel.
Simultaneously, the simulation also showcases the active contraction of the ventricular mesh. This feature demonstrates how the ventricular tissue changes shape and size during the contraction process (Fig. 6.17).

Furthermore, the velocity profiles at two fixed points serve as important indi-

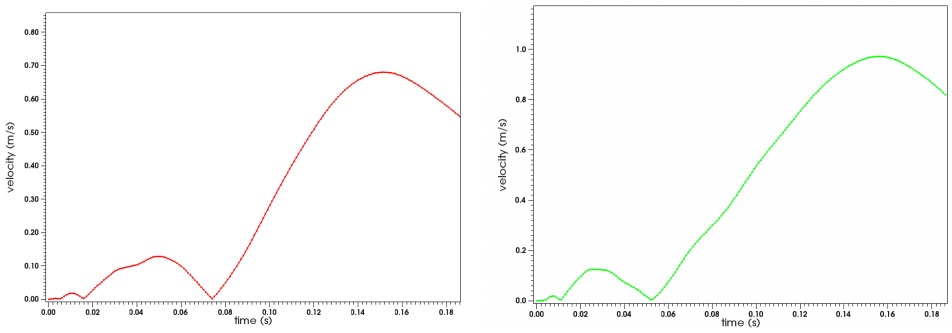

(a) point A (b) point B

Figure 6.18. Velocity profile at two fixed point $A = (0.1925, 0.15)$ and $B = (0.17, 0.15)$ respect of time

cators of fluid dynamics (see Fig. 6.18). The first point A, located inside the ventricle, shows the velocity distribution within the ventricle during contraction. This provides valuable information about the flow characteristics and velocity magnitudes inside the ventricular chamber, where the velocity reaches a peak value of 0.34 m/s.
The second fixed point B, positioned inside the connected channel but close to the entry of the ventricle, allows us to assess the influence of the absence of the aortic valve on the dynamics in the ventricular apex. The velocity profile at this point helps us understand how the absence of the aortic valve affects the fluid flow patterns and velocities within the ventricle.

Additionally, through the velocity field, we can observe the relationship between

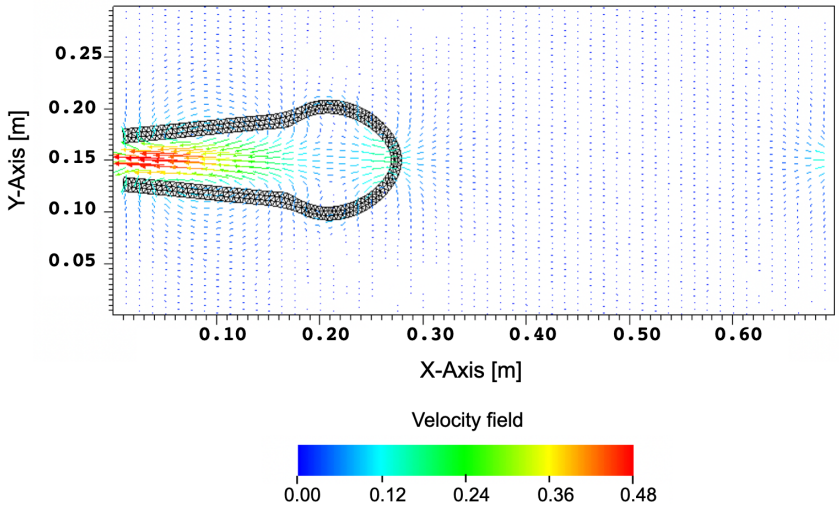

Figure 6.19. Velocity field at time $t = 0.12$s and the conctracted two-dimensional ventricle.

the flow increase and the reduction in the section of the channel (Fig. 6.19). This observation highlights how changes in the geometry and valvular dynamics impact the flow dynamics within the ventricle and the connected channel.

6.3 A three-dimensional idealized left ventricle

In this section, we demonstrate the capabilities of the generalized FSI framework with active stress through a three-dimensional application involving a truncated ellipsoid, as inspired by Land et al. [2015a], within a cubic fluid domain.
Initially, we perform a simulation using a linear function to define the active stress, generating a uniform contraction throughout the truncated ellipsoid. By examining the effects of this simplified active stress model, we gain initial insights into the overall behavior of the system and lay the foundation for more complex and realistic simulations.
Subsequently, we introduce the concept of activation maps, which is a graphical

$\mu_s\ [kPa]$	b_f	b_t	b_{fs}
0.493	38.06	4.11	45.07

Table 6.6. Guccione-Costa constitutive law parameters of the truncated ellipsoid

representation that illustrates the timing and propagation of electrical activation within cardiac or biological tissue. It provides a spatial depiction of the initiation and spread of electrical impulses responsible for the heart's contraction. Two distinct activation maps are utilized: one generated by the eikonal model and another generated by the monodomain model coupled with Luo-Rudy ionic model.
The eikonal model offers quick approximations of activation patterns with a simplified representation of electrical propagation, while the monodomain model provides a more detailed and accurate description of electrical activity but requires more computational resources. Once the activation maps are applied, the simulation evaluates the electrical activity on each node and the information is used to generate a three-dimensional contraction of the heart.
All the three-dimensional simulations discussed in this chapter were performed on the Piz Daint supercomputer machine. Each simulation utilized 8 nodes, with each node consisting of 32 processors. The simulations were executed using a time step of $\Delta t = 1e^{-5}$, which ensured accurate temporal resolution of the cardiac dynamics.
The computational time required for each simulation was approximately 13 hours. The high-performance computing capabilities of the Piz Daint machine, coupled with the parallel implementation of the solution strategy, enabled efficient and timely execution of the simulations.
As in Chapter 3 for the electrophysiological simulations, the orientation of the

fibres is estimated following Potse et al. [2006a].

We consider the Guccione-Costa constitutive law [Guccione et al., 1995] for

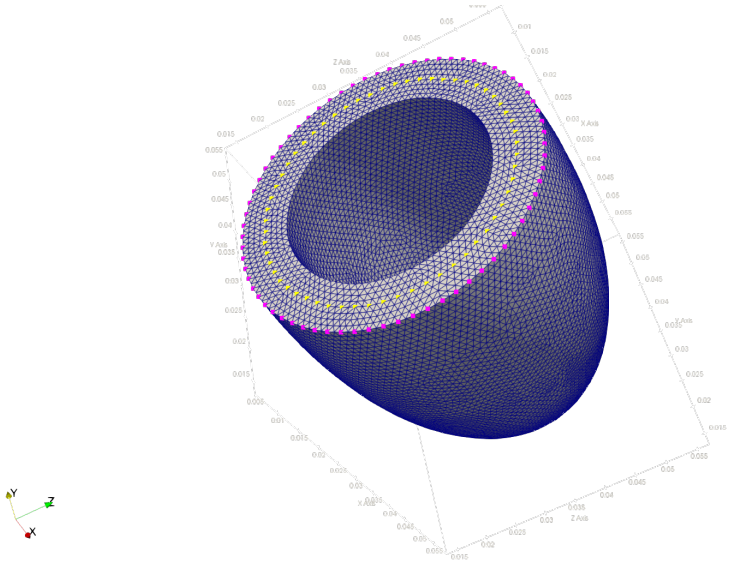

Figure 6.20. Relaxed three-dimensional ventricle and outer and internal nodesets

modeling the elastic behavior of the human ventricle with the constitutive parameters taken from Nikou et al. [2015] and reported in Tab. 6.6. Null Dirichlet Boundary conditions are imposed in the outer and internal ring of the ventricle base with periodic boundary conditions at the inlet and outlet of the fluid domain for all the following simulations (see Fig. 6.20).

In this study, the fluid properties were carefully selected to achieve a desired flow regime in the computational fluid dynamics simulations. Specifically, the fluid density was set to 1060 [kg/m^3], while the viscosity was chosen as 0.004 [$Pa \cdot s$]. To determine the reference length and velocity, we aimed to attain a Reynolds number on the order of 10^4, which corresponds to a turbulent flow regime. This choice was based on the recommendations presented in [Kronborg et al., 2022b], which highlighted the importance of considering turbulent effects in cardiovascular flow simulations.

6.3.1 Simulation of uniform contraction

In this section, we present the results of our simulation using a linear function to define the active stress, resulting in a uniform contraction of the truncated

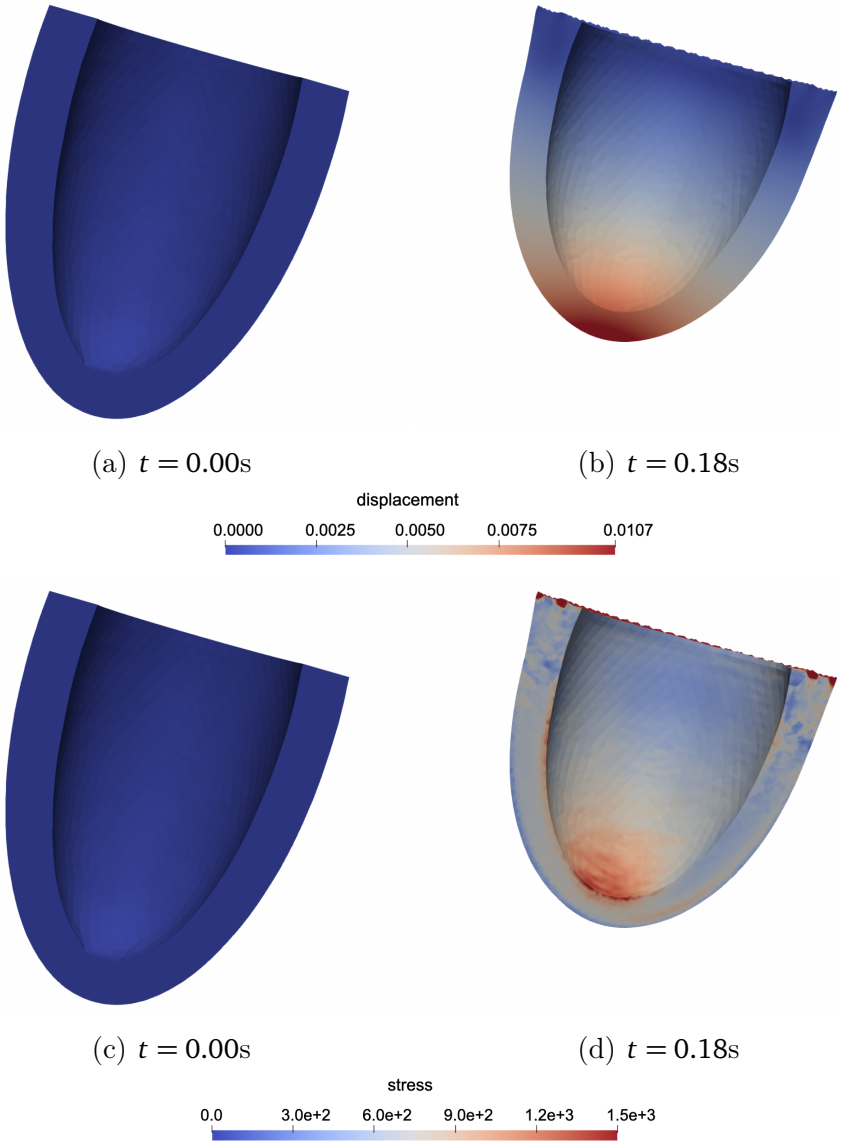

(a) $t = 0.00$s (b) $t = 0.18$s

(c) $t = 0.00$s (d) $t = 0.18$s

Figure 6.21. Uniform contraction. Displacement of the ventricle domain and Von Mises stress.

ellipsoid immersed in a three-dimensional fluid domain. The fluid domain has dimensions of $L_{f,x} = 0.07$[m], $L_{f,y} = 0.07$[m] and $L_{f,z} = 0.07$[m], while the solid geometry corresponds to the same configuration described in the second and third benchmarks of Land et al. [2015b]. The solid geometry is scaled by a factor of 0.005, translated, and rotated to ensure that the base plane is fixed at $x = 0.005$ [m] and centered at $(0.005, 0.035, 0.035)$.

The fluid and solid domains remain identical for all computations related to the contraction process. The fluid domain is discretized using a Cartesian grid with dimensions of 161 × 161 × 161 points, providing a suitable resolution for capturing the fluid dynamics. On the other hand, the ventricular structure is represented using 324376 $\mathbb{P}_1$ elements and 61216 nodes, enabling a detailed description of the solid mechanics.
During the simulation, we employ a cubical time-dependent active stress function to model the rapid contraction during the systolic phase representing the expected behavior during the cardiac cycle:

$$\alpha(t) = 0.0 \cdot (t \leq 0.0001) + \frac{10^3}{(0.2 - 0.0001)^3} \cdot (t - 0.0001)^3 \cdot (t > 0.0001) \quad (6.12)$$

Furthermore, we impose zero flow at the inlet of the fluid domain to simulate a closed system, consistent with the absence of an aortic valve geometry. No-slip boundary conditions are enforced at the top and bottom walls of the fluid domain.
To evaluate the displacement of the solid structure, we compare our results (see Fig 6.21) with those reported in [Bucelli et al., 2023]. Specifically, we examine the magnitude of the velocity (Fig. 6.22) and its profile at a specific point located inside the ventricle (Fig. 6.24) but close to the entry of the truncated ellipsoid. It is important to note that our simulation, similar to the previous two-dimensional study, does not incorporate the aortic valve geometry. Despite this omission, we anticipate that the maximum velocity value and flow magnitude (Fig. 6.23) will remain within a comparable range to those presented in [Bucelli et al., 2023]. By making this comparison, we can assess the agreement between our findings and the established results in the literature.

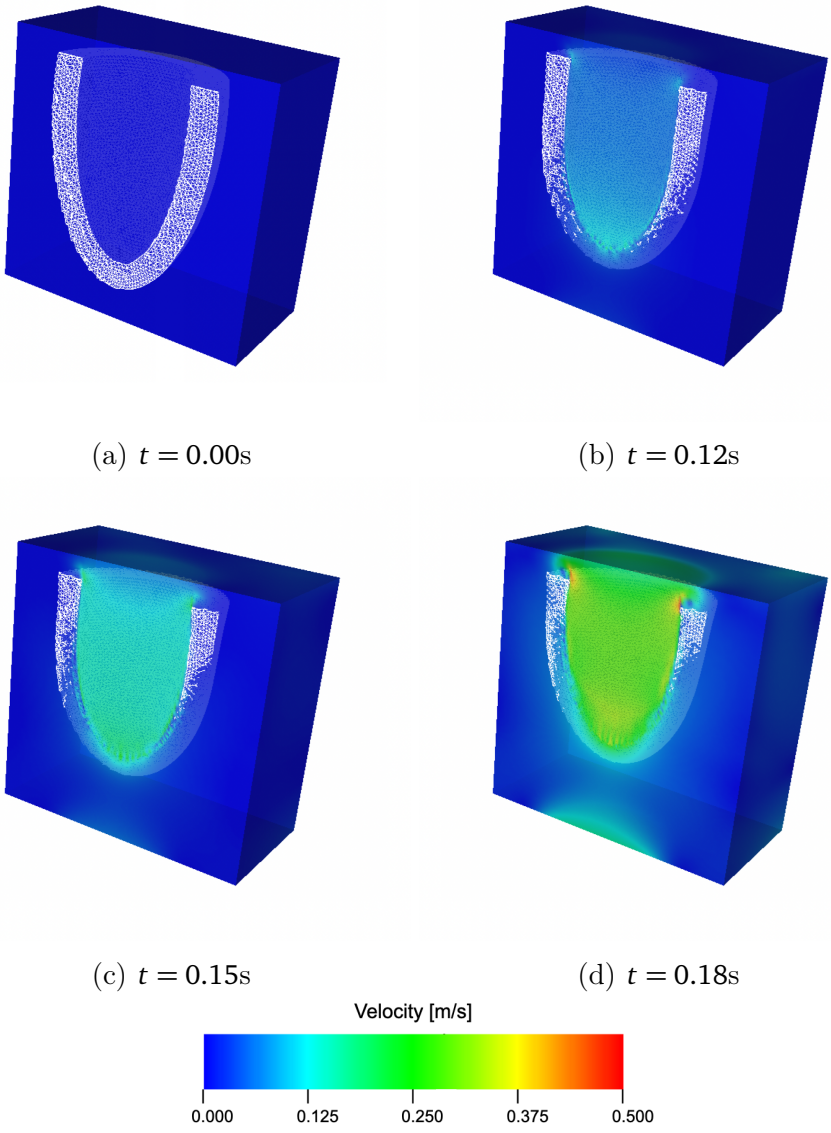

(a) $t = 0.00$s (b) $t = 0.12$s

(c) $t = 0.15$s (d) $t = 0.18$s

Figure 6.22. Uniform contraction. Slice perspective of fluid velocity [m/s] and immersed displaced ventricle with uniform active stress.

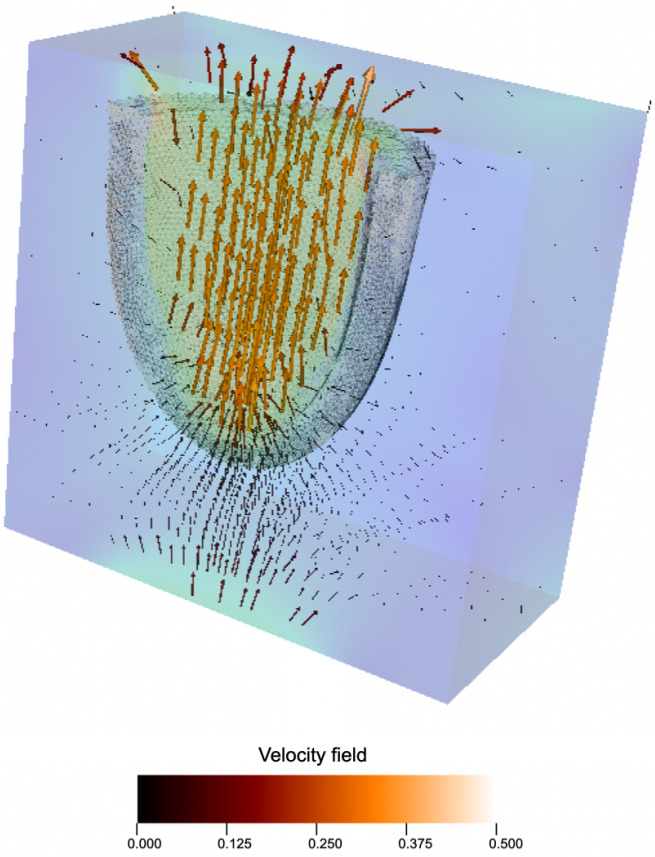

Figure 6.23. Uniform contraction. Velocity field at time $t = 0.18$[s].

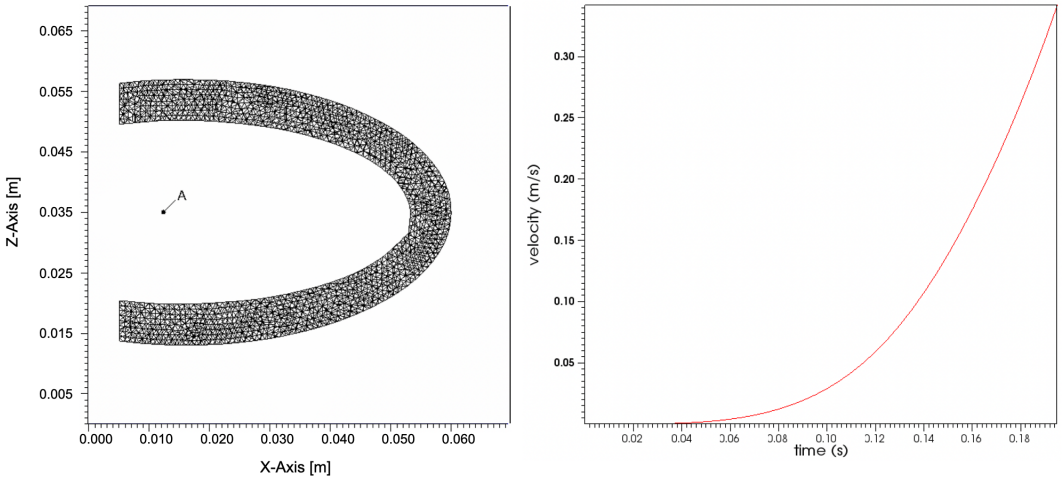

Figure 6.24. Uniform contraction. Velocity profile over time at a fixed point A(0.0122302, 0.035, 0.035) close to the entry of the ventricle.

6.3.2 One way electro-fluid-structure coupling

Eikonal model

In this section, we present the results of the simulation for the contraction driven by an active force, which in turn depends on an activation map constructed through the resolution of an Eikonal model (see Fig. 6.25). Although this model does not accurately represent cardiac electrophysiology, it provides an initial and unique bridge, given the absence of a complete electromechanical coupling, between a generalized fluid-structure model based on immersed domains and the L2 projection, which includes the description of an active term.

The fluid domain in our simulation maintains the same dimensions as in the

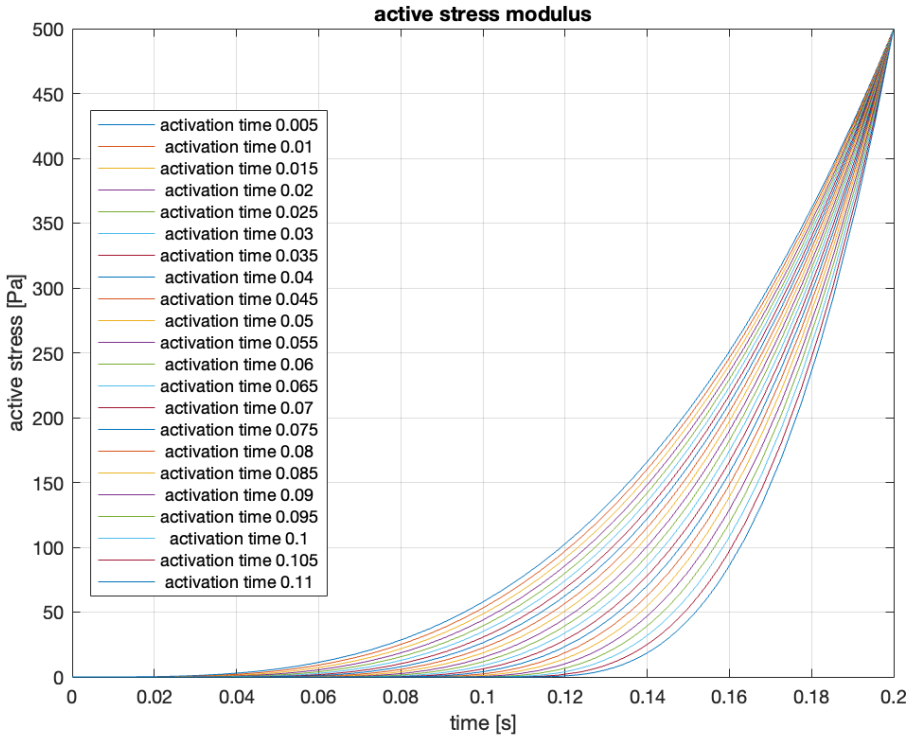

Figure 6.25. Time dependent active stress function for different cellular time activation.

uniform contraction simulation. The dimensions of the fluid domain are set as $L_{f,x} = 0.07$ m, $L_{f,y} = 0.07$ m, and $L_{f,z} = 0.07$ m. On the other hand, the solid geometry, following [Land et al., 2015a], is scaled by a factor of 0.0025 and translated such that the base plane is fixed at $x = 0.005$ m and centered at

$(0.005, 0.035, 0.035)$.
The discretization of the fluid domain is performed using a Cartesian grid with $161 \times 161 \times 161$ points. The grid is refined near the solid apex to capture the details of the geometry accurately. The truncated ellipsoid, representing the solid domain, is discretized using $324,376$ $\mathbb{P}_1$ elements and $61,216$ nodes, which is the same as the uniform contraction simulation.
To imitate the function of the Purkinje network, which is not included in the mathematical model, stimuli are applied at three different points on the epicardial surface. These stimuli initiate the activation process and propagate through the myocardial tissue. The active stress is defined by a time-dependent cubical function

$$\hat{\mathbf{P}}_a = \alpha(t)\mathbf{Fgn} \otimes \mathbf{n} \tag{6.13}$$

$$\alpha(t) = (t \leq \psi_a) \cdot 0.0 + \left(\frac{T_a}{(0.2 - \psi_a)^3} \cdot (t - \psi_a)^3 \right) \cdot (t > \psi_a). \tag{6.14}$$

where ψ_a represents the activation time obtained by the resolution of the Eikonal model and the maximum value of the active stress is set to $T_a = 500$ [Pa], which is reached at $t = 0.20$ s.
For the parallel implementation of the proposed solution strategy, we utilize a single matrix preconditioner (SMP). The system resulting from the linearization of the Eikonal-diffusion model is solved using the SuperLU solver from the PETSC suite. In contrast, a Newton method is employed to linearize the mechanical equations, and the GMRES method is used to solve the associated system for both the uniform and Eikonal contraction cases. This parallel implementation strategy enables efficient computation and solution of the system equations, facilitating the simulation of cardiac mechanics.

The displacement results obtained from the simulation can be compared with the work by [Gerbi et al., 2018]. Furthermore, the activation map influences the deformation, as the geometry differs from that generated using a uniform active force (see Fig. 6.26). In addition to the fluid-structure interaction, the magnitude of the velocity field has also been analyzed, and it remains consistent with previous cases (Fig. 6.27). The velocity field, on the other hand, is strongly influenced by the choice of geometry, which does not include the aortic valve and the consequent increase in flow.

The simulation results reveal valuable insights into the contraction dynamics of the simplified right ventricle geometry. By incorporating the activation map derived from the Eikonal model, the active force plays a crucial role in driving the deformation of the geometry. Therefore, the simulation results demonstrate the effectiveness of the proposed approach in capturing the contraction behavior

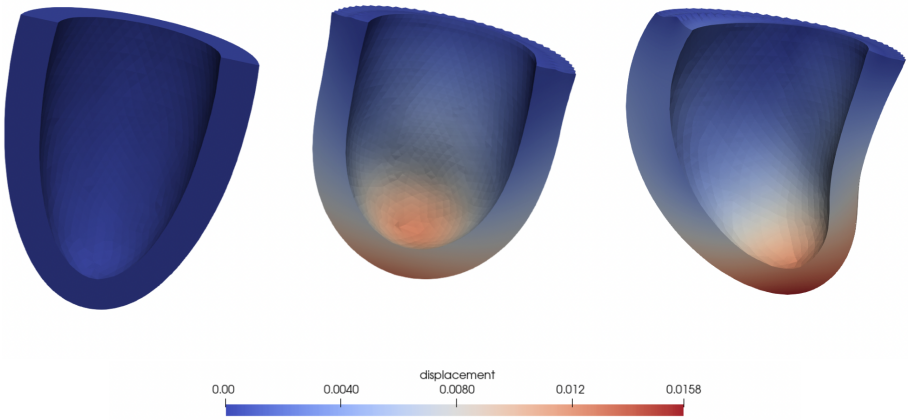

(a) first ($t = 0.00$s) and final ($t = 0.18$s) stage

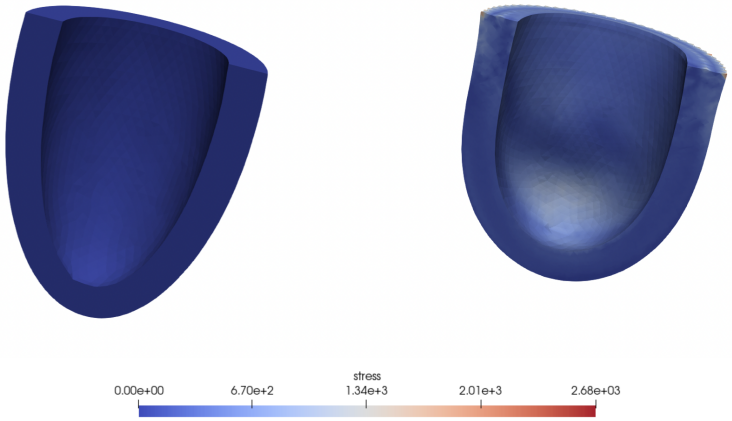

(b) first ($t = 0.00$s) and final ($t = 0.18$s) stage

Figure 6.26. Eikonal contraction. Displacement of two different sections of the ventricle and Von Mises stress.

of the simplified left ventricle geometry. The employment of the Eikonal model to construct the activation map allows for the integration of an active term in the fluid-structure model. While limitations exist due to the absence of a complete electromechanical coupling, the results provide a valuable starting point for further investigations and advancements in the understanding of cardiac functions.

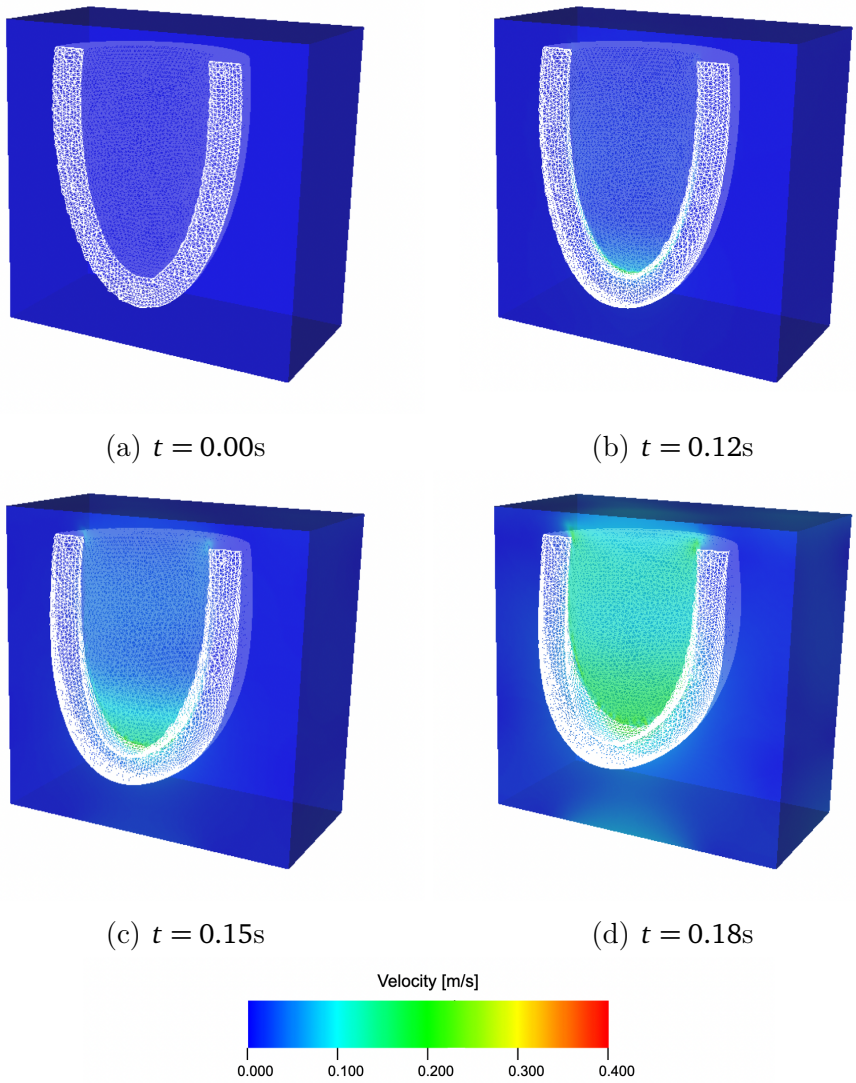

(a) $t = 0.00$s (b) $t = 0.12$s

(c) $t = 0.15$s (d) $t = 0.18$s

Figure 6.27. Eikonal contraction. Slice perspective of fluid velocity [m/s] and immersed displaced ventricle over time.

Monodomain with LR1 model

In this section, we extend our analysis by incorporating the activation time map evaluated using the Monodomain system coupled with the LuoRudy ionic model (Chapter 3). The Monodomain model provides more detailed information about cardiac electrophysiology compared to the Eikonal model.

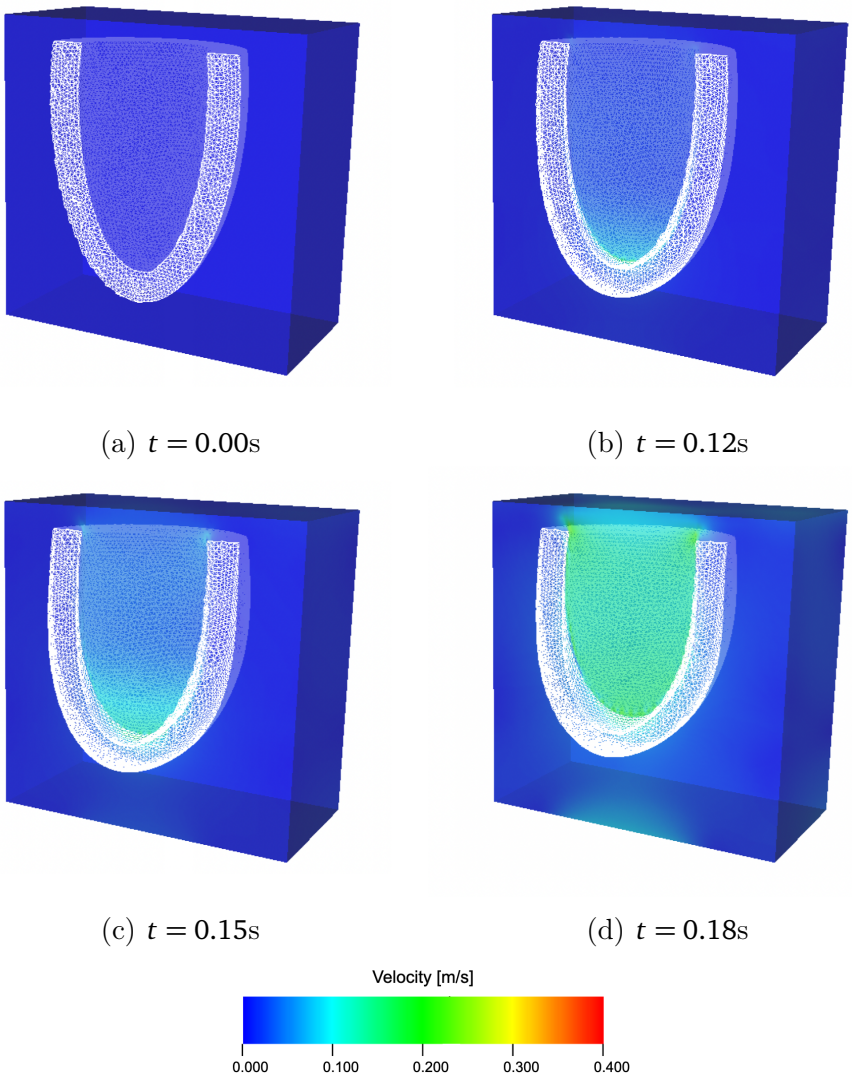

(a) $t = 0.00$s (b) $t = 0.12$s

(c) $t = 0.15$s (d) $t = 0.18$s

Figure 6.28. Monodomain contraction. Slice perspective of fluid velocity [m/s] and immersed displaced ventricle over time.

Then, to evaluate the activation time map, we solve the electrophysiological Monodomain problem separately and, due to the need for higher computational resolution, we discretize the ventricular domain with N = 460935 nodes. Subsequently, we interpolate the activation time onto the coarser mesh with N = 61216 nodes, which is consistent with the previous simulation. The fluid domain and its discretization remain the same as before.
Similar to the previous simulation, the active stress in this simulation is defined

by the time-dependent cubical function 6.13, which takes into account the time activation map obtained from the resolution of the Monodomain model. The threshold value for the action potential is fixed at -60.0 mV.
In this simulation, we set the maximum value of the active stress to $T_a = 5e^2$

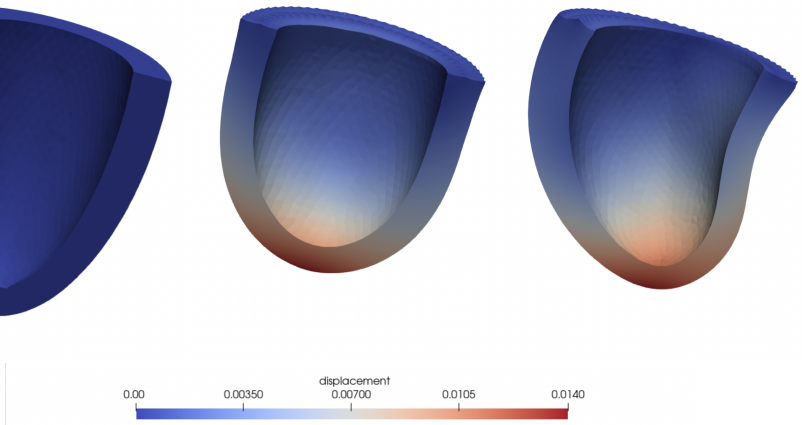

(a) first ($t = 0.00$s) and final ($t = 0.18$s) stage

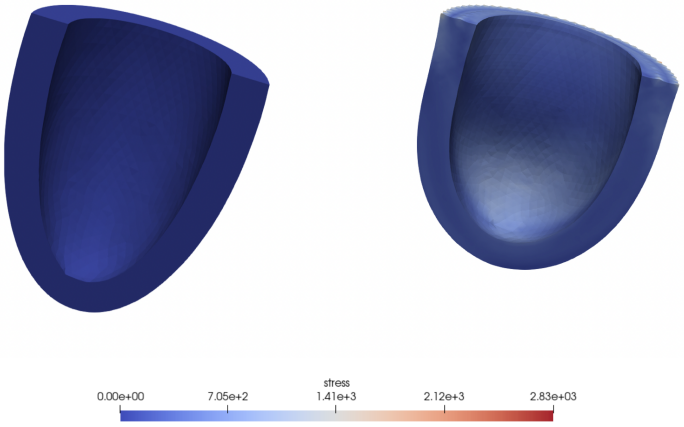

(b) first ($t = 0.00$s) and final ($t = 0.18$s) stage

Figure 6.29. Monodomain contraction. Displacement of two different sections of the ventricle and Von Mises stress.

[Pa]. This value determines the peak intensity of the active stress during the cardiac cycle, influencing the deformation and mechanical behavior of the ventricular walls.
To visualize the impact of the activation map on the dynamics, we present a slice

perspective of the magnitude of the velocity field and the displaced ellipsoid (Fig. 6.28). Additionally, we plot the displacement of the solid from different viewpoints, highlighting the influence of the activation map on the mechanical response (Fig. 6.29).

Furthermore, we analyze the velocity field, where we observe that, despite the

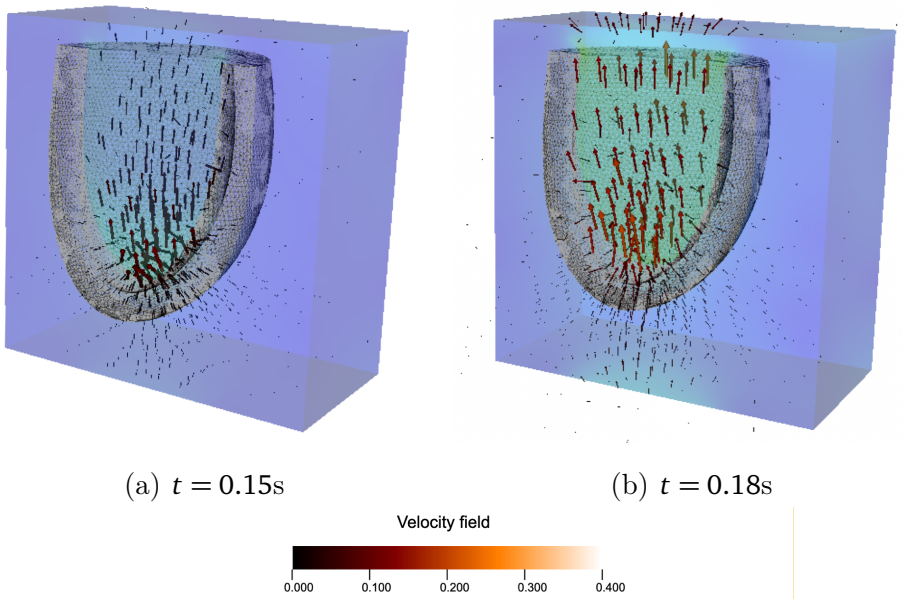

(a) $t = 0.15$s (b) $t = 0.18$s

Figure 6.30. Monodomain contraction. Velocity field at time $t = 0.15$[s] and $t = 0.18$[s].

reduction in the fluid domain compared to the two-dimensional simulations, the periodic boundary conditions do not significantly influence the dynamics (see Fig. 6.30). This observation underscores the robustness and validity of the simulation framework in capturing the fluid dynamics within the ventricular domain. It is essential to maintain an optimal ratio between the solid and fluid meshes to ensure regular solutions and stable performance. In particular, the interface between the solid and fluid domains is sensitive to the ratio of the two mesh sizes. An improper fraction can lead to instabilities and oscillations in the simulation results. This observation holds for both the current and previous simulations. To mitigate this issue, an adaptive mesh refinement technique could be introduced, especially in regions where the displacement and stress exhibit significant variations (see Fig. 6.30).

By incorporating the activation time map evaluated using the Monodomain model, we gain a more comprehensive understanding of cardiac electrophysiology and its impact on the mechanical response. The combination of the Monodomain

model and the fluid-structure interaction framework allows for a more realistic representation of cardiac dynamics, enabling us to study the complex interplay between electrical and mechanical processes in a simplified way.

Chapter 7

Conclusion

In this work, we developed a partioned coupled model for numerical cardiac simulations performing the fundamental physical processes concerning heart physiology by a one-way electro-fluid-structure interaction problem.
Initially, we explored electrophysiological models that describe the propagation of electrical signals through cardiac tissue. These models include the Monodomain model, which consists of a nonlinear reaction-diffusion equation coupled with a system of ordinary differential equations governing the evolution of gating variables for ionic channels, and the simplified Eikonal Model. To implement these electrophysiological models, we utilized the library *Pony*, which is based on the open-source C++ finite element framework MOOSE.
We considered a space discretization based on the finite element method and two different approaches for time discretization: the first was a semi-implicit finite difference method for the reaction-diffusion equation coupled with the Rush-Larsen scheme for the ODE's system. The second was a second-order time integrator scheme based on Strang splitting where a second-order θ-rule method for the resolution of the linear diffusive differential equation was combined with a second-order explicit predictor-corrector scheme for solving the nonlinear subproblem. We validated this time integrator with a Monodomain equation coupled with a modified FitzHugh Nagumo model for cardiac membrane cells, which successfully describes qualitative aspects of excitation, including some quantitative properties of cardiac tissue, such as the shape and the duration of the action potential.
Considering the mechanical properties of the heart and blood, which can be modeled as a Newtonian fluid, we then developed a generalized fluid-structure interaction formulation based on the immersed boundary method. In this formulation, we introduced a time-dependent active contribution expressed as active

stress to simulate the mechanical contraction of cardiac muscles. To validate our approach, we compared the results with the Turek-Hron benchmark, demonstrating the capability of our methodology to accurately capture the complex behavior of the cardiac system.
We first presented the results of a two-dimensional idealized ventricle simulation, where we simulated the inflow of blood and the contraction of the cardiac muscles. To initialize the ventricle, we utilized the deformed geometry generated by the inflation simulation. By incorporating the time-dependent active contribution, we were able to capture the dynamic contraction behavior of the ventricle, providing insights into the mechanical response of the cardiac muscles during the cardiac cycle.
Subsequently, we extended our investigation to three-dimensional simulations. Initially, we considered a uniform contraction of the idealized ventricle, examining the fluid-structure interaction and the resulting mechanical deformation. To further enhance the realism of our simulations, we incorporated two different activation maps derived from distinct models of cardiac electrophysiology. The first activation map was obtained through the resolution of the Eikonal Model, while the second was computed using the Monodomain model coupled with the LuoRudy ionic model. Hence, we were able to investigate the influence of cardiac electrophysiology on the mechanical behavior of the ventricle. By comparing the different activation maps, we were able to observe their distinct effects on the deformation patterns and mechanical response of the ventricle. This highlights the importance of incorporating detailed cardiac electrophysiological models to capture the full complexity of cardiac electromechanics.
The one-way electro-fluid-structure interaction algorithm was implemented in the finite element framework MOOSE, where a Newton method was used to linearize the solid problem, and GMRES was employed to solve the associated system and integrated with an Object Oriented Numerics Library $MOONoLith$ for the transfer of discrete fields and the flow solver IMPACT.
All the simulations were performed on the Euler Institute cluster (Lugano, Switzerland), composed of 42 compute nodes running CentOS 8.2.2004.x86_64 and the Piz Daint supercomputer at CSCS (Lugano, Switzerland), a hybrid Cray XC40/XC50 system with a total of 5320 compute nodes.

Based on the obtained results, future research should focus on advanced electromechanical couplings, including the effects of calcium concentration on active force generation and the feedback induced on the active force and electrophysiological equations by the mechanical model. Furthermore, it is important to consider a more realistic geometry of the ventricle and integrate it with the mitral

and aortic valves to accurately regulate and stabilize the inflow and outflow of blood, as well as simulate the velocity profile in specific regions of the domain. Additionally, several aspects remain open, such as mesh generation, boundary constraints, and fiber-reinforced material models.
A correct description of heart functions through these simulations has the potential to support medical research in investigating cardiac diseases and rare pathologies, particularly those with a limited number of patients.

Appendix

Anatomy and physiology of the heart

The heart is a complex organ primarily responsible for pumping blood through the body with an intricate system of muscle layers, chambers, valves, and nodes, its own circulation system, and an electrical conduction system that makes it contract and relax. Because of this task, the heart may be considered one of the most important organs of the body, and a methodical and numerical understanding could be the key for studying dysfunctions and abnormalities.
In this chapter, we present a basic description of the anatomy of the heart. In particular, we focus on the organic structure of the heart and its functions, then move on to the main characteristics of cardiac tissue and its contractile property and we conclude with a summary of the electrical conduction system of the heart.
Mammalian hearts can be viewed as a four-chambered pump, consisting of two separated pumps: one (the right heart) drives blood from the systemic veins into the pulmonary circulation, while the other one (the left heart) drives the oxygenated blood around the body. Each of these hearts is composed of two chambers: an atrium (the upper chamber) and a ventricle (the lower chamber). A layer of collagenous fibers called atrioventricular septum, is interposed between the atria and the ventricles to whom atrioventricular (AV) valves are fixed. On the right is the tricuspid valve, with three cusps, and on the left the mitral valve, also known as the bicuspid valve due to the presence of only two cusps. Semilunar valves separate each ventricle from its great artery: the pulmonary valve is located between the right ventricle and the pulmonary artery, while the aortic valve is between the left ventricle and the aorta Marieb and Hoehn [2007].

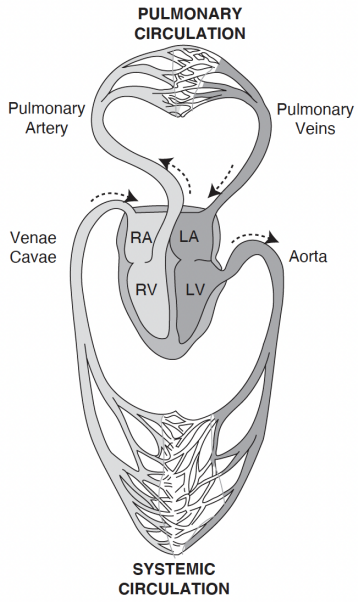

Figure 7.1. Schematic representation of the cardiovascular system (Physiology of the heart, Arnold M.Katz, MD, D.Med (Hon), FACP, FACC, Fig. 1-1, p. 4)

Electrical conduction

The heart is provided with a system for generating rhythmical electrical impulses to cause contraction of the heart muscle and conducting these impulses rapidly through the heart tissue.
Cardiac cells perform are both excitable and contractile. Their excitable conformation allows electrical signals, transmitted by the action potential (rapid changes in the membrane potential), to propagate through the cardiac tissue.
The electrical activity of the heart is initiated in a collection of cells known as the sinoatrial (SA) node located just below the superior vena cava on the right atrium with the capability of self-excitation, a process that can cause automatic rhythmical discharge and control the rate of the beat of the entire heart. The action potential, that is generated by the SA node, is then propagated through the atria by the atrial cells.
The conformation of the conductive system in the atria does not permit the cardiac impulse to travel from the atria into the ventricles too rapidly, such that atria have enough time for emptying their blood into the ventricles before a ventricular contraction begins.
The atria and ventricles are separated by a septum composed of non-excitable

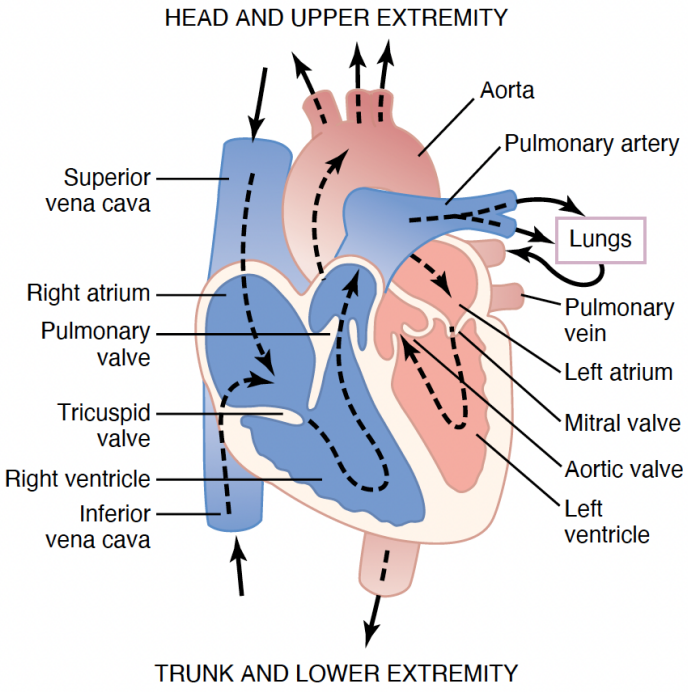

Figure 7.2. Structure of the heart and blood flow through the heart chambers (Textbook of medical physiology, Arthur C. Guyton, John E. Hall.—11th ed., Fig. 9-1, p. 104)

cells, so there is one pathway for the action potential to continue propagation and that is through another collection of cells, known as the atrioventricular node, located at the base of the atria. When the electrical signal leaves the AV node, it propagates through a specialized collection of fibers called the bundle of HIS, composed of Purkinje fibers, very large fibers which guarantee the instantaneous transmission of the cardiac impulse Katz [2010].
The Purkinje fiber network spreads via tree-like branching into the left and right bundle branches beneath the endocardium on the two sides of the ventricular septum. Each branch spreads throughout the interior of the ventricles progressively dividing into smaller branches.

Cardiac muscle

The heart wall is made up of three layers: the inner endocardium, the middle myocardium, and the outer epicardium. The middle layer of the heart, the my-

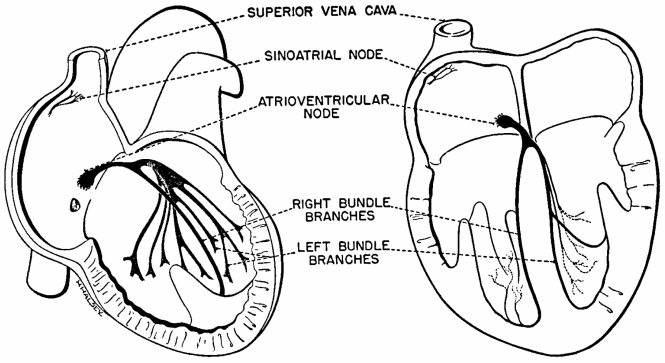

Figure 7.3. Schematic diagram of the cardiac conduction system (Cardiovascular dynamics, Rushmer, 1976)

ocardium, is the cardiac muscle, a layer of involuntary striated muscle tissue Guyton et al. [1986].
The main three types of cardiac muscle are atrial muscle, ventricular muscle, and excitatory and conductive muscle fibers. The contraction of atrial and ventricular muscles is similar to skeletal muscle, while the excitatory and conductive fibers contract feebly.
As in typical skeletal muscle, cardiac muscle is striated and has myofibrils that contain actin and myosin filaments which lie side by side and work together to produce muscle contraction.
Each cardiac fiber is made up of individual cells connected in series and in parallel with the other ones and cell membranes fuse with each other forming permeable junctions (gap junctions) that allow free diffusion of ions.
When an action potential diffuses over the cardiac muscle membrane, it spreads to the interior of the cardiac muscle fiber along the membranes of the transverse (T) tubules causing the release of calcium ions into the muscle sarcoplasm. These calcium ions diffuse into the myofibrils and induce the sliding of the actin and myosin filaments producing muscle contraction. Differently from the skeletal muscle, an additional large quantity of calcium ions diffuses into the sarcoplasm from the T tubules to increase muscle contraction strength.

Cardiac muscle contraction begins a few milliseconds after the first appearance of the action potential and continues until a few milliseconds after the action potential ends. For this reason, the duration of contraction of cardiac muscle can be considered as a function of the duration of action potential with values of about 0.2 milliseconds in atria and 0.3 milliseconds in ventricles.

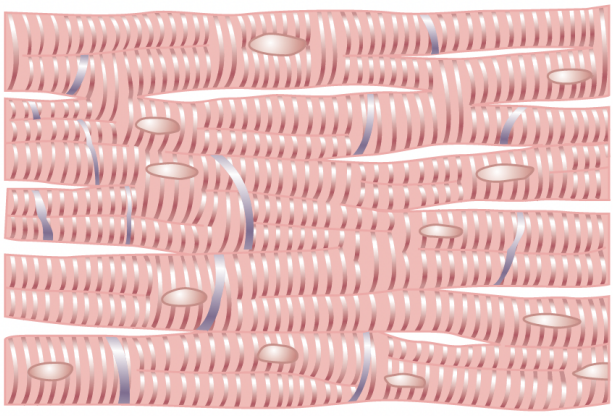

Figure 7.4. Structure of cardiac muscle fibers (Textbook of medical physiology, Arthur C. Guyton, John E. Hall.—11th ed., Fig. 9-2, p. 104)

Cardiac cycle

Changes in pressure and volume that occur during a heartbeat are repeated periodically in the same order. This repetition is referred to as the cardiac cycle.
The cardiac cycle can be divided into two major phases: systole and diastole. Systole is the phase characterized by the muscle transforming from its totally relaxed state to mechanical activation. Diastole is the period during which the muscle relaxes toward its resting state Fukuta and Little [2008].
The cardiac cycle duration is nearly 0.8[s] and is inversely proportional to the heart rate. Usually, under resting conditions, diastole lasts $\frac{2}{3}$ of the duration of cardiac cycle, while systole occupied $\frac{1}{3}$.
It is possible to give a schematic point of view of the cardiac cycle highlighting four main events: atrial systole, atrial diastole, ventricular systole, and ventricular diastole Luisada and MacCanon [1972].

- *Atrial systole and diastole*:

  at the beginning of the cardiac cycle, the atria and the ventricles are relaxed. Atrial diastole is characterized by the inflow of blood in the right atrium through the vena cava and in the left atrium through the pulmonary veins. In the first part of this phase the atrioventricular valves are closed then atria start to fill up with blood and the pressure inside increases until

it becomes greater than the pressure in the ventricles. When this pressure difference occurs, the atrioventricular valves open and blood flows inside the ventricles where the semilunar valves are closed to prevent backflow of blood from the aorta (on the left) and the pulmonary trunk (on the right). In this way, approximately $70-80$ percent of ventricular filling occurs.
Atrial contraction works for the remaining $20-30$ percent of filling and it is the main event of atrial systole. It starts when the SA node initiates an electrical signal that propagates throughout the atrial myocardium and results in the contraction of the atria, forcing any residual blood into the ventricles. It lasts for 0.1[s] while atrial diastole lasts for the resultant 0.7[s].
At the end of atrial systole, atrial diastole returns and ventricular systole begins.

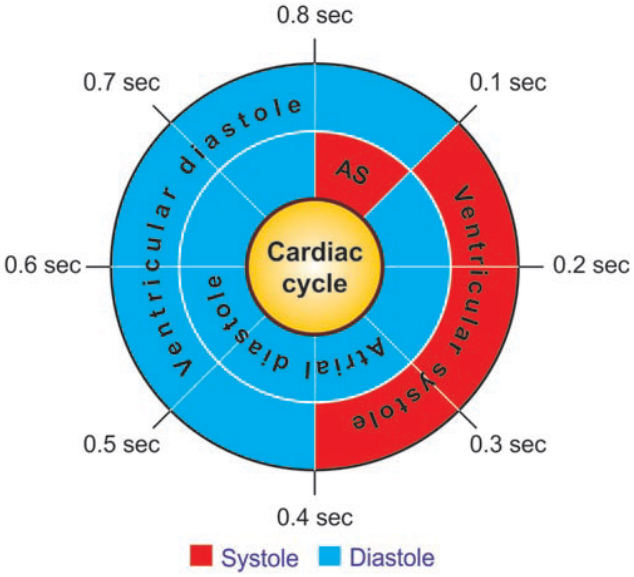

Figure 7.5. Summary of the sequence of events in cardiac cycle. The inner ring represents the atrial events while the outer ring the ventricular systole and diastole.

- *Ventricular systole*:

  it starts with the depolarization of ventricles, in particular when the electrical impulse arrives at the AV node, going then to the bundle of His and subsequently to the left and right bundle branches.

As the ventricular muscles begin to contract, the pressure inside the ventricles rises even though it is not high enough to induce the opening of semilunar valves. This increase in pressure is responsible for flowing back toward the atria of the blood, closing the tricuspid and mitral valves (atrioventricular valves).
Because both the valves are closed, no blood is ejected from the ventricles hence there is no change in volume. For this reason, it is said that ventricles are in the stage of isovolumetric contraction.
When the ventricular pressure exceeds the pressure in the pulmonary trunk and aorta, blood is pumped outside the ventricles, and the so called ejection phase starts. It usually lasts 0.25[s] and it can be divided into two parts: in the first part the outflow is very rapid, keeping 0.11[s], and we have the maximum ejection period, while in the second part, which lasts 0.14[s], the rate of outflow slows down.

- *Ventricular diastole*:

after the ejection of blood, the ventricular muscle relaxes, and as a consequence pressure within the ventricles begins to fall.
When the pressure inside the ventricles goes down below pressure in the pulmonary trunk and aorta, blood tries to roll back toward the ventricles but it is stopped by the closure of semilunar valves. At this point, both valves are closed and ventricles continue to relax as closed cavities and without outflow and inflow of blood. Hence it is named isovolumetric relaxation.
When the pressure inside the ventricles drops below the pressure in the atria, the atrioventricular valves open and a new cycle begins.

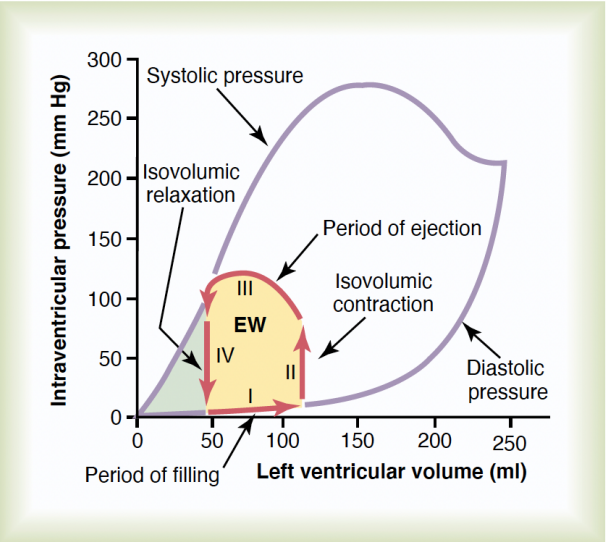

Figure 7.6. Volume-pressure diagram in red line and the relationship between intraventricular pressure and left ventricular volume (Textbook of medical physiology, Arthur C. Guyton, John E. Hall.—11th ed., Fig. 9-7, p. 110)

Bibliography

Azam Ahmad Bakir, Amr Al Abed, Michael C Stevens, Nigel H Lovell, and Socrates Dokos. A multiphysics biventricular cardiac model: Simulations with a left-ventricular assist device. *Frontiers in physiology*, 9:1259, 2018.

Rubin R Aliev and Alexander V Panfilov. A simple two-variable model of cardiac excitation. *Chaos, Solitons & Fractals*, 7(3):293–301, 1996.

D Ambrosi and S28990101312 Pezzuto. Active stress vs. active strain in mechanobiology: constitutive issues. *Journal of Elasticity*, 107(2):199–212, 2012.

Md S Arefin and Yosry S Morsi. Fluid structure interaction (fsi) simulation of the left ventricle (lv) during the early filling wave (e-wave), diastasis and atrial contraction wave (a-wave). *Australasian physical & engineering sciences in medicine*, 37(2):413–423, 2014.

MS Arefin et al. Fluid structure interaction (fsi) of the left ventricle (lv) in developing the next generation ventricular assist device (vad) system. *Swinburne University of Technology*, 2015.

Frank PT Baaijens. A fictitious domain/mortar element method for fluid–structure interaction. *International Journal for Numerical Methods in Fluids*, 35(7):743–761, 2001.

Nicolas Alejandro BARNAFI, Ngoc Mai Monica HUYNH, Luca Franco PAVARINO, and Simone SCACCHI. Parallel nonlinear solvers in computational cardiac electrophysiology. *IFAC-PapersOnLine*, 55(20):187–192, 2022.

Go W Beeler and H Reuter. Reconstruction of the action potential of ventricular myocardial fibres. *The Journal of physiology*, 268(1):177–210, 1977a.

Go W Beeler and H Reuter. Reconstruction of the action potential of ventricular myocardial fibres. *The Journal of physiology*, 268(1):177–210, 1977b.

Christine Bernardi, Yvon Maday, and Francesca Rapetti. Basics and some applications of the mortar element method. *GAMM-Mitteilungen*, 28(2):97–123, 2005.

Olivier Bernus, Ronald Wilders, Christian W Zemlin, Henri Verschelde, and Alexander V Panfilov. A computationally efficient electrophysiological model of human ventricular cells. *American Journal of Physiology-Heart and Circulatory Physiology*, 2002.

Daniele Boffi and Lucia Gastaldi. A finite element approach for the immersed boundary method. *Computers & structures*, 81(8-11):491–501, 2003.

Javier Bonet and Richard D Wood. *Nonlinear continuum mechanics for finite element analysis*. Cambridge university press, 1997.

Yves Bourgault, Yves Coudière, and Charles Pierre. Existence and uniqueness of the solution for the bidomain model used in cardiac electrophysiology. *Nonlinear Analysis-real World Applications*, 10:458–482, 2009a.

Yves Bourgault, Yves Coudiere, and Charles Pierre. Existence and uniqueness of the solution for the bidomain model used in cardiac electrophysiology. *Nonlinear analysis: Real world applications*, 10(1):458–482, 2009b.

Dietrich Braess. *Finite elements: Theory, fast solvers, and applications in solid mechanics*. Cambridge University Press, 2007.

Michele Bucelli, Matteo Salvador, Alfio Quarteroni, et al. Multipatch isogeometric analysis for electrophysiology: simulation in a human heart. *Computer Methods in Applied Mechanics and Engineering*, 376:113666, 2021.

Michele Bucelli, Alberto Zingaro, Pasquale Claudio Africa, Ivan Fumagalli, Luca Dede', and Alfio Quarteroni. A mathematical model that integrates cardiac electrophysiology, mechanics and fluid dynamics: application to the human left heart. *International Journal for Numerical Methods in Biomedical Engineering*, page e3678, 2022.

Michele Bucelli, Alberto Zingaro, Pasquale Claudio Africa, Ivan Fumagalli, Luca Dede', and Alfio Quarteroni. A mathematical model that integrates cardiac electrophysiology, mechanics, and fluid dynamics: Application to the human left heart. *International Journal for Numerical Methods in Biomedical Engineering*, 39(3):e3678, 2023.

Alfonso Bueno-Orovio, Elizabeth M Cherry, and Flavio H Fenton. Minimal model for human ventricular action potentials in tissue. *Journal of theoretical biology*, 253(3):544–560, 2008.

Martin Buist, Gregory Sands, Peter Hunter, and Andrew Pullan. A deformable finite element derived finite difference method for cardiac activation problems. *Annals of biomedical engineering*, 31(5):577–588, 2003.

Paola Causin, Jean-Frédéric Gerbeau, and Fabio Nobile. Added-mass effect in the design of partitioned algorithms for fluid–structure problems. *Computer methods in applied mechanics and engineering*, 194(42-44):4506–4527, 2005.

Bee Ting Chan, Chi Wei Ong, Einly Lim, NA Abu Osman, Amr Al Abed, Nigel H Lovell, and Socrates Dokos. Simulation of left ventricle flow dynamics with dilated cardiomyopathy during the filling phase. In *2012 Annual International Conference of the IEEE Engineering in Medicine and Biology Society*, pages 6289–6292. IEEE, 2012.

Ludovica Cicci, Stefania Fresca, Andrea Manzoni, and Alfio Quarteroni. Efficient approximation of cardiac mechanics through reduced order modeling with deep learning-based operator approximation, 2022a. URL `https://arxiv.org/abs/2202.03904`.

Ludovica Cicci, Stefania Fresca, Andrea Manzoni, and Alfio Quarteroni. Efficient approximation of cardiac mechanics through reduced order modeling with deep learning-based operator approximation. *arXiv preprint arXiv:2202.03904*, 2022b.

Piero Colli Franzone and Luca F Pavarino. A parallel solver for reaction–diffusion systems in computational electrocardiology. *Mathematical models and methods in applied sciences*, 14(06):883–911, 2004.

TIM Colonius, Sanjiva K Lele, and Parviz Moin. Boundary conditions for direct computation of aerodynamic sound generation. *AIAA journal*, 31(9):1574–1582, 1993.

Annie AM Cuyt and Louis B Rall. Computational implementation of the multivariate halley method for solving nonlinear systems of equations. *ACM Transactions on Mathematical Software (TOMS)*, 11(1):20–36, 1985.

Luca Dede, Alfio Quarteroni, and Francesco Regazzoni. Mathematical and numerical models for the cardiac electromechanical function. *Rendiconti Lincei-Matematica e Applicazioni*, 32(2):233–272, 2021.

Giulio Del Corso, Roberto Verzicco, and Francesco Viola. A fast computational model for the electrophysiology of the whole human heart. *Journal of computational physics*, 457:111084, 2022.

Antonio DeSimone, Benoît Perthame, Alfio Quarteroni, Lev Truskinovsky, L Dede', A Gerbi, and A Quarteroni. Segregated algorithms for the numerical simulation of cardiac electromechanics in the left human ventricle. *The Mathematics of Mechanobiology: Cetraro, Italy 2018*, pages 81–116, 2020.

J Donea, A Huerta, JP Ponthot, and A Rodríguez-Ferran. Arbitrary lagrangian-eulerian methods. in: Encyclopedia of computational mechanics second edition. 2017.

F Dorri, PF Niederer, and PP Lunkenheimer. A finite element model of the human left ventricular systole. *Computer methods in biomechanics and biomedical engineering*, 9(5):319–341, 2006.

Konstantin Fackeldey, Dorian Krause, Rolf Krause, and Christoph Lenzen. Coupling molecular dynamics and continua with weak constraints. *Multiscale Modeling & Simulation*, 9(4):1459–1494, 2011.

Longling Fan, Jing Yao, Chun Yang, Di Xu, and Dalin Tang. Modeling active contraction and relaxation of left ventricle using different zero-load diastole and systole geometries for better material parameter estimation and stress/strain calculations. *Molecular & cellular biomechanics: MCB*, 13(1):33, 2016.

Liuyang Feng, Hao Gao, Boyce Griffith, Steven Niederer, and Xiaoyu Luo. Analysis of a coupled fluid-structure interaction model of the left atrium and mitral valve. *International Journal for Numerical Methods in Biomedical Engineering*, 35(11):e3254, 2019.

Richard FitzHugh. Impulses and physiological states in theoretical models of nerve membrane. *Biophysical journal*, 1(6):445–466, 1961.

Piero Colli Franzone and Luciano Guerri. Spreading of excitation in 3-d models of the anisotropic cardiac tissue. i. validation of the eikonal model. *Mathematical biosciences*, 113(2):145–209, 1993.

Piero Colli Franzone and Giuseppe Savaré. Degenerate evolution systems modeling the cardiac electric field at micro-and macroscopic level. In *Evolution equations, semigroups and functional analysis*, pages 49–78. Springer, 2002.

Piero Colli Franzone, Luca Franco Pavarino, and Simone Scacchi. *Mathematical cardiac electrophysiology*, volume 13. Springer, 2014.

Hidekatsu Fukuta and William C Little. The cardiac cycle and the physiologic basis of left ventricular contraction, ejection, relaxation, and filling. *Heart failure clinics*, 4(1):1–11, 2008.

Hao Gao, David Carrick, Colin Berry, Boyce E Griffith, and Xiaoyu Luo. Dynamic finite-strain modelling of the human left ventricle in health and disease using an immersed boundary-finite element method. *IMA journal of applied mathematics*, 79(5):978–1010, 2014.

Hao Gao, Liuyang Feng, Nan Qi, Colin Berry, Boyce E. Griffith, and Xiaoyu Luo. A coupled mitral valve—left ventricle model with fluid–structure interaction. *Medical Engineering & Physics*, 47:128–136, 2017. ISSN 1350-4533. doi: https://doi.org/10.1016/j.medengphy.2017.06.042. URL `https://www.sciencedirect.com/science/article/pii/S1350453317301819`.

Antonello Gerbi, Luca Dedè, and Alfio Quarteroni. A monolithic algorithm for the simulation of cardiac electromechanics in the human left ventricle. *Mathematics in Engineering*, 1(ARTICLE):1–37, 2018.

Giacomo Gigante and Christian Vergara. On the stability of a loosely-coupled scheme based on a robin interface condition for fluid-structure interaction. *Computers & Mathematics with Applications*, 96:109–119, 2021.

R Glowinski and Yu Kuznetsov. Distributed lagrange multipliers based on fictitious domain method for second order elliptic problems. *Computer Methods in Applied Mechanics and Engineering*, 196(8):1498–1506, 2007.

Boyce E Griffith and Xiaoyu Luo. Hybrid finite difference/finite element immersed boundary method. *International journal for numerical methods in biomedical engineering*, 33(12):e2888, 2017a.

Boyce E Griffith and Xiaoyu Luo. Hybrid finite difference/finite element immersed boundary method. *International journal for numerical methods in biomedical engineering*, 33(12):e2888, 2017b.

Boyce E Griffith, Xiaoyu Luo, David M McQueen, and Charles S Peskin. Simulating the fluid dynamics of natural and prosthetic heart valves using the immersed boundary method. *International Journal of Applied Mechanics*, 1(01): 137–177, 2009.

Debao Guan, Hao Gao, Li Cai, and Xiaoyu Luo. A new active contraction model for the myocardium using a modified hill model. *Computers in Biology and Medicine*, 145:105417, 2022. ISSN 0010-4825. doi: https://doi.org/10.1016/j.compbiomed.2022.105417. URL https://www.sciencedirect.com/science/article/pii/S0010482522002098.

Julius M Guccione, Kevin D Costa, and Andrew D McCulloch. Finite element stress analysis of left ventricular mechanics in the beating dog heart. *Journal of biomechanics*, 28(10):1167–1177, 1995.

Arthur C Guyton, John Edward Hall, et al. *Textbook of medical physiology*, volume 548. Saunders Philadelphia, 1986.

Abdallah I Hassaballah, Mohsen A Hassan, Azizi N Mardi, and Mohd Hamdi. An inverse finite element method for determining the tissue compressibility of human left ventricular wall during the cardiac cycle. *PloS one*, 8(12):e82703, 2013.

Rolf Henniger, Dominik Obrist, and Leonhard Kleiser. High-order accurate solution of the incompressible navier–stokes equations on massively parallel computers. *Journal of Computational Physics*, 229(10):3543–3572, 2010.

C Hesch, AJ Gil, A Arranz Carreno, J Bonet, and P Betsch. A mortar approach for fluid–structure interaction problems: Immersed strategies for deformable and rigid bodies. *Computer Methods in Applied Mechanics and Engineering*, 278: 853–882, 2014.

Alan L Hodgkin and Andrew F Huxley. A quantitative description of membrane current and its application to conduction and excitation in nerve. *The Journal of physiology*, 117(4):500, 1952.

Gerhard A Holzapfel. Nonlinear solid mechanics: a continuum approach for engineering science. *Meccanica*, 37(4):489–490, 2002.

Akira Hosoi, Takumi Washio, Jun-ichi Okada, Yoshimasa Kadooka, Kengo Nakajima, and Toshiaki Hisada. A multi-scale heart simulation on massively parallel computers. In *SC'10: Proceedings of the 2010 ACM/IEEE International Conference for High Performance Computing, Networking, Storage and Analysis*, pages 1–11. IEEE, 2010.

Greg Ikonnikov, Dominique Yelle, E Wong, and S Chaudhry. Physiology of cardiac conduction and contractility. *MacMaster Physiological Review*, 2014.

Smadar Karni. Accelerated convergence to steady state by gradual far-field damping. *AIAA journal*, 30(5):1220–1227, 1992.

Arnold M Katz. *Physiology of the Heart*. Lippincott Williams & Wilkins, 2010.

James Keener and James Sneyd. *Mathematical physiology: II: Systems physiology*. Springer, 2009.

James P Keener. An eikonal-curvature equation for action potential propagation in myocardium. *Journal of mathematical biology*, 29(7):629–651, 1991.

W.Yong Kim, Thue Bisgaard, Sten L. Nielsen, Jens K. Poulsen, Erik M. Pedersen, J.Michael Hasenkam, and Ajit P. Yoganathan. Two-dimensional mitral flow velocity profiles in pig models using epicardial doppler echocardiography. *Journal of the American College of Cardiology*, 24(2):532–545, 1994. doi: 10.1016/0735-1097(94)90314-X.

Richard Klabunde. *Cardiovascular physiology concepts*. Lippincott Williams & Wilkins, 2011.

Markus Kloker, Uwe Konzelmann, and H Fasel. Outflow boundary conditions for spatial navier-stokes simulations oftransition boundary layers. *AIAA journal*, 31(4):620–628, 1993.

VI Kondaurov and LV Nikitin. Finite strains of viscoelastic muscle tissue. *Journal of Applied Mathematics and Mechanics*, 51(3):346–353, 1987.

Rolf Krause and Patrick Zulian. A parallel approach to the variational transfer of discrete fields between arbitrarily distributed unstructured finite element meshes. *SIAM Journal on Scientific Computing*, 38(3):C307–C333, 2016.

Joel Kronborg, Frida Svelander, Samuel Eriksson-Lidbrink, Ludvig Lindström, Carme Homs-Pons, Didier Lucor, and Johan Hoffman. Computational analysis of flow structures in turbulent ventricular blood flow associated with mitral valve intervention. *Frontiers in Physiology*, page 752, 2022a.

Joel Kronborg, Frida Svelander, Samuel Eriksson-Lidbrink, Ludvig Lindström, Carme Homs-Pons, Didier Lucor, and Johan Hoffman. Computational analysis of flow structures in turbulent ventricular blood flow associated with mitral valve intervention. *Frontiers in Physiology*, 13:806534, 2022b.

Markku Kupari, P Hekali, and V Poutanen. Cross sectional profiles of systolic flow velocities in left ventricular outflow tract of normal subjects. *British heart journal*, 74:34–9, 07 1995. doi: 10.1136/hrt.74.1.34.

Sander Land, Viatcheslav Gurev, Sander Arens, Christoph M Augustin, Lukas Baron, Robert Blake, Chris Bradley, Sebastian Castro, Andrew Crozier, Marco Favino, et al. Verification of cardiac mechanics software: benchmark problems and solutions for testing active and passive material behaviour. *Proceedings of the Royal Society A: Mathematical, Physical and Engineering Sciences*, 471 (2184):20150641, 2015a.

Sander Land, Viatcheslav Gurev, Sander Arens, Christoph M Augustin, Lukas Baron, Robert Blake, Chris Bradley, Sebastian Castro, Andrew Crozier, Marco Favino, et al. Verification of cardiac mechanics software: benchmark problems and solutions for testing active and passive material behaviour. *Proceedings of the Royal Society A: Mathematical, Physical and Engineering Sciences*, 471 (2184):20150641, 2015b.

Luca Lanzilao and Johan Meyers. An improved fringe-region technique for the representation of gravity waves in large-eddy simulation with application to wind farms, 2022.

Zhaowu Lin, Andrew Hess, Zhaosheng Yu, Shengqiang Cai, and Tong Gao. A fluid–structure interaction study of soft robotic swimmer using a fictitious domain/active-strain method. *Journal of Computational Physics*, 376:1138–1155, 2019.

Svein Linge, Joakim Sundnes, Monica Hanslien, Glenn Terje Lines, and Aslak Tveito. Numerical solution of the bidomain equations. *Philosophical Transactions of the Royal Society A: Mathematical, Physical and Engineering Sciences*, 367(1895):1931–1950, 2009.

William C Little. Assessment of normal and abnormal cardiac function. *Heart disease*, 2001.

Aldo A Luisada and Donald M MacCanon. The phases of the cardiac cycle. *American heart journal*, 83(5):705–711, 1972.

Elaine Nicpon Marieb and Katja Hoehn. *Human anatomy & physiology*. Pearson education, 2007.

Rajat Mittal and Gianluca Iaccarino. Immersed boundary methods. *Annu. Rev. Fluid Mech.*, 37:239–261, 2005.

MARILENA MUNTEANU and LUCA FRANCO PAVARINO. Implicit parallel solvers in computational electrocardiology. In *Applied Analysis and Differential Equations*, pages 255–266. World Scientific, 2007.

Marilena Munteanu and Luca F Pavarino. Decoupled schwarz algorithms for implicit discretizations of nonlinear monodomain and bidomain systems. *Mathematical Models and Methods in Applied Sciences*, 19(07):1065–1097, 2009.

Maria Murillo and Xiao-Chuan Cai. A fully implicit parallel algorithm for simulating the non-linear electrical activity of the heart. *Numerical linear algebra with applications*, 11(2-3):261–277, 2004.

Maria Giuseppina Chiara Nestola, Barna Becsek, Hadi Zolfaghari, Patrick Zulian, Dario De Marinis, Rolf Krause, and Dominik Obrist. An immersed boundary method for fluid-structure interaction based on variational transfer. *Journal of computational physics*, 398:108884, 2019.

Amir Nikou, Shauna Dorsey, Jeremy McGarvey, Joseph Gorman III, Jason Burdick, James Pilla, Robert Gorman, and Jonathan Wenk. Computational modeling of healthy myocardium in diastole. *Annals of biomedical engineering*, 44, 07 2015. doi: 10.1007/s10439-015-1403-7.

Amir Nikou, Shauna M Dorsey, Jeremy R McGarvey, Joseph H Gorman, Jason A Burdick, James J Pilla, Robert C Gorman, and Jonathan F Wenk. Computational modeling of healthy myocardium in diastole. *Annals of biomedical engineering*, 44(4):980–992, 2016.

David Nordsletten, M McCormick, PJ Kilner, Peter Hunter, D Kay, and NP Smith. Fluid–solid coupling for the investigation of diastolic and systolic human left ventricular function. *International Journal for Numerical Methods in Biomedical Engineering*, 27(7):1017–1039, 2011.

Jan Nordström, Niklas Nordin, and Dan Henningson. The fringe region technique and the fourier method used in the direct numerical simulation of spatially evolving viscous flows. *SIAM Journal on Scientific Computing*, 20.4:1365–1393, 1999.

Luca F Pavarino and Piero Colli Franzone. A parallel solver for reaction-diffusion systems in computational electrocardiology.

Charles S Peskin. Numerical analysis of blood flow in the heart. *Journal of computational physics*, 25(3):220–252, 1977.

Simone Pezzuto, Peter Kal'avskỳ, Mark Potse, Frits W Prinzen, Angelo Auricchio, and Rolf Krause. Evaluation of a rapid anisotropic model for ecg simulation. *Frontiers in physiology*, 8:265, 2017.

Roberto Piersanti, Pasquale C Africa, Marco Fedele, Christian Vergara, Luca Dedè, Antonio F Corno, and Alfio Quarteroni. Modeling cardiac muscle fibers in ventricular and atrial electrophysiology simulations. *Computer Methods in Applied Mechanics and Engineering*, 373:113468, 2021.

Mark Potse, Bruno Dubé, Jacques Richer, Alain Vinet, and Ramesh M Gulrajani. A comparison of monodomain and bidomain reaction-diffusion models for action potential propagation in the human heart. *IEEE Transactions on Biomedical Engineering*, 53(12):2425–2435, 2006a.

Mark Potse, Bruno Dubé, Jacques Richer, Alain Vinet, and Ramesh M Gulrajani. A comparison of monodomain and bidomain reaction-diffusion models for action potential propagation in the human heart. *IEEE Transactions on Biomedical Engineering*, 53(12):2425–2435, 2006b.

Steffan Puwal and Bradley J Roth. Forward euler stability of the bidomain model of cardiac tissue. *IEEE transactions on biomedical engineering*, 54(5):951–953, 2007.

Zhilin Qu and Alan Garfinkel. An advanced algorithm for solving partial differential equation in cardiac conduction. *IEEE Transactions on Biomedical Engineering*, 46(9):1166–1168, 1999a.

Zhilin Qu and Alan Garfinkel. An advanced algorithm for solving partial differential equation in cardiac conduction. *IEEE Transactions on Biomedical Engineering*, 46(9):1166–1168, 1999b.

Alfio Quarteroni and Silvia Quarteroni. *Numerical models for differential problems*, volume 2. Springer, 2009.

Francesco Regazzoni, Luca Dedè, and Alfio Quarteroni. Active force generation in cardiac muscle cells: mathematical modeling and numerical simulation of the actin-myosin interaction. *Vietnam Journal of Mathematics*, 49(1):87–118, 2021.

Scott I Heath Richardson, Hao Gao, Jennifer Cox, Rob Janiczek, Boyce E Griffith, Colin Berry, and Xiaoyu Luo. A poroelastic immersed finite element framework for modelling cardiac perfusion and fluid–structure interaction. *International journal for numerical methods in biomedical engineering*, 37(5):e3446, 2021.

Simone Rossi, Ricardo Ruiz-Baier, Luca F Pavarino, and Alfio Quarteroni. Orthotropic active strain models for the numerical simulation of cardiac biomechanics. *International journal for numerical methods in biomedical engineering*, 28(6-7):761–788, 2012.

Stanley Rush and Hugh Larsen. A practical algorithm for solving dynamic membrane equations. *IEEE Transactions on Biomedical Engineering*, (4):389–392, 1978.

Youcef Saad and Martin H Schultz. Gmres: A generalized minimal residual algorithm for solving nonsymmetric linear systems. *SIAM Journal on scientific and statistical computing*, 7(3):856–869, 1986.

Roya Sattarzadeh, Anahita Tavoosi, Mostafa Jabbari, Amir Farhang Zand Parsa, Babak Geraiely, Mohammad Saadat, Farnoosh Larti, Ali Pasha Meysamie, and Mehrdad Salehi. Acceleration rate of mitral inflow e wave: a novel transmitral doppler index for assessing diastolic function. *Cardiovascular Ultrasound*, 14: 1–6, 2015.

P. Schlatter, N.A. Adams, and L. Kleiser. A windowing method for periodic inflow/outflow boundary treatment of non-periodic flows. *Journal of Computational Physics*, 206(2):505–535, 2005.

NP Smith, DP Nickerson, EJ Crampin, and PJ Hunter. Multiscale computational modelling of the heart. *Acta Numerica*, 13:371–431, 2004.

PR Spalart. Direct numerical study of leading-edge contamination. *Fluid dynamics of three-dimensional turbulent shear flows and transition*, pages 5–1, 1989.

Simone Stella, Francesco Regazzoni, Christian Vergara, Luca Dede, and Alfio Quarteroni. A fast cardiac electromechanics model coupling the eikonal and the nonlinear mechanics equations. *Mathematical Models and Methods in Applied Sciences*, 32, 05 2022. doi: 10.1142/S021820252250035X.

Joakim Sundnes, Glenn Terje Lines, Xing Cai, Bjørn Frederik Nielsen, Kent-Andre Mardal, and Aslak Tveito. *Computing the electrical activity in the heart*, volume 1. Springer Science & Business Media, 2007.

Larry A Taber and Renato Perucchio. Modeling heart development. *Journal of elasticity and the physical science of solids*, 61(1):165–197, 2000.

Kirsten HWJ Ten Tusscher and Alexander V Panfilov. Alternans and spiral breakup in a human ventricular tissue model. *American Journal of Physiology-Heart and Circulatory Physiology*, 291(3):H1088–H1100, 2006.

Mark L Trew, Bruce H Smaill, David P Bullivant, Peter J Hunter, and Andrew J Pullan. A generalized finite difference method for modeling cardiac electrical activation on arbitrary, irregular computational meshes. *Mathematical biosciences*, 198(2):169–189, 2005.

Stefan Turek and Jaroslav Hron. Proposal for numerical benchmarking of fluid-structure interaction between an elastic object and laminar incompressible flow. In *Fluid-structure interaction*, pages 371–385. Springer, 2006.

Taras P Usyk, Ian J LeGrice, and Andrew D McCulloch. Computational model of three-dimensional cardiac electromechanics. *Computing and visualization in science*, 4:249–257, 2002.

Marco Veneroni. Reaction–diffusion systems for the macroscopic bidomain model of the cardiac electric field. *Nonlinear Analysis: Real World Applications*, 10(2): 849–868, 2009.

Francesco Viola, Valentina Meschini, and Roberto Verzicco. Fluid–structure-electrophysiology interaction (fsei) in the left-heart: a multi-way coupled computational model. *European Journal of Mechanics-B/Fluids*, 79:212–232, 2020.

HM Wang, H Gao, XY Luo, C Berry, BE Griffith, RW Ogden, and TJ Wang. Structure-based finite strain modelling of the human left ventricle in diastole. *International journal for numerical methods in biomedical engineering*, 29(1): 83–103, 2013.

Lewis Wexler, Derek H Bergel, Ivor T Gabe, GEOFFREY S MAKIN, and CHRISTOPHER J MILLS. Velocity of blood flow in normal human venae cavae. *Circulation Research*, 23(3):349–359, 1968.

Alan A Wray. Very low storage time-advancement schemes. Technical report, Internal Report, Moffett Field, CA, NASA-Ames Research Center, 1986.

Patrick Zulian, Teseo Schneider, Kai Hormann, and Rolf Krause. Parametric finite elements with bijective mappings. *BIT Numerical Mathematics*, 57(4):1185–1203, 2017.